

Mathematical modelling of supraglacial meltwater production and drainage

by

Tim Hill

A thesis
presented to the University of Waterloo
in fulfillment of the
thesis requirement for the degree of
Master of Mathematics
in
Applied Mathematics

Waterloo, Ontario, Canada, 2021

© Tim Hill 2021

This thesis consists of material all of which I authored or co-authored: see Statement of Contributions included in the thesis. This is a true copy of the thesis, including any required final revisions, as accepted by my examiners.

I understand that my thesis may be made electronically available to the public.

Statement of Contributions

Tim Hill was the sole author for Chapters 1, 3, and 5, which were written under the supervision of Dr. Christine Dow. Chapters 2, 4, and Appendices A, B of this thesis consist of manuscripts and their corresponding supplementary material written for publication as detailed below.

Chapter 2

Chapter 2 contains a copy of the peer-reviewed manuscript “Application of an improved surface energy balance model to two large valley glaciers in the St. Elias Mountains, Yukon” as published in the *Journal of Glaciology*. Appendix A contains a copy of the corresponding supplementary material. This research was conducted at the University of Waterloo under the supervision of Dr. Christine Dow, and with contributions from Dr. Eleanor Bash (University of Calgary) and Dr. Luke Copland (University of Ottawa).

Eleanor Bash contributed to the design of the comparison experiment and consulted on the methodology and software development. Luke Copland curated the in-situ data and validated the satellite-derived albedo maps. Christine Dow supervised the project, contributed to the design of the comparison between Kaskawulsh Glacier and Nàhùdäy (Lowell Glacier), and curated in-situ data. All authors contributed to revising and editing the manuscript.

Tim Hill contributed to the study’s design, and was the primary author responsible for the methodology, software, running the numerical experiments, visualization, analysis, and writing the manuscript draft.

Citation for Chapter 2:

Hill, T., Dow, C., Bash, E., & Copland, L. (2021). Application of an improved surface energy balance model to two large valley glaciers in the St. Elias Mountains, Yukon. *Journal of Glaciology*, 67(262) 297–312. doi:[10.1017/jog.2020.106](https://doi.org/10.1017/jog.2020.106)

Chapter 4

Chapter 4 contains a modified version of the manuscript “Modeling the dynamics of supraglacial rivers and distributed meltwater flow with the Subaerial Drainage System (SaDS) model” submitted to the *Journal of Geophysical Research: Earth Surface* on 11 June 2021. Appendix B contains the companion supplementary information. This chapter was modified to reference and avoid repeating the numerical methods described in Chapter 3, and to expand the discussion of the model’s mathematical formulation.

This work was done in collaboration with Christine Dow, who contributed to the design of the experiments, consulted on the methodology, and revised and edited the manuscript. Tim Hill was the primary author responsible for the majority of the work including developing the mathematical framework of the model, developing and testing the numerical model, designing and carrying out the model runs, and writing the manuscript.

Citation for Chapter 4:

Hill, T. & Dow, C.. Modeling the dynamics of supraglacial rivers and distributed melt-water flow with the Subaerial Drainage System (SaDS) model. (submitted). *Journal of Geophysical Research: Earth Surface*, 2021JF006309

Abstract

Mountain glaciers and the polar ice sheets exert a critical control on water resource availability, drive sea level change, and impact global ocean circulation. These and other impacts are controlled by surface meltwater that flows through the glacier hydrologic system to the base of the ice and drives seasonal and long-term changes in ice flow velocity. This thesis presents numerical models for the production and transport of meltwater runoff across the surface of melting glaciers and ice sheet.

First, a surface energy balance model is developed that improves on existing models by utilizing high resolution satellite data to capture spatial variations in surface melt. The model is applied to Kaskawulsh Glacier and Nâłudây (Lowell) Glacier in the St. Elias Mountains, Yukon, Canada using six years of in-situ meteorological data. By validating model outputs against in-situ measurements, it is shown that modelled seasonal melt agrees with observations within 9% across a range of elevations.

In order to determine how surface meltwater is transported through moulins, we develop the Subaerial Drainage System (SaDS) model. SaDS is a physics-based, finite-volume numerical model that calculates supraglacial runoff in both a distributed sheet and through supraglacial channels. The benefit of this approach is that a connected network of supraglacial channels and lakes naturally emerges without using prior information about the channel network, for example from satellite-derived maps. In synthetic settings and when applied to the Greenland Ice Sheet, model outputs show realistic and varied moulin flux rates, and modelled supraglacial lake and channel locations match those mapped from satellite images. These results demonstrate that SaDS is a promising tool to provide moulin inputs for subglacial and ice dynamic studies.

These models represent significant steps forward in their respective domains. Together, these tools will be valuable components of future modelling work, including for studies that aim to constrain how climatic variables control sea level contributions from glaciers and ice sheets.

Acknowledgements

First, I would like to acknowledge that this work was undertaken at the Waterloo campus of the University of Waterloo, which is situated on the Haldimand Tract, land that was promised to the Haudenosaunee of the Six Nations of the Grand River, and are within the territory of the Neutral, Anishinaabe, and Haudenosaunee peoples.

Parts of this work were undertaken in the traditional territory of Kluane First Nation, and I am very grateful for their permission to undertake this research. Permission to use the traditional Dákwangè (Southern Tutchone) toponym for the Lowell Glacier, Nàhùdäy, also spelled Nafudi, was provided by Champagne and Aishihik First Nations and the Kluane First Nation.

I am honoured to have received funding from the Natural Sciences and Engineering Research Council (NSERC), the Ontario Graduate Scholarship program, and the Northern Scientific Training Program.

Thank you to everyone from Outers Club who kept me sane during my time at the University of Waterloo, including Christian, Micaela, Evan, Claire, Ali, and Ari. You all made my time with the club so rewarding.

This work would not have been possible without all of my collaborators. I would like to thank Eleanor Bash and Luke Copland for their contributions to the surface energy balance model. Thank you to the rest of the IceLab and everyone from the University of Ottawa who I talked about research with, and to Laura Thomson and Christopher Omelon for giving me the opportunity to do fieldwork on Axel Heiberg Island. Finally, I appreciate the rest of the UWaterloo Glaciology Group for their feedback and support.

I am grateful to everyone who has taught me along the way, including the fluids group for teaching me about applying numerical modelling and applied math to earth systems, and Wesley Van Wychen for teaching me about glaciers. Also to Ray Nassar, who provided me with my first opportunity to do research and taught me how to do good science.

None of this would have been possible without Christine Dow's supervision. Thank you for trusting me, helping me when I needed it, endlessly editing (improving) my work, and always encouraging me to set ambitious goals.

Thank you to my parents, Annamarie and Stephen, for instilling in me curiosity about the world around me and for supporting me throughout my (lengthy) university career.

Most of all, I'm thankful for my fiancée Christine Yanta's continuing support. Thank you for encouraging me in everything I do – you help me more than you could ever know. And thank you for letting me miss Valentine's Day to learn crevasse rescue.

Table of Contents

List of Tables	xi
List of Figures	xii
1 Introduction	1
1.1 Overview	1
1.2 Background	2
1.2.1 Mass balance and melt	2
1.2.2 Supraglacial hydrology	4
1.2.3 Englacial hydrology	6
1.2.4 Subglacial hydrology	6
1.2.5 Ice flow mechanisms	7
1.3 Numerical models	8
1.3.1 Surface melt models	8
1.3.2 Supraglacial hydrology models	8
1.3.3 Englacial hydrology models	12
1.3.4 Subglacial hydrology models	13
1.4 Format of the thesis	13

2	Application of an improved surface energy balance model to two large valley glaciers in the St. Elias Mountains, Yukon	15
2.1	Introduction	15
2.2	Study area	17
2.3	Data and methods	20
2.3.1	Data	20
2.3.2	Glacier surface shading	25
2.3.3	Debris insulation	26
2.3.4	Subsurface model	28
2.3.5	Surface energy balance model	30
2.3.6	Model implementation	32
2.3.7	Model evaluation and uncertainty estimation	33
2.4	Results	35
2.4.1	Albedo maps	35
2.4.2	Kaskawulsh Glacier, 2010–14	36
2.4.3	Kaskawulsh and Naluday, 2018	37
2.4.4	Shading by adjacent topography	41
2.4.5	Subsurface model	41
2.5	Discussion	44
2.5.1	Model performance	44
2.5.2	Model limitations and uncertainties	46
2.5.3	Implications for understanding surge mechanisms	47
2.6	Conclusions	49
3	Finite volume methods on unstructured triangular mesh elements and edges	51
3.1	Introduction	51
3.2	Unstructured mesh topology	52

3.3	General form	53
3.4	Gradient reconstruction on unstructured elements	54
3.4.1	Green-Gauss methods	54
3.4.2	Least squares methods	56
3.4.3	Method comparison	58
3.5	Finite volume methods on edge network	60
3.6	Gradient calculation on edge network	60
3.6.1	Arithmetic averaging	61
3.6.2	Least squares method	61
3.6.3	Interpolation with Matlab	61
3.6.4	Method comparison	62
3.7	Mass conservation on edge network	63
3.8	Conclusions	63
4	Modeling the dynamics of supraglacial rivers and distributed meltwater flow with the Subaerial Drainage System (SaDS) model	65
4.1	Introduction	65
4.2	Model description	67
4.2.1	Sheet model	68
4.2.2	Channel model	69
4.2.3	Mass exchange	72
4.2.4	Summary of model equations	73
4.2.5	Numerical methods	74
4.2.6	Boundary conditions	75
4.3	Synthetic ice sheet margin experiments	75
4.3.1	Ice sheet margin domain	75
4.3.2	Surface melt parameterization	76
4.3.3	Baseline scenario	77

4.3.4	Sensitivity tests	79
4.4	Internally drained catchments on the Greenland Ice Sheet	85
4.4.1	Input data	85
4.4.2	Results	87
4.5	Discussion	89
4.5.1	Synthetic ice sheet margin	89
4.5.2	Sensitivity tests	90
4.5.3	Application to the Greenland Ice Sheet	92
4.5.4	Assumptions and simplifications in the model formulation	93
4.6	Conclusions	94
5	Conclusions and future work	96
5.1	General conclusions	96
5.2	Limitations	97
5.3	Future work	99
	References	100
	APPENDICES	116
A	Supplementary material for Application of an improved surface energy balance model to two large valley glaciers in the St. Elias Mountains, Yukon	117
B	Supplementary information to “Modeling the dynamics of supraglacial rivers and distributed meltwater flow with the Subaerial Drainage System (SaDS) model”	123
B.1	Introduction	123

List of Tables

1.1	Summary of supraglacial hydrology models	10
2.1	Summary statistics of in-situ albedo measurements	36
2.2	Modelled melt volumes and uncertainties, 2010–2014 and 2018.	39
4.1	Model variables symbols, descriptions, and units	68
4.2	Parameters (top group) and physical constants (bottom group)	70
4.3	Deviations from the default parameters (Table 4.2) for the sensitivity tests	80
A.1	Location and temporal coverage of HOBO loggers	118
A.2	Summary of AWS data	118
A.3	Default parameters used in the SEB model	119
A.4	Total and relative model error and ablation rate error	122
B.1	Mesh statistics for resolution tests	130

List of Figures

1.1	Connections between glaciers and their environment	3
1.2	ISMIP6 sea level rise projections	4
1.3	Overview of glacier hydrology	5
2.1	Study site in the St. Elias Mountains, Yukon.	18
2.2	Digital elevation model and surface albedo	21
2.3	Comparison between modelled and measured ablation, 2010–2014	37
2.4	Comparison between modelled and measured ablation, 2018	38
2.5	Modelled surface melt on Kaskawulsh and Nàhùdäy, 2018	40
2.6	Effect of shading the glacier surface for the period 27 July to 15 September 2018	42
2.7	Difference in modelled melt due to subsurface heat conduction model	43
2.8	Modelled melt rates and elevation profiles on Kaskawulsh and Nàhùdäy Glaciers for the period 27 July–15 September 2018	48
3.1	Mesh topology and nomenclature	52
3.2	Element-based gradient reconstruction stencils	56
3.3	Comparison of element-based gradient reconstruction methods	59
3.4	Comparison of edge network gradient reconstruction methods	62
3.5	Schematic diagram of mass conservation method	64
4.1	Cross-sectional geometry of supraglacial channels.	71

4.2	Synthetic ice sheet margin domain	76
4.3	Baseline model outputs	78
4.4	Moulin inputs and diurnal amplitude for the baseline	79
4.5	Sensitivity test hydrographs	81
4.6	Moulin inputs and diurnal amplitude for case S4	83
4.7	Resolution sensitivity test	84
4.8	Overview of the Greenland model domain	86
4.9	Greenland modelled drainage system	89
A.1	Mean albedo as a function of elevation on Kaskawulsh Glacier, 2014 to 2019	120
A.2	Impact of the subsurface heat conduction model	121
B.1	Numerical method stencils	124
B.2	SHMIP surface melt parameterization	125
B.3	Moulin input sensitivity to the timestep	126
B.4	Model outputs for case M1	126
B.5	Median RACMO surface melt rate	127
B.6	Greenland modeled drainage system with expanded channel initialization .	128
B.7	Channel configuration leading to two distinct peaks in diurnal amplitude .	129
B.8	Surface melt due to potential energy dissipation	129

With four parameters I can fit an elephant, and with five I can make him wiggle his trunk.

John Von Neumann

We all know that art is not truth. Art is a lie that makes us realize truth, at least the truth that is given us to understand. The artist must know the manner whereby to convince others of the truthfulness of his lies.

Pablo Picasso

Chapter 1

Introduction

1.1 Overview

Glaciers and ice sheets cover 10% of the Earth's surface and represent the largest reservoir of freshwater on Earth [143; 75]. With such a significant volume of water, glaciers and ice sheets effect both human and natural systems, including impacting water resource availability, natural hazards, sea level change, and downstream ecosystems [143]. Glacier hazards, including floods, debris flows, and the potential for damaging sea level rise receive considerable attention beyond the glaciological community [e.g. 56; 127].

Along with the human and natural implications of glacier change, glaciers represent a uniquely interesting and important application for mathematical modelling. At the simplest level, glaciers are nonlinear and complex systems. We need numerical models to understand these systems since alpine glaciers and polar ice sheets are difficult to access, especially when some important physical processes occur under hundreds (or thousands) of meters of ice. Given that glaciers and ice sheets represent a significant source for sea level rise throughout this century and beyond, predictive models are critical to inform decision making in response to climate change.

Numerical models of glacier systems encounter multiple challenges. There is a disparity of scales between the scale of the relevant physical mechanisms, which can be tens of meters or smaller, and the scale of the domain, which can be hundreds or thousands of kilometres. Ice flow models routinely couple thermal and mechanical processes (ice deformation and sliding), yet a truly comprehensive model would also have to include hydrological processes at the surface and the bed, fracture mechanics, and frontal ablation processes, including

calving. These challenges, and the importance of understanding these systems, makes numerical modelling of glacier systems particularly interesting and relevant.

1.2 Background

Glaciers are best thought of as complex systems including not just the ice itself, but also liquid meltwater, snow, firn, bedrock, and proglacial outputs. This section traces the path of liquid water generated at the melting glacier surface through the glacier system in order to explain how surface melt and the flow paths taken by water on the glacier surface influences glacier flow velocities and dynamics. This relationship between surface melt and glacier velocity is important since climate-driven acceleration and retreat of glaciers contributes to sea level rise [76] and terminus position changes of lake-terminating glaciers can impact the frequency of glacial lake outburst floods [61].

1.2.1 Mass balance and melt

A glacier's mass balance is determined by the difference between accumulation (mass gain) and ablation (mass loss). Typically, the dominant source of accumulation is snowfall. Avalanching, wind-blown snow, hoar frost, and rain may also contribute to accumulation [16]. The dominant sources of ablation are surface melt, calving, and basal melt, with smaller contributions by sublimation, evaporation, and snow redistribution by winds [16]. When a glacier is in balance with the climate its long-term average mass balance should be zero.

Mass balance and surface melt rates have wide implications. In some regions, glaciers provide an important water resource as summer melt provides a steady source of water in what might be an otherwise dry season. For example, 8–20% of the Bow River's flow through Calgary in the summer is attributed to glacier melt in the Rocky Mountains [13], providing an important source for downstream demands [144]. In the context of a warming climate, flow in rivers stemming from glacier runoff will increase at first as glacier melt rates increase. However, as glacierized area decreases, a turning point will be reached where the decrease in area becomes more important than increasing melt rates. This is called “peak water”. After this point, flow will decrease until the glaciers disappear [70]. Understanding the timing of peak water is critical for communities who rely on glacier runoff.

Changes in mass balance can also shift natural hazard risks. Terminus retreat driven by mass loss combined with increased melt rates can lead to the development or enlargement

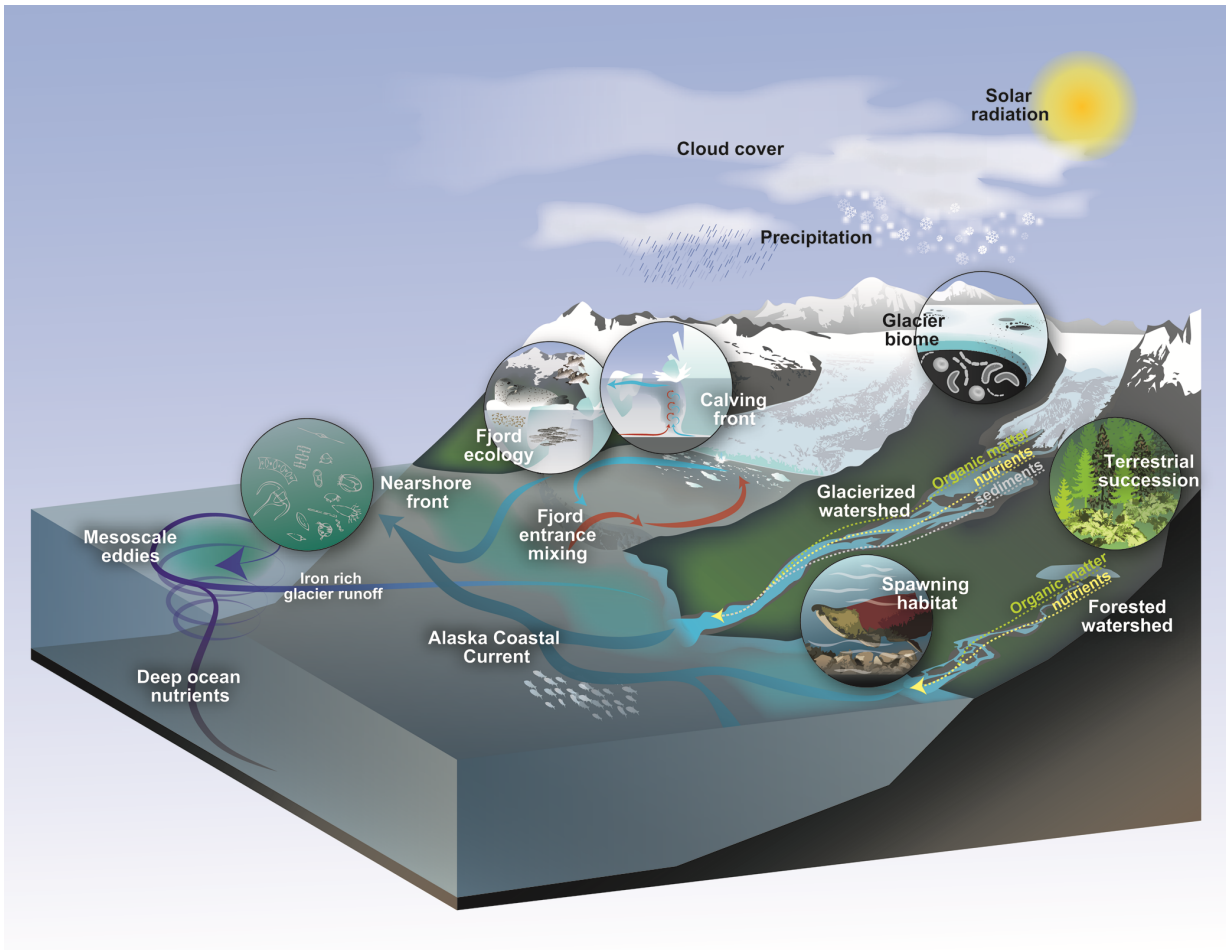


Figure 1.1: Connections between ecosystems and glaciers in the Gulf of Alaska region. From [112].

of moraine-dammed lakes, increasing the risk of potentially catastrophic outburst floods [61].

Natural systems are also impacted by mass balance and melt rates. (Figure 1.1). For example, freshwater runoff from glaciers and icefields accounts for 47% of the freshwater discharge into the Gulf of Alaska, with 10% of this coming from recent rapid glacier mass loss [102]. Glaciers are also a source of nutrients to downstream ecosystems, impacting salmon productivity [112].

Perhaps the most commonly reported consequence of increasing mass loss from glaciers

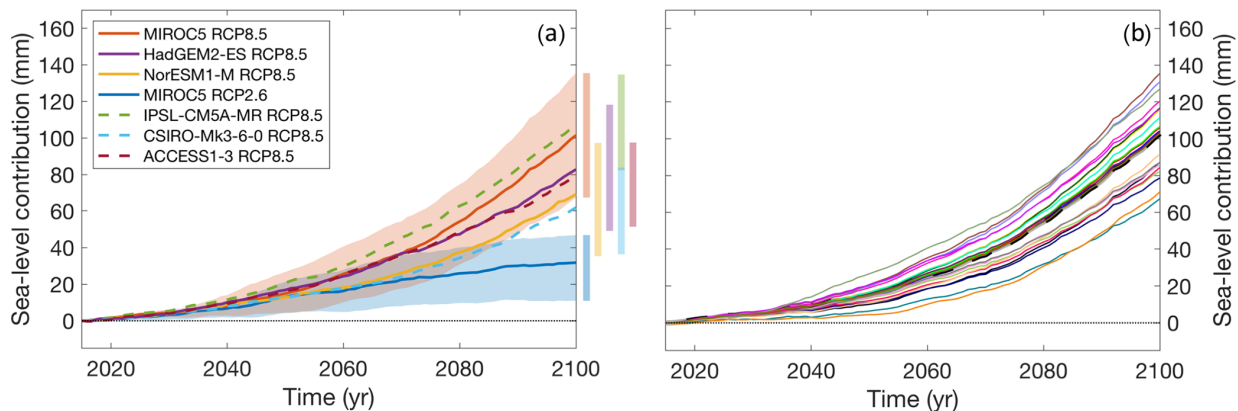


Figure 1.2: Greenland sea level rise projections to 2100 from the Ice Sheet Model Intercomparison Project 6 (ISMPI6) project [59]. (a) Ice sheet model ensemble mean projections with model spread for different climate forcing scenarios (shaded areas and bars on right). (b) Specific results for each model and climate scenario. From Goelzer et al. [59]

and ice sheets is increased rates of sea level rise. Globally, glacier ice has the potential to raise sea levels by more than 60 m [143; 75]. While only a small fraction of this mass is expected to melt in the near future, approximately two-thirds of current sea level rise is due to melting glaciers and ice sheets [88]. The rate of cryospheric sea level rise, especially from the polar ice sheets, is expected to increase throughout this century, although there is considerable uncertainty in the magnitude (Figure 1.2) [59].

1.2.2 Supraglacial hydrology

Once meltwater is produced at the glacier surface it flows through the supraglacial drainage system (Figure 1.3). The mode of supraglacial drainage depends on where the meltwater is generated. In the accumulation zone, water percolates through snow and firn layers overlying the ice. Meltwater can refreeze within the firn layers to form ice lenses and slabs, which also impacts water routing and storage, or meltwater can percolate to the base of the snowpack and flow downhill as saturated flow [27; 97].

In the ablation zone, flow begins as sheet-like flow across the bare ice surface. Flow eventually accumulates into a network of streams, rivers, and lakes [27; 134]. Flow in supraglacial rivers is complicated by the fact that viscous heat dissipation and friction against the river bed melts the underlying ice. This additional melt means that supraglacial rivers increase in flow rapidly along their length and causes rivers to evolve throughout

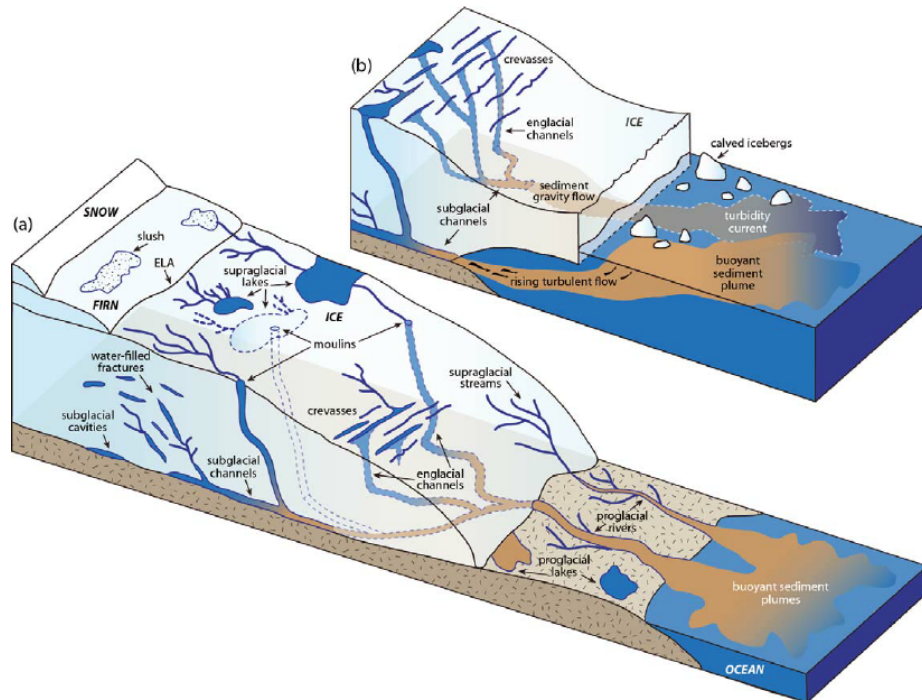


Figure 1.3: Overview of glacier hydrology. Supraglacial hydrology above the equilibrium line altitude (ELA) is dominated by snow, firn, and slush. Below the ELA, hydrology is dominated by supraglacial rivers, lakes, moulin (vertical shafts that let water drain from the surface to the bed), and crevasses. The subglacial drainage system transports subglacial water across the grounding line for marine-terminating glaciers, and across the terminus for land-terminating glaciers. From Chu [27].

the melt season [27; 115]. As the ice surface melts it also lowers, acting to reducing the cross-sectional area of supraglacial streams and rivers. Large rivers can balance surface lowering by cutting downward through melt along the bed, while smaller streams with insufficient incision rates melt out as surface melt progresses, leaving only larger rivers to transport meltwater [153].

The supraglacial river network has important implications for moulin inputs. A well-developed river network with a high capacity leads to moulin inputs with high diurnal amplitude, while a poorly-developed network leads to moulin input rates that are nearly constant throughout the day, even as melt reduces or pauses overnight [153; 64]. These differences likely have important implications for subglacial hydrology, although the effect has not yet been fully tested.

1.2.3 Englacial hydrology

Between the surface and the bed, meltwater travels through the englacial drainage system, which includes englacial conduits, moulins, and possibly water storage within permeable ice (Figure 1.3) [52; 16]. Englacial conduits can form when supraglacial streams cut downwards into the ice sufficiently that the roof closes over the channel [52; 73], or by exploiting existing weaknesses, fractures, or permeable structures (e.g. crevasses) in the ice [16]. This system is important as it controls the timing and location of the delivery of supraglacial runoff to the bed. However, it is very difficult to access and observe the englacial system given that it is dangerous to ascend into and difficult to constrain with geophysical instrumentation, so numerical models of englacial conduit and moulins are only now beginning to be developed [e.g. 3].

1.2.4 Subglacial hydrology

Geothermal heat and frictional heat at the bed, combined with high pressure lowering the melting point of ice, melts basal ice [52]. Combined with water inputs from moulins, significant volumes of water can be found at the bed. For instance, Lindbäck et al. [91] reported total subglacial runoff of 5.4 km^3 from 29 May to 10 September 2010 for the Isunnguata Sermia catchment (total area below 1750 m asl of 3200 km^2) and 6.5 km^3 for the Kangerlussuaq catchment (total area below 1750 m asl of 2800 km^2) beneath the Greenland Ice Sheet. This water once again flows down potential gradients towards the terminus. It is hypothesized that subglacial flow occurs through two primary modes. Slow flow is suggested to occur through a long, torturous series of linked cavities, or by Darcian flow through sediment, whereas fast flow occurs through large conduits melted into the base of the ice or carved into the underlying sediments [16]. Depending on water inputs, slow flow through linked cavities can have water pressures nearly as high as, or greater than, the pressure of the ice overhead (called the overburden pressure). When sufficient flow accumulates to initialize channelization, subglacial conduits remove most of the subglacial water and reduce pressure in the drainage system by drawing in water from the higher pressure distributed system.

The timing, volume, and location of supraglacial meltwater inputs to the subglacial system are important drivers of subglacial water pressure. At the beginning of the season, surface melt begins towards the terminus and advances upglacier towards higher elevations as the melt season progresses. The development of the subglacial drainage systems follows the same seasonal progression since the delivery of surface meltwater to the bed drives subglacial development. Moulin inputs allow the subglacial system to become channelized,

with channels extending down potential gradients from moulin locations. This reduces subglacial water pressure, draws higher pressure water away from the distributed system, and decreases the sliding velocity. At the same time, the glacier becomes more responsive to temporal changes in meltwater forcing [123]. Once the subglacial system is channelized, the diurnal amplitude of melt forcing induces a diurnal cycle in subglacial water pressure and therefore glacier velocity [e.g. 137]. Large spikes in meltwater inputs can fully pressurize the subglacial channels, releasing water back into the distributed system and temporarily increasing glacier velocity. Since the configuration of the supraglacial drainage system is the primary control on the location, timing, and volume of moulin inputs, understanding supraglacial hydrology is important for determining the drivers of ice dynamics.

1.2.5 Ice flow mechanisms

Glaciers are not simply static ice masses. They flow downhill as individual ice crystals slide relative to each other in response to driving stresses (primarily gravity) [16]. The relationship between stress balance and flow is nonlinear, usually described by Glen’s Flow Law [106]. Despite the nonlinearity, ice creep is relatively well understood and straightforward to calculate.

Glacier flow is made more complicated by the presence of liquid water at the bed. Sufficient subglacial pressure from accumulating water reduces friction at the ice-rock interface, allowing the glacier to slide downhill. The total velocity is the sum of basal sliding and ice deformation [16]. However, this process is subject to significant uncertainty as it is difficult to access the subglacial environment to verify models. Subglacial pressure depends on the configuration of the subglacial drainage system, bedrock topography and glacier geometry, and the flow rate of water from the surface to the bed through moulins.

By taking this system-level view, we see that liquid water generated at the surface travels through the supraglacial, englacial, and subglacial drainage systems and therefore controls subglacial water pressure, basal sliding, and eventually ice flow velocity. This is important since changes in velocity impact sea level rise by driving ice discharge from marine-terminating glaciers. Given these implications, significant effort has been invested in developing numerical models of meltwater production and transport through the glacial system.

1.3 Numerical models

1.3.1 Surface melt models

Surface melt models can be organized on a spectrum of increasing complexity. The most basic melt models are degree-day (DD) and temperature index (TI) models that calculate melt as a linear function of air temperature [e.g. 21; 117]. DD and TI models must be calibrated with local air temperature and melt data to calculate the degree-day factor. The simple formulation of these models makes them suitable for modelling surface melt over large domains and for long periods of time. However, since they only depend on air temperature, they lack spatial variations caused by changes in glacier aspect, slope, albedo, and supraglacial debris.

These simple melt models can be improved by including direct solar radiation, called Enhanced Temperature Index (ETI) models [e.g. 66; 14]. ETI models also must be calibrated with local data, but are more accurate than DD and TI models [67]. Since these models include the effect of solar radiation, they include the effects of slope and aspect. Bash and Moorman [14] used a high resolution UAV-derived map of surface albedo and so their melt model correctly accounts for spatial variations in melt due to spatial patterns in albedo. However, ETI models still require high quality in-situ data to calibrate the melt factors. This data is only available in select locations, and there is no physical basis for how melt factors transfer between regions.

Finally, melt can be modelled by physically-based surface energy balance (SEB) models. SEB models calculate melt from the net balance of shortwave radiation, longwave radiation, turbulent heat fluxes, and subsurface heat flux [e.g. 5; 44; 47; 9; 14]. These models are theoretically better positioned to accurately calculate surface melt since they attempt to model the physical processes responsible for melt. However, in practice they have similar performance to ETI models [14] because they have several parameters that are difficult to measure and calibrate, require a large amount of input data, and the turbulent flux parameterizations are not always accurate [47]. Nevertheless, owing to their physical basis, SEB models are usually recommended over ETI models when sufficient meteorological data is available to drive the model.

1.3.2 Supraglacial hydrology models

Despite the wide reaching implications of surface meltwater routing, there is not a consensus on the best approaches (Table 1.1) and there remains room for improvement. As with melt

models, it is convenient to organize supraglacial hydrology models by complexity. Table 1.1 compares several representative models that are described below.

Instantaneous runoff models

The most basic approach to route surface meltwater to the bed is to directly include climate model surface runoff as a distributed input to the subglacial system [e.g. 36]. This approach entirely neglects any time delay introduced by flow through the supraglacial drainage system and the spatially localized nature of flow through moulins. These limitations should be carefully considered when using this method since they may lead to significant errors in subglacial hydrology.

Instantaneous moulin inputs

Next, models may route meltwater instantaneously through moulins to the subglacial environment. Typically, catchments are delineated from a digital elevation model (DEM), and all runoff generated within each catchment is instantaneously routed through the outlet moulin or river [e.g. 95; 11]. In this way these models capture the spatial localization of flow through moulins, however this approach neglects the time it takes for water to travel across the surface and does not account for storage in supraglacial lakes. This method is simple to implement, computationally efficient, and requires minimal data, so it is suitable for applications that span very large spatial domains and where short timescale (<1 day) dynamics are not of interest.

Flow routing

Flow routing models further improve upon instantaneous moulin input models. Flow routing models route water generated in each cell of a DEM down the path of steepest descent and calculate the travel time using a velocity parameterization (in practice, often temporally and spatially constant velocity). The flow through catchment outlets is calculated by summing the surface melt generated within each cell using the calculated time delay [e.g. 4; 33; 34].

This approach is better than instantaneously routing runoff since it accounts for the time it takes for water to flow from where it is generated to the catchment outlet. This leads to reduced diurnal amplitude in moulin inputs, which likely impacts the diurnal amplitude of subglacial water pressure. It can also account for more physical processes,

Table 1.1: Summary of representative supraglacial hydrology and runoff models. Flow routing type models pre-calculate flow paths using a digital elevation model and use a constant velocity to calculate travel times. Dynamic models explicitly calculate time derivatives of water depth using a mathematical model.

Reference	Model type	Sheet flow	Channel flow
Arnold et al. [4]	Flow routing	✓	×
Marshall and Clarke [94]	Dynamic	✓	×
Raymond and Nolan [118]	Dynamic	×	✓
Flowers and Clarke [49]	Dynamic	✓	×
McGrath et al. [95]	Instantaneous runoff	×	×
Bartholomew et al. [11]	Instantaneous runoff	×	×
Clason et al. [33]	Flow routing	✓	×
Leeson et al. [87]	Dynamic	✓	×
Kingslake et al. [77]	Dynamic	×	✓
Clason et al. [34]	Flow routing	✓	×
Smith et al. [130]	Synthetic Unit Hydrograph (SUH)	✓	✓
Koziol and Arnold [83]	Flow routing	✓	✓
Yang et al. [153]	Rescaled Width Function (flow routing)	✓	✓
Gleason et al. [58]	Dynamic (Hillslope River Routing)	✓	✓

including different flow velocities across bare ice or snow and firn, and the filling and draining of lakes [8]. However, flow routing models have a few primary limitations. In order to calculate continuous flow paths, any sinks in the DEM must be filled. This means that lake basins must be pre-calculated and the filling and draining of each lake needs to be explicitly modelled, making it difficult to account for changes in flow paths throughout the year.

Most flow routing models have focused on slow, distributed flow only. Yang et al. [153] extended this approach by combining flow through a connected network of supraglacial rivers with distributed flow in the areas between rivers. Runoff is routed in a distributed sheet until it intersects a supraglacial channel, after which it is routed through the channel network. Moulin hydrographs are calculated by using different flow velocities in each system to calculate travel times and time-delayed flow accumulation. The partitioning between sheet and channel flow is calculated from an arbitrary parameterization of the minimum area threshold for channelization. The area threshold is parameterized to monotonically increase throughout the melt season so that drainage system density decreases. This is suggested to represent the melt out of small supraglacial channels, however direct measurements to support this parameterization are not available. This model is a significant step forward, although it leaves room for models that use a physics-based approach to determine changes in the drainage system.

Dynamic models

The most complete models are based on mathematical conservation laws. These dynamic models have similar behaviour to flow routing models, but are more flexible given their formulation as partial differential equations. Dynamic models can directly model supraglacial lake development since water flows down potential gradients, the flow velocity can depend on the depth of flow and surface slope, and flow paths can change throughout the melt season. They have been presented for distributed sheet flow [e.g. 49; 87] and for flow in supraglacial rivers, including for rivers draining supraglacial lakes [e.g. 118; 77]. These studies have yet to include both modes of supraglacial runoff.

Coupling distributed and channelized flow

Few models to date have explicitly combined distributed and channelized supraglacial meltwater flow. In addition to Yang et al. [153] (discussed above), Smith et al. [130] derived a synthetic unit hydrograph (SUH) from direct measurements of supraglacial streamflow

that can predict streamflow through catchment outlets accounting for both modes of flow. However, the hydrograph is built up from generic, non-physically based basis functions. This makes it difficult to transfer the model to new catchments.

Koziol and Arnold [83] extended the Surface Routing and Lake Filling model [8] by including draining of supraglacial lakes through moulins and channels that incise downwards. This model more completely captures supraglacial lake dynamics, including unstable drainage, but only includes supraglacial rivers that form during lake drainage events.

Gleason et al. [58] applied the Hillslope River Routing (HRR) model, a terrestrial hydrology model, to a catchment on the Greenland Ice Sheet. This is a dynamic model that calculates distributed and river flow, but with some limitations due to its formulation as a terrestrial hydrology model. HRR requires a high resolution, topologically connected supraglacial river network map derived from high resolution satellite imagery. HRR also does not include surface lowering due to surface melt or melt along supraglacial rivers, so it does not account for seasonal changes in the drainage system.

These studies are all limited by the prior knowledge they require of the supraglacial drainage system. Smith et al. [130] derived their SUH directly from in-situ discharge measurements which are not widely available. Koziol and Arnold [83] requires maps of supraglacial lakes, whereas Yang et al. [153] and Gleason et al. [58] also need high resolution, topologically connected maps of the supraglacial river network. These maps are time consuming to create and have only been developed for limited areas.

Finally, only Yang et al. [153] represented seasonal changes in the drainage system, and this was done with a prescribed inter-channel width function. This approach is not physically based, so it leaves space for more complete supraglacial hydrology models.

Summary of models

Existing supraglacial hydrology models show a range of complexity. The most complete models represent both distributed and channelized flow [130; 83; 58], while Yang et al. [153] included seasonal changes in the drainage system. However, existing models heavily rely on prior maps of the supraglacial drainage system and have yet to physically model seasonal expansion and contraction of the channel network.

1.3.3 Englacial hydrology models

Given the inaccessibility of the englacial system and that the subglacial system modulates any impacts on ice velocity, englacial hydrology models are in their early stages of develop-

ment. For example, the (subglacial) Glacier Drainage System model (GlaDS) [145] models the englacial system as a simple linear reservoir. More recently, Andrews et al. [3] suggest that moulin shape can change by 30% daily and 100% seasonally, resulting in noticeable changes in moulin water storage capacity and therefore subglacial channel dimensions. These results suggest that more work needs to be done on developing englacial hydrology models and in measuring moulins and englacial channels to validate the numerical models.

1.3.4 Subglacial hydrology models

Physically-based subglacial hydrology models already account for both distributed and channelized flow, including the Glacier Drainage System model [GlaDS; 145]; Subglacial Hydrology and Kinetic, Transient Interactions [SHAKTI; 132]; and Gagliardini and Werder [55]. See also de Fleurian et al. [40] for a comparison of models. These models provide important fundamental tools for linking ice dynamics with subglacial processes.

1.4 Format of the thesis

This thesis focuses on mathematically modelling supraglacial meltwater production and the supraglacial drainage system. It is organized as follows: Chapter 2 presents the paper “Application of an improved surface energy balance model to two large glaciers in the St. Elias Mountains, Yukon” [65] which has been published in the *Journal of Glaciology*. This paper describes a surface energy balance model to calculate summertime glacier melt rates. The model uses high resolution input data, including satellite-derived albedo, and a more complete treatment of downward solar radiation to improve on existing models’ capability to calculate surface melt. The model is applied to Kaskawulsh Glacier and Nàhùdäy (Lowell Glacier) in the St. Elias Mountains, Yukon, where the downstream water resources and ecological impacts of increasing surface melt are important.

Chapter 3 develops finite volume numerical methods that are applied to unstructured triangular meshes. This chapter compares several gradient reconstruction methods in terms of their accuracy and computational cost and describes how to apply one-dimensional finite volume methods on the network of triangle edges within the mesh. These methods are suitable for developing supraglacial hydrology models as distributed flow can occur in two dimensions across the triangular elements, and a connected network of supraglacial streams can form on edges.

Chapter 4 presents the paper “Modeling the dynamics of supraglacial rivers and distributed meltwater flow with the Subaerial Drainage System (SaDS) model” [64] which has been submitted to the Journal of Geophysical Research: Earth Surface. This paper describes the SaDS model, which was developed to improve upon existing supraglacial drainage models. SaDS is a dynamic model that represents distributed flow coupled with flow through supraglacial rivers using the numerical methods described in Chapter 3. The model explicitly calculates the melt out or incision of supraglacial channels in order to naturally form a river network without relying on existing satellite-derived drainage system maps. Due to the model’s mathematical formulation, SaDS represents seasonal and interannual changes in the drainage system, including supraglacial lake filling and draining. This paper shows that SaDS predicts moulin inputs with complex and heterogeneous seasonal dynamics. SaDS represents a significant step forward for supraglacial hydrology modelling and is an ideal tool for studying how supraglacial hydrology controls subglacial hydrology and therefore ice dynamics.

Chapter 2

Application of an improved surface energy balance model to two large valley glaciers in the St. Elias Mountains, Yukon

2.1 Introduction

The St. Elias Mountains, located along the Yukon-Alaska border, contain $\sim 33\,170\text{ km}^2$ of glacial ice [114], and are home to one of the largest icefields outside of the polar regions [31]. Glaciers in the Yukon/Alaska region are experiencing consistently negative mass balances ($-72.5 \pm 8.0\text{ Gt a}^{-1}$ from 2002–19; 28), high thinning rates (e.g. -0.4 to $-0.6\text{ m w.e. a}^{-1}$ from 2000–07; 53), and rapid reductions in areal extent [10]. These high thinning rates and strongly negative mass balance have caused the region to become one of the most significant contributors to global sea level rise, with only Arctic Canada expected to surpass the region’s contributions in the 21st century [68].

The retreat of mountain glaciers has significant local hydrological implications. As glaciers melt and retreat, meltwater runoff from glacierized basins typically increases until a maximum runoff value is reached (“peak water”), beyond which runoff decreases [70]. The timing and magnitude of peak water relative to current runoff varies globally and regionally. Huss and Hock [70] showed that $\sim 50\%$ of glacierized basins globally have already passed peak runoff, while Chesnokova et al. [25] showed that large, heavily glacierized basins in the Yukon have likely not reached peak water, but some smaller basins likely have. The

timing and volume of peak water is important for downstream communities who depend on the water resources provided by mountain glaciers. Therefore, it is important to be able to accurately model past, current and future glacier melt rates to predict water resource availability.

Glacier surface melt rates are commonly modelled using surface energy balance (SEB) models [e.g. 122; 44; 125; 47; 105; 14]. SEB models may be applied at both regional and local (i.e. individual glacier) scale. At the regional scale, SEB models can be used to predict ablation in regional mass balance models [e.g. 105]. Local scale models are often used to assess the sensitivity of glacier mass balance to climatic variations [e.g. 108; 46; 44], and to study in-depth the mass balance characteristics and melt volumes of individual glaciers [e.g. 147; 92; 47; 14]. These glacier-scale models are an important tool to examine the availability of meltwater runoff on the surface of glaciers, which has been linked to ice dynamics [71; 150; 62].

Glacier-scale SEB models have generally been successful at modelling melt rates when validated against in-situ observations, typically agreeing within $\sim 10\text{--}30\%$, including those applied to two small alpine glaciers in the Donjek Range of the St. Elias Mountains [147; 92]. However, recent models have four primary limitations:

1. The lack of a readily available high resolution (< 500 m) surface albedo product. Models often rely on highly-averaged parameterizations based on modelled snow cover, elevation, and mean clean ice albedo [e.g. 22; 92]. Surface albedo is one of the most sensitive parameters in SEB models [108; 44], leading to large uncertainties in modelled ablation (more than 35% uncertainty in the shortwave radiation component; 22).
2. Models sometimes neglect the possibility that the glacier surface may be shaded by adjacent valley walls and steep topography, or fail to properly account for cast shadows [110]. For example, this mechanism has been suggested by Thomson and Copland [140] to be responsible for non-uniform surface lowering on White Glacier, Arctic Canada. Shading has been included by a few energy balance studies [e.g. 5; 6; 7], but has not yet been combined with a high resolution, non-parameterized surface albedo to achieve the most accurate representation of shortwave radiation absorption.
3. Models often neglect to account for supraglacial debris. Sufficiently thick debris cover drastically lowers surface albedo while locally insulating the glacier surface and reducing melt rates [120; 135]. This is an area of considerable current research, with much focus on debris-covered glaciers in the Himalayas [e.g. 85; 103; 99]. Steiner

et al. [135] found that debris cover on Lirung Glacier, Nepal, locally reduced energy fluxes transferred to the glacier surface by 10-100%. Without careful treatment of debris cover, SEB models which take spatially variable surface albedo into account will compute elevated melt rates over debris compared to clean ice due to the lower surface albedo, leading to significant model errors over these regions. Melt models for debris covered glaciers highlight the large difference in melt rates over debris-covered and dirty ice. For example, Fyffe et al. [54] found that supraglacial debris cover reduced total melt volumes on Miage Glacier in the French Alps by 60%.

4. Models that assume the ice surface is at the melting point may overestimate melt rates by $\sim 10\%$ [60; 113; 146]. A subsurface model is necessary to account for heat conduction through ice to compute surface temperature. Of the models that include a subsurface heat conduction model, the heat conduction is usually solved independently from the energy balance [e.g. 60; 113; 146; 92]. However, these processes are highly coupled, as the energy balance at the surface depends on the surface temperature, controlled by upwards longwave radiation and sensible heat flux, while the subsurface temperature depends on the energy available for warming at the surface along with the deeper thermal gradient driven by long-term ice temperature conditions. More complicated models that account for supraglacial lake formation and firn densification have solved these processes simultaneously [e.g. 24], but this approach has not been adopted by most energy balance models.

We present an improved distributed surface energy balance model that addresses these four limitations, and therefore allows for more accurate quantification of the spatial distribution of melt. We apply the model to Kaskawulsh Glacier and Nàhùdäy (Lowell) Glacier in the St. Elias Mountains, Yukon, using in-situ meteorological data and validate outputs against measured surface ablation. The improved model can be used to investigate the meltwater volumes of individual glaciers with greater accuracy, and has the potential to be upscaled to the entire St. Elias Mountains to quantify the controls on melt at regional scale. Future application of the melt model in combination with a supraglacial meltwater routing model may provide important evidence for constraining the drivers of glacier surges in this region.

2.2 Study area

The St. Elias Mountains are a high elevation (up to 5959 m asl.) mountain range located in southwest Yukon and southeast Alaska (Figure 2.1). Glaciers in the St. Elias Mountains

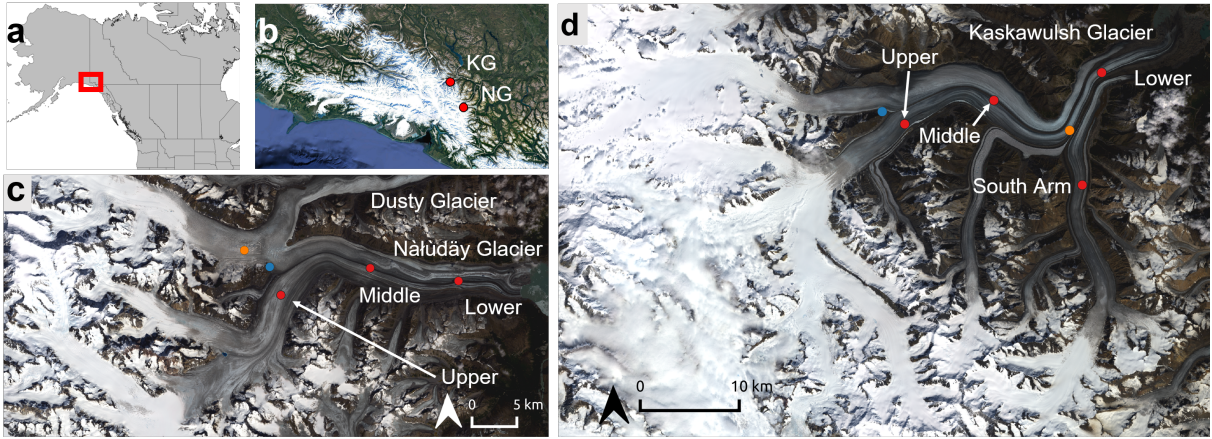


Figure 2.1: Nàhùdäy (Lowell) Glacier and Kaskawulsh Glacier in the St. Elias Mountains, Yukon. (a) Location of the St. Elias Mountains on the border of Alaska, USA and Yukon, Canada. (b) Location of Kaskawulsh Glacier (KG) and Nàhùdäy Glacier (NG) within the St. Elias Mountains. Google Earth, Image: Landsat/Copernicus, IBCAO. (c) False colour composite image of Nàhùdäy Glacier from 3 August 2015 Landsat 8 scene. Blue dot indicates the location of weather station AWSN1. (d) False colour composite image of Kaskawulsh Glacier from 3 August 2015 Landsat 8 scene. Blue dot indicates the location of co-located weather stations AWSK1 and AWSK2. Red dots in (c) and (d) indicate the locations of surface ablation measurements and on-ice HOBO temperature and relative humidity sensors; orange dots indicate the locations of albedo measurements made by Williamson et al. [149]

are diverse, representing a range of sizes, elevations, and dynamic behaviours [31], including a high concentration of surge-type glaciers [96; 32]. Surge-type glaciers are characterized by a semi-regular oscillation between two dynamic regimes. In the quiescent phase, glacier flow is slower than the balance velocity and mass builds up in a reservoir zone. In the active phase, flow speeds dramatically increase, typically by more than an order of magnitude, and mass is rapidly transferred down-glacier [39]. While the exact mechanisms are not fully understood, surges are suggested to be controlled by subglacial hydrology, bed characteristics, thermal conditions [39], and enthalpy budgets [124; 17].

Glaciers in this region show a range of surge characteristics. Nàhùdäy Glacier [18] and Dañ Zhúr (Donjek) Glacier [79] have rapid surge cycles (~ 10 – 13 year quiescent phase, ~ 1 – 2 year active phase over the past 50 years), while Trapridge Glacier has surge phases lasting decades [30]. Moreover, successive surges on a single glacier show distinct characteristics; Kochtitzky et al. [79] showed that surges on Donjek Glacier have varying patterns of surge

initiation and termination. While more work is necessary to understand the full details of surge mechanisms in the St. Elias Mountains, the quantity and distribution of surface meltwater delivered to the bed is potentially an important control on the surge dynamics [96; 18; 79].

We apply our improved SEB model to Kaskawulsh Glacier ($60^{\circ}44'37''$ N, $138^{\circ}57'9''$ W) and Nàhùdäy Glacier ($60^{\circ}19'21''$ N, $138^{\circ}27'42''$ W), and validate the predicted melt rates to in-situ measurements. These glaciers are located ~ 50 km apart on the eastern slope of the St. Elias Mountains (Figure 2.1) and experience a similar climatic regime. Kaskawulsh Glacier is a ~ 70 km long valley glacier ranging in elevation from ~ 2500 m asl. to ~ 820 m asl. at the terminus [50] with a complex network of tributary glaciers. Nàhùdäy Glacier is a similarly sized (~ 65 km long) valley glacier, with an elevation range from ~ 1500 m asl. in the St. Elias Icefields to ~ 500 m asl. at the terminus.

Despite their physical and climatic similarities, the glaciers differ in their dynamic regimes. Nàhùdäy Glacier is a surge-type glacier [31; 18], illustrated by extensive looped moraines in the lower regions (Figure 2.1). Recently, surges have been occurring more frequently (~ 12 years compared to ~ 15 year historical average) but with lower velocities than past surges, with the net result of less terminus displacement [18]. The last surge of Nàhùdäy Glacier was observed in 2009–10, and with the observed quiescent phase of ~ 12 years it is expected that another surge is nearly due (in ~ 2022 ; 18). In contrast, there is no evidence that Kaskawulsh Glacier is a surge-type glacier, although some of its tributaries do surge [31; 53]. The dynamic behaviour of Kaskawulsh Glacier is driven by meltwater inputs, but not in the cyclical way of Nàhùdäy Glacier. Instead, Kaskawulsh responds similarly to the majority of valley glaciers where seasonal velocity patterns are directly driven by meltwater inputs, with high velocities in the spring (up to 2–3x winter values) during periods of rapid melt of the winter snowpack [71; 150; 62; 2].

Both of these glaciers exert significant controls on regional hydrology. As recently as 1909, Nàhùdäy Glacier advanced during a surge phase to partially block drainage of the Alsek River, causing a major flood downstream when the ice dam broke [29]. In spring 2016, Kaskawulsh Glacier switched from draining north through the Slims River to the Bering Sea to a southerly drainage through the Alsek River to the Gulf of Alaska [128].

We have chosen to apply the SEB model to these two glaciers in order to compare meltwater inputs and how this may contribute to their dynamic regime. This work is part of a larger project to explain the dynamic regimes of Kaskawulsh and Nàhùdäy, and by modelling and comparing their surface melt we are taking an important step for this. Comparing the quantity and spatial distribution of meltwater on Kaskawulsh and Nàhùdäy Glaciers may provide evidence to constrain the sources of enthalpy [17] that contribute to

their contrasting dynamics.

2.3 Data and methods

2.3.1 Data

Digital elevation model

We drive the SEB model (described below) with digital elevation models (DEMs) extracted from 32 m resolution v3.0 ArcticDEM mosaic elevation data, where each mosaic tile is constructed from imagery acquired between 25 June 2011 and 17 March 2017 by the DigitalGlobe WorldView-1, WorldView-2, and WorldView-3 satellites [116]. The DEMs are used to calculate local slope and aspect in order to distribute solar radiation, and to distribute temperature by elevation according to the temperature lapse rate. The DEMs were cropped to contain the ablation zone of both glaciers as well as neighbouring peaks and ridges that are likely to shade the glacier surface at low solar angles (Figure 2.2).

We use glacier outlines from the Randolph Glacier Inventory Version 6.0 [121], and include only the area up to the equilibrium line altitude (ELA) as our model considers bare ice only. This approach neglects any meltwater transport downglacier from above the ELA, and so our melt volumes represent only in-situ melt below the ELA. By assessing the location of snowlines in Landsat 8 scenes used to derive surface albedo, we define the ELA to be 2100 m asl. on Kaskawulsh Glacier (previously identified as 1958 m asl in 2007; 53), and 1750 m asl. on Nalùdäy Glacier (previously identified as between 1520 to 1700 m asl. in 2010; 18).

Albedo

The SEB is highly sensitive to surface albedo [107; 44]. Parameterizations of surface albedo are able to represent average albedo sufficiently, but lack spatial variability [22]. Recent SEB models have modelled albedo as a function of snow cover [122; 105], or derived albedo from high resolution UAV imagery [14]. While both approaches can capture variability in surface albedo, the latter has the advantage of being derived from spatially distributed imagery. The use of UAV imagery, however, requires in-situ measurement and is not easily scalable. Instead, we derive surface albedo from Landsat 8 imagery.

Naegeli et al. [100] derived surface albedo for two glaciers in the Swiss Alps from both Landsat 8 and Sentinel-2 imagery, and validated the satellite-derived albedo with in-situ

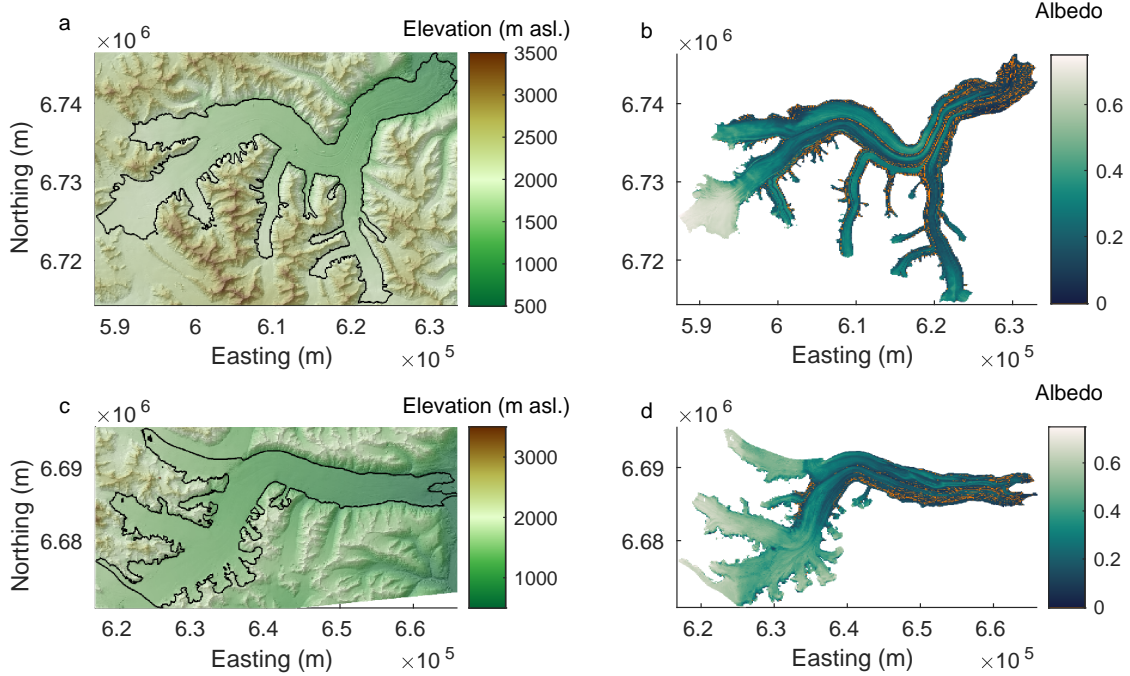


Figure 2.2: Study area and surface albedo. (a) Kaskawulsh Glacier DEM (ArcticDEM mosaic v3.0) covering the glacier as well as surrounding topography. (b) Albedo map of Kaskawulsh Glacier derived from the mean of five Landsat 8 scenes acquired on 15 July 2014, 18 July 2015, 3 August 2018, 18 August 2018, and 30 August 2019. Red pixels have been identified as debris-insulated by our debris algorithm. (c) Nàhùdäy Glacier DEM (ArcticDEM mosaic v3.0). (d) Albedo map of Nàhùdäy Glacier derived from five Landsat 8 scenes acquired on 15 July 2014, 3 August 2015, 23 July 2017, 8 August 2017, and 30 August 2019, with debris cover as in (b). All panels use UTM zone 7N projection.

measurements. Here we apply a simplified version of their method to derive surface albedo from Landsat 8 imagery, and describe our spatially distributed surface albedo maps. We convert the spectral reflectance from Landsat 8 to a broadband reflectance using the narrow to broadband conversion from Liang et al. [90] in order to approximate the surface albedo,

$$\alpha = 0.356B_2 + 0.130B_4 + 0.375B_5 + 0.085B_6 + 0.072B_7 - 0.0018, \quad (2.1)$$

where B_n is the surface reflectance in band n . Naegeli et al. [100] showed that this conversion neglects the anisotropy of reflection from snow and ice, and introduces up to a

10% bias in derived albedo values. Due to the complexity of accounting for the anisotropic reflections, we use this albedo directly as an input to the surface energy balance model and account for the bias when reporting our uncertainty in modelled melt volumes. We have chosen to derive surface albedo from Landsat 8 scenes rather than applying the MODIS albedo product directly due to their respective spatial resolutions. With Landsat 8 scenes, we derive surface albedo at 30 m resolution, while MODIS is only available at 500 m resolution.

We computed surface albedo for Kaskawulsh and Nàhùdäy from five snow and cloud free Landsat 8 scenes. For Kaskawulsh, we used scenes acquired on 15 July 2014, 18 July 2015, 3 August 2018, 18 August 2018, and 30 August 2019. Landsat 8 scenes acquired on 15 July 2014, 3 August 2015, 23 July 2017, 8 August 2017, and 30 August 2019 were used to derive albedo for Nàhùdäy Glacier. While seasonal trends in albedo have been found in other studies [e.g. 23], where albedo decreases throughout the season as more dirt and debris becomes exposed, we found no evidence of this pattern in the albedo derived from these Landsat scenes. Therefore, we averaged the five scenes to obtain an albedo more representative of the mean. Variation between albedo maps was up to 0.1 ($\sim 30\%$) on Kaskawulsh and 0.03 ($\sim 10\%$) on Nàhùdäy, with no clear annual trend.

Meteorological data

The SEB model is forced by in-situ meteorological data from a combination of automated weather stations (AWSs) and shielded Onset HOBO temperature and relative humidity (RH) U23 Pro sensors during the portion of the 2010–14 and 2018 melt seasons when the glacier surface is snow-free in the ablation area. From 2006–18, an AWS (AWSK1) on a nunatak adjacent to Kaskawulsh Glacier ($60^{\circ}44'32''\text{N}$, $139^{\circ}9'57''\text{W}$; Figure 2.1) provided temperature, pressure, incoming shortwave (SW) radiation, wind speed, and wind gust data. AWSK1 did not measure incoming longwave (LW) radiation. From 29 August 2017 until the station was decommissioned on 26 July 2018 the wind speed sensor malfunctioned, preventing application of the SEB model during the 2017 melt season. From 2018–20, AWSs on nunataks adjacent to Kaskawulsh Glacier (AWSK2, located beside AWSK1) and Nàhùdäy Glacier (AWSN1; $60^{\circ}18'45''\text{N}$, $138^{\circ}33'36''\text{W}$) provided temperature, pressure, RH, incoming and outgoing SW and LW radiation, wind speed, wind gust, and wind direction data (Figure 2.1). Unfortunately, the motherboard of AWSK2 failed on 11 May 2019 and was replaced on 5 September 2019, preventing us from modelling the 2019 melt season.

From 2010–14 four HOBOs on Kaskawulsh Glacier (Lower, Middle, Upper, South Arm; Figure 2.1, Table A.1) recorded temperature and relative humidity near the glacier surface. However, no data were recorded from 20 September 2010 to 13 August 2011. From 2017–19,

three HOBOS on Kaskawulsh and Nàhùdäy provided temperature and RH data (labelled Lower, Middle, and Upper stations on each glacier; Figure 2.1). Table S1 summarizes the temporal availability of HOBOS measurements, and Table S2 summarizes the available weather station data.

We assume that surface elevations and the positions of on-ice HOBOS sensors are static. These assumptions neglect that melt itself changes surface elevations, and that the on-ice sensors are advected down-glacier. Each of the HOBOS sensors was co-located with a dual-frequency global positioning system (dGPS) receiver, which recorded mean horizontal velocities of 141.3 to 164.3 m a⁻¹, and vertical velocities of -0.6 to -4.5 m a⁻¹, over the period 2010–14 at the Kaskawulsh stations [62]. The stations were reset to their original locations every few years, so were always within ~600 m horizontally and ~20 m vertically of their starting position over our 2010–18 study period. Horizontal and vertical velocities are similar on Nàhùdäy Glacier. The dGPS data from the middle station from 25 August–11 October 2017 show a mean horizontal velocity of 134 m a⁻¹ and vertical velocity of -7 m a⁻¹. Over our study period (27 July – 15 September, or 51 days), these velocities translate to a horizontal displacement of 19 m and a vertical displacement of -0.98 m.

Temperature and RH from the HOBOS are used to force the model as they provide measurements close to the ice surface, while the weather stations are on nunataks adjacent to the glacier and ~100 m above it. However, the AWS measurements of incoming SW and LW radiation and wind speed are used when available.

From 2010–14 when AWSK1 did not measure incoming LW radiation, we model incoming LW radiation using the Stefan-Boltzmann law,

$$LW_{in} = \varepsilon_a \sigma T_a^4, \quad (2.2)$$

where σ is the Stefan-Boltzmann constant, ε_a is the atmospheric emissivity, and T_a is the air temperature. Following Ebrahimi and Marshall [44] we parameterize atmospheric emissivity as a linear function of the relative humidity (RH) and the cloud fraction f . We calibrated the parameterization using the emissivity derived from incoming LW radiation and air temperature from AWSK2, finding

$$\varepsilon_a = 0.6007 + 0.0021RH + 0.2510f. \quad (2.3)$$

We apply the method of Crawford and Duchon [38] to compute the cloud fraction based on measured incoming SW radiation. Our parameterization captured most of the variability in the atmospheric emissivity in 2018. We found the standard deviation of the residuals (the difference between the measured LW radiation and modelled radiation using

the parameterization) to be 23 W m^{-2} , only slightly larger than the range 9 to 20 W m^{-2} reported by Ebrahimi and Marshall [43] for similar parameterizations.

Lapse rates

The air temperature in the SEB model is corrected for elevation by computing temperature lapse rates (Γ) on each glacier using data from the 2018 on-ice temperature sensors. On Kaskawulsh Glacier, we found that the lapse rate was $-3.98 \text{ }^\circ\text{C km}^{-1}$ (from 23 July 2018 to 17 March 2019; $R^2 = 0.87$), while on Nàhùdäy Glacier the lapse rate was $-3.26 \text{ }^\circ\text{C km}^{-1}$ (from 27 July 2018 to 20 November 2018; $R^2 = 0.89$).

In addition to temperature, pressure is modelled by assuming hydrostatic equilibrium, and density is computed according to the ideal gas law for moist air, accounting for variations in temperature and pressure with elevation. The resulting expressions are

$$T_a = T_{a,0} - \Gamma \Delta z \quad (2.4)$$

$$P = P_0 - \rho_a g \Delta z \quad (2.5)$$

$$\rho_a = \frac{P_0 - p_v}{R_d T_a + g \Delta z} + \frac{p_v}{R_v T_a(z) + g \Delta z}, \quad (2.6)$$

where Δz is the elevation difference between a point in the DEM and the elevation that the reference state ($T_{a,0}, P_0$) was measured at, R_d and R_v are the dry air and water vapour ideal gas constants, T_a is the temperature in kelvin, and p_v is the temperature dependent vapour pressure.

Surface ablation measurements

We evaluate the performance of the SEB model by comparing modelled ablation rates to in-situ surface ablation measurements. Surface ablation measurements are available from two separate periods. From 2010–14, two Judd Communications LLC Ultrasonic Depth Sounders (UDSs) were installed on Kaskawulsh Glacier to automatically record changes in surface height (Figure 2.3). The UDSs were initially installed at the upper and south arm stations; the south arm UDS was moved to the lower station in August 2013. The UDS data show significant noise in 2011, 2012, and 2013. In 2010 we have high quality UDS data at the upper and south arm stations, and in 2014 we have high quality data at the upper and lower stations. These years are where we have the best ability to quantify model performance.

Since 2017, time lapse cameras recorded hourly images of ablation stakes marked with stripes every 5 cm on both Nàhùdäy and Kaskawulsh. Images were used to calculate surface ablation at several locations on each glacier. These surface ablation data are used to evaluate model performance (Figure 2.4, Table A.1).

On Nàhùdäy Glacier, the middle time lapse camera rotated so that the ablation stake was out of the frame from 8 August 2018 onwards. To obtain a complete melt record, we therefore compute the mean ratio of melt at the middle and lower stations when we have both melt observations, and multiply the melt measurements at the lower station by this ratio. We found the mean melt ratio was 0.91 with standard deviation 0.14, and with correlation between the measurements at the middle and lower stations of 0.998, indicating that this approach provides a robust estimate of ablation at the middle stake location. The extended melt record is shown in Figure 2.4, and is used in Tables A.2 and A.4 to quantify model performance.

2.3.2 Glacier surface shading

Shading of the glacier surface by valley walls and neighbouring topography is an important component of high resolution SEB models [110]. This mechanism is inherently non-local, requiring the DEM to cover any nearby prominent ridges, and especially up to the ridges on the valley walls containing the glacier, highlighting one advantage of the complete spatial coverage provided by the ArcticDEM mosaic data. It is important to note the distinction between calculating shadows cast by neighbouring topography, which depend on the time of day and day of year, and approximating shading by the sky view factor. The sky view factor (SVF) is the ratio of the sky area that is visible (e.g. unobstructed by surrounding terrain) to the complete half-hemisphere area. Since the SVF is constant over time and does not depend on the solar geometry, using the SVF to compute shading neglects the time dependence of shading and the importance of the aspect of the topography obstructing the view (e.g. the difference between a north- and south- facing cliff adjacent to a glacier). Instead of using the SVF, we directly compute shading for our DEMs.

We implement an algorithm to shade DEMs based on the description by Corripio [37] and Olson and Rupper [110]. The algorithm computes shadows cast by high-relief topography for a given solar position, which is determined by the time of day, day of year, and latitude. The algorithm is fully described by Corripio [37], so here we provide only a brief description. The algorithm traces solar rays across the DEM, computing the projection of each cell onto a plane perpendicular to the incoming solar rays, labelled the solar plane (see Figure 6 of 37). Starting from the edge of the DEM closest to the sun, the algorithm

traces solar rays across the DEM. A cell is shaded when its projection onto the solar plane is less than any of the previously computed projections along the solar ray. For cells that are determined to be in the shade, the direct incoming SW radiation is set to zero.

2.3.3 Debris insulation

In this section we present an automated algorithm to delineate regions on the glacier that are insulated by debris cover. Our distributed albedo maps are sufficiently high resolution to capture low albedo over regions of dirty ice and debris cover, and so if we were to neglect the spatial distribution of thick debris on the glacier surfaces we would overestimate melt in regions of thick debris cover.

When debris reaches a critical thickness (for example, ~ 0.05 m in the laboratory experiments of [120](#)), the debris acts to insulate the glacier surface and reduce melt rates [e.g. [120](#); [119](#); [135](#)]. During the day when energy balance is positive, the debris surface warms and builds a steep thermal gradient within the debris layer, maintaining near freezing temperatures at the debris-ice interface and reducing energy transferred to the glacier surface. Overnight, the debris surface efficiently releases the heat absorbed during the day back to the atmosphere. Kraaijenbrink et al. [[85](#)] observed this diurnal cycle on Lirung Glacier in Nepal, showing that debris surface temperatures increase to above 15°C during the day, but was thick enough to prevent heat conduction through to the ice surface and reduce glacier melt rates directly under the debris by 10-100% [[135](#)]. High surface temperatures invert near-surface temperature profiles and introduce atmospheric instability over debris during the day, significantly altering turbulent heat fluxes over the debris as well as atmospheric circulation patterns over the entire glacier basin when enough of the surface is covered by debris [[103](#); [35](#)]. SEB models have been adapted to accurately model melt rates of debris covered glaciers [e.g. [119](#); [54](#); [125](#)], showing good agreement with ablation stake measurements. Since our glaciers are not heavily debris covered ($\leq 7\%$) and we do not have data on the thickness of debris to apply a heat conduction model within the debris layer, we make the approximation that no melt occurs where the surface is insulated by debris as identified by the algorithm below.

Our algorithm is based on analyzing the DEMs and surface albedo maps to find medial moraines, which are the dominant type of debris cover on our study glaciers. The albedo maps allow us to find regions with debris cover or dirty ice, and locally elevated regions in the DEMs show where this debris cover is thick enough to reduce melt rates.

For each point in the DEM, we calculate the second derivative of the surface elevation in the across glacier direction, which provides information on how the surface slope changes

in the across-glacier direction (surface curvature),

$$\partial_{\mathbf{y}\mathbf{y}}\eta = \mathbf{y}^T H \mathbf{y}, \tag{2.7}$$

where H is the Hessian matrix of the elevation η and \mathbf{y} is a unit vector in the across-glacier direction. We expect negative (downwards) curvature where the surface has been insulated, representing convex surface, since the debris-insulated surface is higher than its surroundings [99].

Therefore, we identify a point as covered by debris sufficiently thick to insulate the glacier surface if the following three conditions are met:

1. $\alpha < \bar{\alpha}$ to find regions with lower than average albedo,
2. $\alpha < \alpha_{\max}$ to limit to regions with albedo lower than the maximum allowed debris albedo,
3. $\partial_{\mathbf{y}\mathbf{y}}\eta < \gamma$ to find regions elevated from their surroundings.

Condition (1) finds regions with albedo lower than the average albedo $\bar{\alpha}$, computed using a 1 km moving average, while condition (2) ensures we only consider regions with albedo less than a specified maximum debris albedo threshold $\alpha_{\max} = 0.125$. Together, these conditions find dirty and debris covered regions. Condition (3) is used to distinguish regions of dirty ice with enhanced melt from regions of debris cover that are thick enough to insulate the surface and reduce melt.

The surface curvature threshold γ controls the typical magnitude of surface curvature of debris cover. The curvature threshold is always negative, as a negative second derivative implies the region is elevated compared to its surroundings. We use γ as a tuning parameter while keeping the value of γ within the expected range. For a medial moraine of width 100m and height 10m, we expect $\gamma \approx -4 \times 10^{-4} \text{ m}^{-1}$. γ is tuned so that debris cover matches visible regions of debris in the Landsat 8 scenes and the and the 32 m resolution ArcticDEMs, as well as field observations. In the case of Kaskawulsh and Nàhùdäy the curvature parameter likely differs due to their different dynamic regimes. Each time Nàhùdäy surges, the surface becomes heavily crevassed and fractured, effectively erasing any elevation difference between clean ice and debris-covered ice. Following the surge, differential ablation slowly builds up the elevation difference again. This results in small elevation differences between debris-covered and clean ice compared to Kaskawulsh, where elevation differences are continually enhanced.

When applied to Nàhùdäy Glacier, the algorithm identified the primary medial moraine extending from the junction with Dusty Glacier to the terminus, along with several longitudinal ridges of debris cover on the southern half of the main trunk near the lower and middle stations (Figure 2.2). Several debris patches and longitudinal features were also identified along both margins almost up to the elevation of the upper station. Significant debris cover was found to be distributed throughout the terminus region below the lower station, which matches with field observations. Overall, we found 11.9 km² of the 363 km² glacier surface (3.3%) to be insulated by debris. We found the debris algorithm had the best ability to classify debris cover when using a curvature threshold $\gamma = -1.5 \times 10^{-4} \text{ m}^{-1}$ on Nàhùdäy Glacier. This is in line with our expectation of lower elevation differences between debris-insulated and clean ice due to the surging behaviour of Nàhùdäy.

On Kaskawulsh Glacier, we found that a surface curvature threshold value of $\gamma = -4 \times 10^{-4} \text{ m}^{-1}$ clearly identified the primary medial moraines originating from the junction of the north and central arms, and the junction with south arm. Similar to Nàhùdäy Glacier, we found debris patches distributed across the terminus region (Figure 2.2). In total, we found 26.9 km² (7.0%) of the 385 km² surface of Kaskawulsh Glacier to be insulated by debris. Automatically derived moraine locations matched with the locations of moraines visible in Landsat 8 imagery and with field observations.

2.3.4 Subsurface model

The ice surface temperature is an important input to the SEB model, as neglecting subsurface heat flux may lead to overestimation of total melt by 0.8 to 10.4%, especially at high elevations [113]. Therefore, we include a simple one-dimensional subsurface heat conduction model (SSM) based on that of Greuell and Konzelmann [60]. The model is further simplified by assuming all energy absorption and melting is in the surface layer [146; 147; 24]. The heat conduction model only considers vertical fluxes since horizontal heat flux is negligible due to small horizontal temperature gradients.

Under these assumptions, the subsurface model may be written in the conservation law form

$$\rho_i c_{pi} \frac{\partial T_i}{\partial t} + \frac{\partial q}{\partial z} = 0, \quad (2.8)$$

where ρ_i is the density of ice, c_{pi} is the specific heat capacity of ice, T_i is the subsurface ice temperature, and z is the depth below the surface. The heat flux q is given by

$$q = -k_i \frac{\partial T_i}{\partial z}, \quad (2.9)$$

where k_i is the heat conductivity of ice. The top boundary condition is the heat flux at the surface, which is equal to the energy available to warm the the surface. We partition the total heat flux Q_{net} into energy used to melt ice, Q_M , and energy used to warm the surface layer, Q_T . The bottom boundary condition is a combination of requiring the bottom temperature to be equal to the 12 m ice temperature and a zero heat flux condition, so that:

$$-k_i \left. \frac{\partial T_i}{\partial z} \right|_{z=0} = Q_T \quad (2.10)$$

$$T(z = H) = T_{12m} \quad (2.11)$$

$$q(z = H) = 0, \quad (2.12)$$

where we use the 12 m depth ice temperature $T_{12m} = -3^\circ\text{C}$ measured on a small tributary glacier adjacent to Kaskawulsh in September 2008 by Wheler and Flowers [147], as no more recent temperature measurements exist for Kaskawulsh or Nàlùdäy. Q_T is the energy used to warm the surface, computed according to

$$Q_T = \begin{cases} Q_{\text{net}} & T_s + \Delta T < 0 \\ -\frac{h\rho_i c_{pi} T_s}{\Delta t_{SSM}} & T_s < 0, T_s + \Delta T > 0 \\ 0 & T_s \geq 0, \end{cases} \quad (2.13)$$

with surface temperature T_s , layer thickness h , and timestep Δt_{SSM} . The maximum warming potential ΔT is defined as the amount the surface layer would warm within a model timestep of length Δt_{SSM} with total heat flux at the surface Q_{net} ,

$$\Delta T = \frac{\Delta t_{SSM} Q_{\text{net}}}{\rho_i c_{pi} h}. \quad (2.14)$$

The energy available for melting is then computed as

$$Q_M = Q_{\text{net}} - Q_T. \quad (2.15)$$

2.3.5 Surface energy balance model

Our energy balance model is based on that of Ebrahimi and Marshall [44] and Bash and Moorman [14]. The net energy flux at the surface (Q_{net}) is computed from the net balance of SW (Q_{SW}) and LW (Q_{LW}) radiation, and latent (Q_E) and sensible (Q_H) turbulent heat fluxes,

$$Q_{\text{net}} = Q_{SW} + Q_{LW} + Q_E + Q_H. \quad (2.16)$$

Shortwave radiation

Incoming shortwave radiation is modulated by surface slope, aspect, and solar geometry. The method to distribute solar radiation is based on, and is functionally equivalent to, the model employed by Bash and Moorman [14], but has been reformulated in terms of local unit vectors to better integrate with the DEM shading algorithm [37]. The unit solar vector \mathbf{s} is computed based on the time of day and day of year [37]. The local incident shortwave radiation I' is then computed from the global incident radiation I_0 , where shaded cells have $I_0 = 0$, as

$$I' = (\mathbf{n} \cdot \mathbf{s})I_0, \quad (2.17)$$

where \mathbf{n} is the upward unit normal perpendicular to the glacier surface. Following Bash and Moorman [14], we add a diffuse radiation component to all cells,

$$I_{\text{diff}} = 16\psi^{1/2} - 0.4\psi, \quad (2.18)$$

where ψ is the solar angle of elevation in degrees. The net SW radiation flux is

$$Q_{SW} = (1 - \alpha)I' + I_{\text{diff}}, \quad (2.19)$$

where α is the local surface albedo derived from Landsat 8 scenes.

Longwave radiation

Outgoing LW radiation is computed from the surface emissivity and surface according to the Stefan-Boltzmann law,

$$LW_{out} = \epsilon_s \sigma T_s^4, \quad (2.20)$$

where σ is the Stefan-Boltzmann constant, ϵ_s is the ice emissivity, and T_s is the surface temperature modelled by the subsurface model. Incoming LW radiation from weather stations is used where available (AWSK2 and AWSN1), and is modelled for AWSK1 (Eq. 2.2). Incoming LW is distributed according to air temperature,

$$LW_{in} = LW_{in0} \frac{T_a^4}{T_{a,0}^4}, \quad (2.21)$$

where LW_{in0} is the LW radiation measured by the AWS, T_0 is the temperature recorded by the AWS, and T_a is the distributed air temperature (Eq. 2.4). The relative change in incoming LW radiation is quite small since the temperature only varies by a few degrees across the glacier. With the largest lapse rate that we calculated ($-3.98 \text{ }^\circ\text{C km}^{-1}$), the difference in temperature across Kaskawulsh Glacier is $\sim 3 \text{ }^\circ\text{C}$, corresponding to a change in incoming LW radiation of $\sim 4.5 \%$ or $\sim 13 \text{ W m}^{-2}$. The net longwave radiation is simply

$$Q_{LW} = LW_{in} - LW_{out}. \quad (2.22)$$

Turbulent heat fluxes

Following [44; 14], the sensible heat flux Q_H and latent heat flux Q_E are

$$Q_H = \rho_a c_p k^2 U \left(\frac{T_a(z) - T_s}{\ln(z/z_0) \ln(z/z_{0H})} \right) \quad (2.23)$$

$$Q_E = \rho_a L_v k^2 U \left(\frac{q_a(z) - q_s}{\ln(z/z_0) \ln(z/z_{0E})} \right), \quad (2.24)$$

where c_p is the constant pressure heat capacity of air, k is von Karman's constant, L_v is the latent heat of vaporization of water, and z_0 , z_{0H} , z_{0E} are the momentum, heat, and moisture roughness lengths. The parameter z is the height above the glacier surface of the air temperature and specific humidity measurements (Table A.3). $T_a(z)$, $q_a(z)$ are the air temperature and specific humidity measured by on-ice HOBOS at a height z above the glacier surface, after distributing quantities by elevation according to the lapse rates, U is the wind speed measured at the AWSs, q_s is the specific humidity at the glacier surface, and ρ_a is the density of air. These parameterizations were developed for horizontal,

uniform surfaces [47] but are commonly applied to rough, inhomogeneous glacier surfaces [e.g. 4; 67; 44; 14]. While these parameterizations have limited accuracy, the difficulty of directly measuring turbulent energy fluxes [e.g. 47] makes them an important component of distributed energy balance models.

The surface energy balance (Eq. 2.16) depends on the surface ice temperature, while the temperature evolution within the ice depends on the surface energy balance through the boundary conditions (Eq. 2.10). We avoid an iterative scheme [e.g. 60; 146; 147] by formulating the models as a coupled system of differential equations [e.g. 24]. Differentiating the surface energy balance model (Eq. 2.16) with respect to time, assuming that external forcing is constant within each time step, we find an evolution equation for the net heat flux at the surface that depends on the surface temperature. We therefore combine the SEB and SSM models into the coupled system

$$0 = \rho_i c_{pi} \frac{\partial T_i}{\partial t} + \frac{\partial q}{\partial z} \quad (2.25)$$

$$\frac{dQ_{\text{net}}}{dt} = -4\epsilon_s T_s^3 \frac{\partial T_s}{\partial t} - \frac{\rho_a c_p k^2 u}{\ln(z/z_0) \ln(z/z_{0H})} \frac{\partial T_s}{\partial t}. \quad (2.26)$$

The complete system is given by equations (2.25) and (2.26), combined with (2.9) and boundary conditions (2.10–2.12).

2.3.6 Model implementation

The model is implemented with two different time steps. The first time step, Δt_{AWS} , is set by the frequency of the AWS data (Table A.3). For AWSK1, this time step is 1 hour; for AWSK2 and AWSN1 the time step is 2 hours. The second time step, Δt_{SSM} , corresponds to the subsurface model for which we use 15 minutes. During each time step Δt_{AWS} we assume the meteorological variables are constant. We then solve the coupled SEB and subsurface model equations (Eq. 2.25 and 2.26) with a timestep Δt_{SSM} , and compute the average surface temperature, heat used for warming the ice, and heat used for melting ice over the long time step Δt_{AWS} . These average quantities are used to compute the total amount of melt during the time step Δt_{AWS} . For instance, for AWSK2 and AWSN1 we take eight 15-minute timesteps in the subsurface model for each 2 hour SEB interval. At the end of each AWS time step, the average melting heat flux Q_M is used to melt ice in the surface layer.

Spatial derivatives are implemented using finite differences on a uniform grid. The grid extends down to 12 m depth with a uniform layer thickness of 1 m. Following Buzzard et al. [24] we assume that all SW radiation is absorbed by the surface layer. This approach neglects the fact that SW radiation exponentially decays with depth, warming and melting the subsurface layers [60]. However, with our layer thickness of 1 m, only $\sim 5\%$ of SW radiation would penetrate to the second layer [60]. Therefore, we believe that this approximation is valid considering the simplifications it allows in the model formulation.

We tested the sensitivity to the vertical grid spacing by reducing the layer depth from 1 to 0.5 m and reducing the timestep from 15 to 5 min. The maximum absolute difference in melt volumes was less than 1%, and so we believe our timestep and layer depth are sufficiently small to resolve the subsurface thermal structure of these two glaciers.

We model surface melt on Kaskawulsh Glacier starting from the time that the glacier surface is snow-free at the upper station (~ 1700 m asl.) By analyzing 12 Landsat 8 images from June through August 2014–19, we determined that Kaskawulsh Glacier is typically snow free at the upper station by 23 June (Figure A.1). The model is run from this date until the end of the melt season, which we define as 15 September, for a total season length of 85 days, subject to data availability constraints. This date for the end of the melt season is in agreement with Herdes [62], who found the melt season ended as early as 11 September at the upper station of Kaskawulsh in 2011. We only have AWS data on Nàhùdäy Glacier beginning in late July of 2018, by which time it was snow free and so we run the model from this date until 15 September. Each 85-day model run takes ~ 12 h on an Intel[®] Core[™] i5-6300U CPU with 8GB RAM.

2.3.7 Model evaluation and uncertainty estimation

We evaluate model performance quantitatively by computing the total model error (ME) between modelled and measured ablation (using UDS data or time-lapse ablation stake measurements) at the end of the melt season and the mean ablation rate error (ARE) at each station. The ARE is defined as the difference between the slope of the best-fit lines through the modelled and observed melt timeseries. The ME and ARE are complementary metrics in that they are each robust with respect to different types of errors. ME is not impacted by errors in the middle of the melt season, and is controlled by the total error at the end of the model run. In contrast, ARE measures the melt trend throughout the entire modelled period, and is not significantly impacted by small variations in the first and last few days of the season. We report these metrics at each measurement location by extracting the model values in the cell containing the station.

We estimate uncertainty in modelled melt volumes based on uncertainties in the input data. In particular, we account for uncertainties in our derived surface albedo maps, our modelled incoming longwave radiation for AWSK1, our wind speed measurements (since they do not reflect measurements directly on the ice), and our sub-surface ice temperature.

The uncertainty in surface albedo is a result of our simple method to derive albedo from surface reflectance data. Naegeli et al. [100] showed that neglecting the anisotropy correction when deriving surface albedo from Landsat 8 surface reflectance can result in up to a 10% bias in derived surface albedo values, depending on surface slope and aspect, as well as solar geometry. Therefore, we perturb our derived albedo values by 10% to derive an uncertainty in modelled melt totals related to our neglecting the anisotropy correction. As albedo varies between DEM cells, the resulting albedo uncertainty is uniquely defined in each cell.

We include an uncertainty contribution from LW radiation when we have had to model incoming radiation. We tuned a parameterization of emissivity using data from AWSK2, where there was a standard deviation of 23 W m^{-2} in the residuals between our modelled and measured incoming LW radiation. Therefore, we assume that there is an uncertainty of 23 W m^{-2} in our modelled incoming LW radiation during this time period, and we compute the corresponding change in surface melt, assuming the uncertainty is uniformly distributed across the glacier surface.

Wind near the surface of a melting glacier is typically dominated by a thin layer ($< 100 \text{ m}$) of katabatic winds [141; 109], and so we expect a non-negligible difference in wind speed between the AWS measurements and the true wind speed near the glacier surface. However, the wind speed profiles have been shown to be consistent through the melt season [109]. We see from Eq. 2.23 that the wind speed only impacts the turbulent heat fluxes. These are also the fluxes impacted by the momentum roughness length. Thus, we consider tuning the roughness length a proxy for adjusting the wind speed. Since we have tuned the roughness length to achieve the best fit with six years of in-situ measurements, we have accounted for any systematic bias in the wind speed. Therefore, we do not include an uncertainty contribution due to the wind speed.

The final uncertainty contribution is from the ice temperature at 12 meters depth. We have used the value reported by Wheler and Flowers [147] measured on a nearby glacier as no recent data is available on the temperature structure of Kaskawulsh and Nàhùdäy Glaciers. As the measurement was taken at a higher elevation than our study sites, we do not expect the subsurface temperature on Kaskawulsh and Nàhùdäy to be below $-3 \text{ }^\circ\text{C}$, and so we assess the sensitivity of modelled melt totals to perturbing the subsurface ice temperature to the maximum value $0 \text{ }^\circ\text{C}$. Averaged over the 2012 melt season, the mean

difference in net heat flux over Kaskawulsh Glacier was -2.3 W m^{-2} , or -0.052 m w.e. over the period 23 June–15 September. We use this heat flux to compute the uncertainty in modelled melt due to the subsurface ice temperature in each melt season.

We compute the total uncertainty in modelled melt volumes as the combination of the contributions due to albedo (δ_α), deep ice temperature ($\delta_{T_{12m}}$), and LW radiation (when we have modelled incoming LW radiation; δ_{LW}),

$$\delta = \sqrt{\delta_\alpha^2 + \delta_{T_{12m}}^2 + \delta_{LW}^2}. \quad (2.27)$$

We report modelled melt values as melt \pm uncertainty (δ) at each measurement location.

2.4 Results

2.4.1 Albedo maps

The surface albedo maps (Figure 2.2) agree well with existing in-situ measurements and with MODIS surface albedo. Williamson et al. [149] measured in-situ surface albedo along several transects on Kaskawulsh Glacier (centered on 60.72°N , 138.82°W) on 9 August 2015 and Nàlùdäy Glacier (centered on 60.33°N , 138.61°W) on 16 August 2015, including along at least one 500 m long transect, and compared these in-situ measurements to the MODIS MOD10A1 snow albedo product. We compare these in-situ and MODIS albedo values from Williamson et al. [149] to our albedo maps derived from Landsat 8 scenes acquired on 3 August 2015 (6 days before measurements on Kaskawulsh and 13 days before measurements on Nàlùdäy). To approximate the in-situ sampling method, we compute the mean, range, and standard deviation of our satellite-derived albedo values within a 500 m square centered on the reported coordinate (Table 1). Note that a single $500 \text{ m} \times 500 \text{ m}$ MODIS pixel was used for each glacier, so we are unable to report the range or standard deviation.

The mean Landsat-derived surface albedo agrees with the MODIS albedo very well, with differences of 4.8% on Kaskawulsh and 0.3% on Nàlùdäy. The standard deviation of the Landsat-derived albedo also agrees well with the in-situ measurements. However, the mean and extreme albedo values disagree between the in-situ and Landsat methods. This is not surprising since we have more than 250 Landsat pixels within each of the measured plots, while the in-situ measurements had only 11 samples on Kaskawulsh and 9 on Nàlùdäy [149]. Moreover, physical hazards (streams, crevasses, etc.) influenced the locations of the in-situ transect but are captured within the remotely sensed data. Considering these limitations,

Table 2.1: Summary statistics of surface albedo within a single $500\text{ m} \times 500\text{ m}$ MODIS pixel footprint on Kaskawulsh and Nàhùdäy derived from Landsat 8 scenes on 3 August 2015 compared with values reported by Williamson et al. [149] from MODIS MOD10A1 snow albedo data and in-situ measurements

Glacier	Method	Mean	σ	Min	Max
Kaskawulsh	Landsat 8	0.205	0.100	0.051	0.400
	MODIS	0.215	N/A	N/A	N/A
	<i>in-situ</i>	0.281	0.100	0.105	0.412
Nàhùdäy	Landsat 8	0.319	0.077	0.154	0.588
	MODIS	0.318	N/A	N/A	N/A
	<i>in-situ</i>	0.426	0.072	0.324	0.580

the difference in mean and range between the satellite-derived and in-situ measured albedo is not surprising.

2.4.2 Kaskawulsh Glacier, 2010–14

We applied our SEB model to Kaskawulsh Glacier during the 2010–14 melt seasons (Figure 2.3). Modelled melt values for the five melt seasons (including three complete melt seasons: 2012–14) and four locations on the glacier are given in Table 2.

At the lower station modelled melt averaged over the 2012–14 full 85 day melt seasons was $3.82 \pm 0.63\text{ m w.e.}$, or $0.045\text{ m w.e. day}^{-1}$. At the middle station modelled melt averaged $3.67 \pm 0.62\text{ m w.e.}$, or $0.043\text{ m w.e. day}^{-1}$. At the upper station modelled melt averaged $3.16 \pm 0.62\text{ m w.e.}$, or $0.037\text{ m w.e. day}^{-1}$. At the south arm station modelled melt averaged $3.43 \pm 0.60\text{ m w.e.}$, or $0.040\text{ m w.e. day}^{-1}$. Modelled melt was highest in 2013, reaching $4.12 \pm 0.63\text{ m w.e.}$ at the lower station, or $0.048\text{ m w.e. day}^{-1}$. Distributed melt totals for the entire modelled region (Figure 2.2) from 2012–14 averaged $3.15 \pm 0.61\text{ m w.e.}$ with a standard deviation of 0.84 m w.e. , equivalent to a daily melt rate of $0.037\text{ m w.e. day}^{-1}$.

Agreement between modelled melt and the UDS surface elevation data from 2010–14 is quantified by the ME and ARE in Table A.4. We have the best ability to quantify model performance in 2010 and 2014 when the UDS data are high quality. For the 2010 melt season, ME is -0.08 m (-3.0%) and ARE is $-0.0037\text{ m w.e. day}^{-1}$ (-6.8%) at the upper station, while ME is 0.52 m (16%) and ARE is $0.0094\text{ m w.e. day}^{-1}$ (17.5%) at the south arm station. In 2014, ME is -0.13 m (-3.6%) and ARE is $-0.0056\text{ m w.e. day}^{-1}$ (-11.7%) at the upper station, while ME is 0.29 m (7.1%) at the lower station and ARE is $0.0017\text{ m w.e. day}^{-1}$

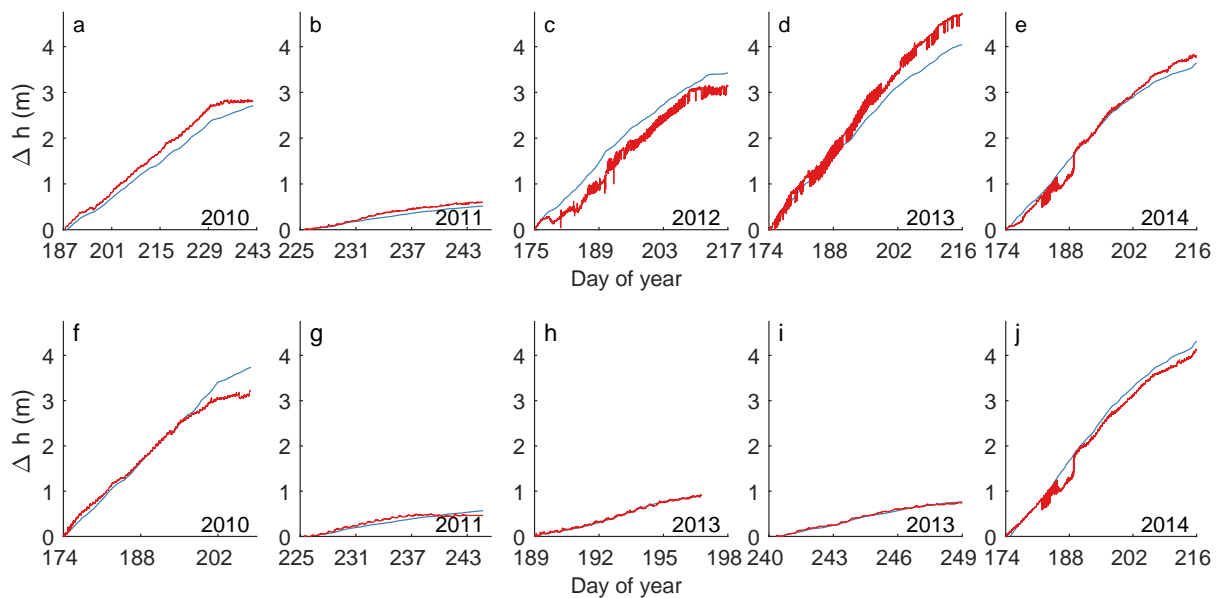


Figure 2.3: Modelled (blue) surface ablation compared to ultrasonic depth sounder (UDS) measurements (red) on Kaskawulsh Glacier, 2010–14 at the (a–e) upper station, (f–h) south arm station, and (i–j) lower station. Note the difference in modelled period between years.

(3.2%) at the lower station. The high ARE at the upper station is at least partially due to the noisy UDS data in mid July which may be a result of instrument error. In these years, ME is within ~ 0.30 m ($\sim 7\%$). Modelled melt agrees with measurements within our estimated uncertainty at the lower, upper, and south arm stations for all years from 2010–14, with the exception of 2010 along the south arm and 2013 at the upper station.

2.4.3 Kaskawulsh and Naluday, 2018

The modelled surface melt for the period 27 July–15 September 2018 is shown for both Kaskawulsh and Nālūdäy Glaciers in Figure 2.5 and is compared to measurements in Figure 2.4. Unfortunately, due to various failures in the collection of the *in-situ* ablation measurements we do not have a continuous surface ablation record on Kaskawulsh in 2018. On Nālūdäy, only the lower station has a continuous melt record, which we have used to approximate measured melt at the middle station.

Modelled melt rates on Kaskawulsh in 2018 fall within the range of melt rates from 2012–14. Modelled melt rates averaged over the period 27 July–15 September 2018 were

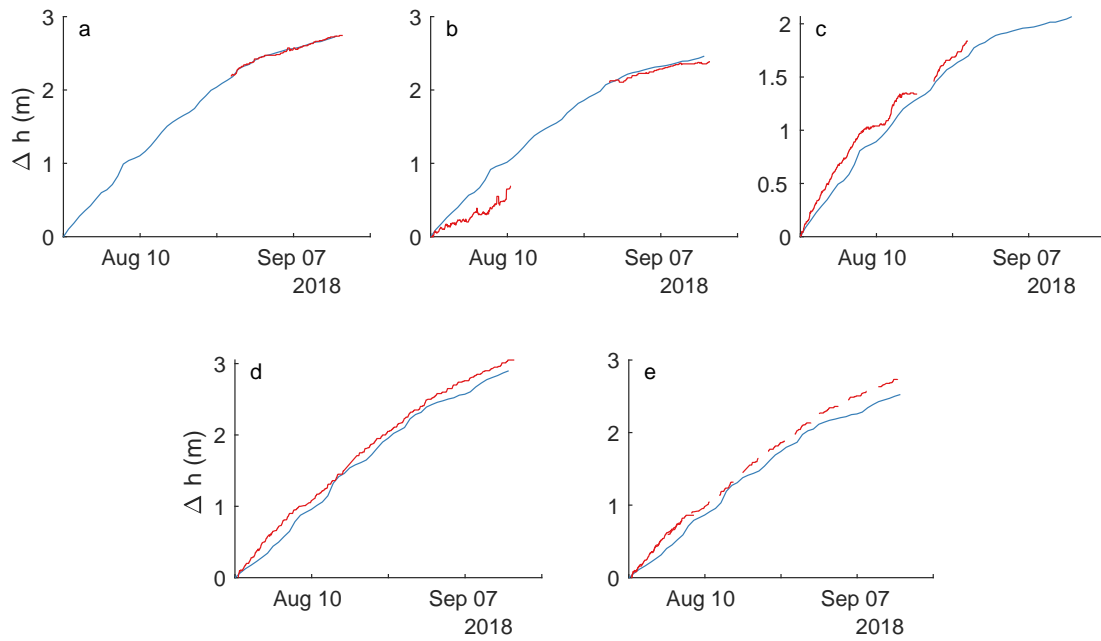


Figure 2.4: Modelled (blue) surface ablation (m) compared to timelapse camera ablation stake measurements (red) from 27 July to 15 September 2018 at the (a) Kaskawulsh lower station, (b) Kaskawulsh middle station, (c) Kaskawulsh upper station. (d) Nàlùdäy lower station, (e) Nàlùdäy middle station. The dashed line in (e) shows the extended melt record for Nàlùdäy Glacier computed from melt observations at the lower station.

Table 2.2: Modelled melt with estimated uncertainties (m w.e.). Uncertainties are computed from estimated uncertainty in surface albedo, 12 meter depth ice temperature, and incoming LW radiation (2010–14 only) using eq. (2.27)

Glacier	Melt year	Modelled period	Lower	Middle	Upper	South Arm	Mean
Kaskawulsh	2010	23 June – 29 August (29 days)	3.49 ± 0.53	3.39 ± 0.52	2.95 ± 0.52	3.19 ± 0.50	2.93 ± 0.52
	2011	13 August – 15 September (33 days)	0.81 ± 0.22	0.73 ± 0.21	0.57 ± 0.21	0.64 ± 0.21	0.59 ± 0.21
	2012	23 June – 15 Septem- ber (85 days)	3.56 ± 0.62	3.42 ± 0.61	2.92 ± 0.61	3.18 ± 0.59	2.92 ± 0.60
	2013	23 June – 15 Septem- ber (85 days)	4.12 ± 0.63	3.94 ± 0.63	3.42 ± 0.62	3.71 ± 0.60	3.42 ± 0.62
	2014	23 June – 15 Septem- ber (85 days)	3.78 ± 0.63	3.64 ± 0.63	3.13 ± 0.62	3.39 ± 0.60	3.12 ± 0.62
	2018	27 July – 15 Septem- ber (51 days)	2.33 ± 0.18	2.09 ± 0.17	1.76 ± 0.16	1.96 ± 0.15	1.81 ± 0.16
Nàludäy	2018	27 July – 15 Septem- ber (51 days)	2.47 ± 0.15	2.15 ± 0.14	1.72 ± 0.15		1.64 ± 0.14

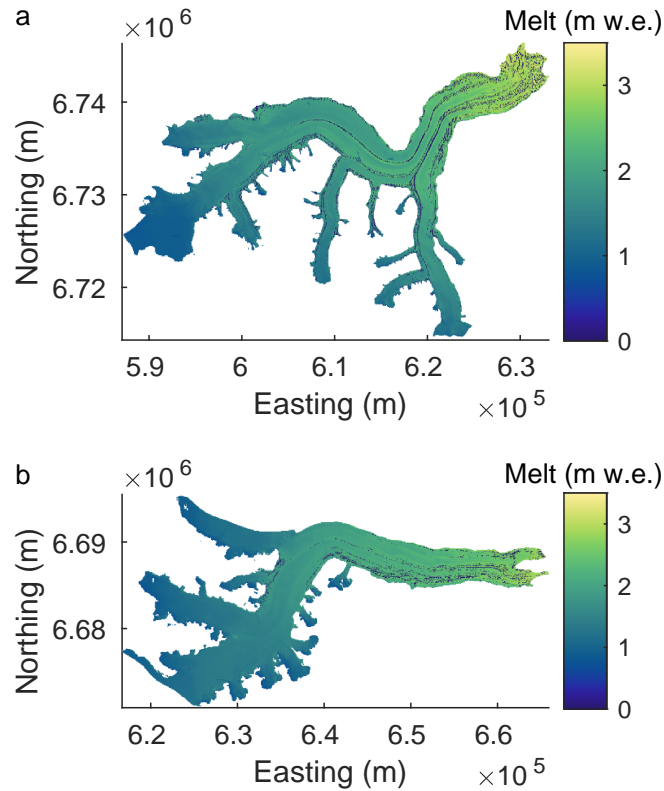


Figure 2.5: Modelled surface melt from 27 July to 15 September 2018 on (a) Kaskawulsh Glacier and (b) Nàlùdäy Glacier. Interior dark regions with no surface melt are those that we have classified as insulated by debris cover.

0.046 m w.e. day⁻¹ at the lower station, 0.041 m w.e. day⁻¹ at the middle station, 0.035 m w.e. day⁻¹ at the upper station, and 0.038 m w.e. day⁻¹ at the south arm station. Modelled melt rates on Nàlùdäy were 0.048 m w.e. day⁻¹ at the lower station, 0.042 m w.e. day⁻¹ at the middle station, and 0.034 m w.e. day⁻¹ at the upper station.

The model results are quantitatively compared to time-lapse ablation stake measurements in Table A.4. ME is less than 0.25 m (<9%) and the ARE is less than 0.005 m w.e. day⁻¹ (<10%) at all locations on both glaciers. Modelled ablation agrees with timelapse camera ablation stake measurements within our uncertainty estimates at all locations except at the middle station on Nàlùdäy, where we have had to use melt at the lower station as a proxy to estimate melt at the higher elevation middle station, making it difficult to make

conclusions about model error at this location.

2.4.4 Shading by adjacent topography

We expect the relative importance of shading of the glacier surface to be highly sensitive to glacier geometry, aspect, and the surrounding topography. We quantify the impact of shading on Kaskawulsh and Nàhùdäy Glaciers in 2018 by calculating the difference in modelled melt at the end of the modelled period (27 July–15 September 2018) with and without including surface shading in the model. Averaged over the entire surface of each glacier, the effect of shading is very small (a total difference of -0.028 m w.e. or -1.6% , and -0.020 m w.e. or -1.2% , for Kaskawulsh and Nàhùdäy, respectively; Figure 2.6). Due to aspect and neighbouring topography, the impact is generally greater on Kaskawulsh.

Along the main trunk of Kaskawulsh the change in modelled surface melt over the period 27 July–15 September 2018 due to shading ranges from 0 to -0.05 m w.e. The impact at the lower, middle, and upper stations is -0.02 m w.e., -0.001 m w.e., and -0.003 m w.e., respectively. This small change is due to the stations being located near the center of the glacier where the glacier has a predominantly easterly aspect. In comparison, we find large differences in modelled melt along the south arm. The combination of a northerly aspect and a narrower valley leads to differences in melt up to -0.35 m w.e. ($\sim 20\%$) along the western margin. However, the difference at the south arm HOB0 location was only -0.04 m w.e. (2.0%) since it is located near the center of the glacier, to the east of the shading footprint.

In comparison, shading of the glacier surface is relatively less important on Nàhùdäy Glacier. The difference is negligible across lower elevations, with a maximum of ~ 0.025 m w.e. where the glacier has a more northerly aspect. There is a large difference (~ 0.25 m w.e., or $\sim 15\%$) on one of the tributaries, but the difference is more spatially localized than on Kaskawulsh. On Nàhùdäy, the difference at the lower, middle, and upper stations is -0.002 m w.e., -0.001 m w.e., and -0.02 m w.e., respectively. The upper station has a larger difference since it is located where the glacier has a northeasterly aspect, allowing the surface to be shaded late in the afternoon, whereas the small (< 1 cm w.e.) difference at the lower and middle stations is typical of the main trunk of Nàhùdäy.

2.4.5 Subsurface model

We also compare model outputs with and without including the subsurface model to quantify its importance, using a subsurface ice temperature of -3°C . We use the 2012 melt

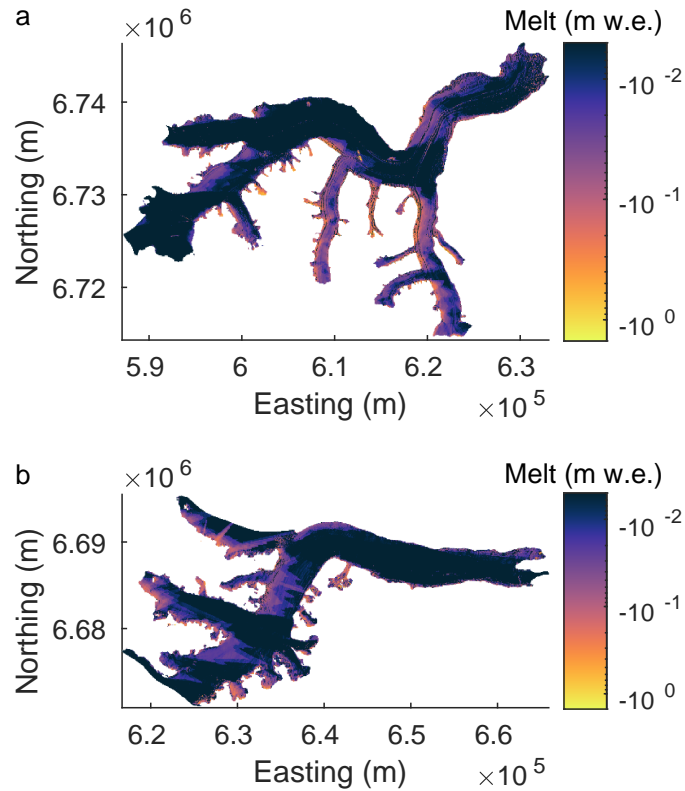


Figure 2.6: Effect of shading the glacier surface for the period 27 July to 15 September 2018. Difference in modelled surface melt (m w.e.) with and without surface shading on (a) Kaskawulsh Glacier and (b) Nàtùdäy Glacier. Negative values indicate a reduction in surface melt due to shading of the glacier surface. Note the logarithmic colour scales.

season (23 June–15 September) at Kaskawulsh as a case study because (1) we have complete temporal coverage to run and validate the model, (2) modelled melt compares well to measured melt, and (3) air temperatures were abnormally cold in early July 2012, leading to significant warming heat fluxes. When we exclude the subsurface heat conduction model, we assume the surface layer of ice is a constant 0°C .

Throughout the 2012 melt season, the subsurface model reduces modelled melt on Kaskawulsh Glacier by ~ 0.1 to 0.35 m w.e. compared to the SEB model without the subsurface model, with the difference increasing rapidly with elevation (Figure 2.7). At the lower, middle, upper, and south arm stations the model difference is -0.14 m w.e. (-4.0%),

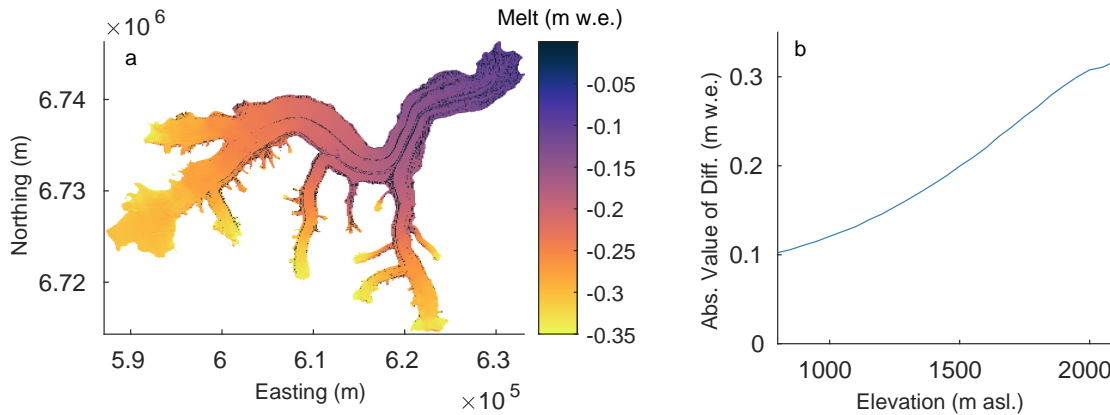


Figure 2.7: Impact of subsurface model for heat conduction throughout the 2012 melt season (23 June–15 September) on Kaskawulsh Glacier. (a) Difference in modelled melt (m w.e.) between SEB model with subsurface model and SEB model without subsurface model. Negative values indicate that the subsurface model reduced surface melt. (b) Absolute value of difference as a function of elevation.

-0.21 m w.e. (-6.1%), -0.26 m w.e. (-8.6%), and -0.20 m w.e. (-6.2%), respectively. There is relatively little variation with surface aspect, slope, or albedo (Figure 2.7). Instead, the spatial variation in melt differences is driven by the lower air temperatures at higher elevations. Colder temperatures allow the surface to cool further below the melting point overnight, resulting in larger warming heat fluxes the following morning, and therefore reduced melt totals. In 2014, which was a warmer year, we found the difference to be only -0.19 m w.e. (-6.3%) at the upper station.

We also investigated the surface temperatures and warming heat flux throughout the beginning of the 2012 melt season (23 June–23 July). From 30 June–19 July cold overnight low temperatures at the upper station allowed the surface to cool to as low as -1 °C (Figure A.2). As the surface energy balance became positive the following day, significant heat, up to ~ 150 W m $^{-2}$, was used to warm the ice rather than melt the surface (Figure A.2). Over this one month time period, the models diverged by almost 0.1 m w.e. at the upper station.

The impact of the subsurface model on melt volumes persisted when removing the deep thermal gradient by imposing a subsurface ice temperature of 0 °C. In this case, the difference in modelled melt volumes on Kaskawulsh from 23 June – 15 September 2012 ranged from -0.04 to 0.32 m w.e. At the upper station, melt was reduced by 0.20 m w.e.,

while melt was reduced by 0.15 m w.e. at the lower station.

2.5 Discussion

2.5.1 Model performance

Our model generally shows very good agreement with surface ablation measurements. Total model error is generally less than 9% at the end of the melt season, and in years with high quality in-situ measurements is often within $\sim 5\%$. These errors are reduced significantly compared to the 6–29% errors reported in previous studies in the region [e.g. 147; 92] as discussed further below.

The primary exceptions to the good agreement are the 2013 melt season and the south arm station on Kaskawulsh Glacier. In these cases, the model diverges from the measurements near the end of the melt season, possibly due to late summer snowfall events, particularly at the higher elevation stations, or near- and below-freezing air temperatures altering atmospheric stability near the melting glacier surface affecting the turbulent heat fluxes, as the parameterizations we have used assume a stably stratified layer at the glacier surface [47].

Model performance is similar on both Kaskawulsh and Nàlùdäy Glaciers. However, the model parameters leading to the highest accuracy did not directly transfer between the glaciers. In tuning the model we found that a momentum roughness length of 3 mm provided the best results on Kaskawulsh Glacier, while a momentum roughness length of 5 mm provided the best results on Nàlùdäy Glacier. This finding is in line with MacDougall and Flowers [92], who found their energy balance model transferred well temporally but not between glaciers. Our approach to tuning the model using the surface roughness parameter is common in SEB models [e.g. 44; 14]. However, MacDougall and Flowers [92] did not tune their energy balance model using the surface roughness, instead using directly measured values to more accurately assess the spatial transferability of the model. The surface roughness values we derived by tuning our model are similar to values found in previous studies when using the roughness length as a tuning parameter (for example 5 mm by 14), and to values found by direct measurement on glaciers in the Canadian Rockies (0.7 to 4.5 mm; 48). In our case, the roughness length may be a reflection of the glacier’s dynamic behaviour. The surface of Nàlùdäy Glacier is expected to be more heavily crevassed and fractured following its surge phase, potentially leading to a higher surface roughness [63; 142]. Alternatively, the differing roughness lengths may be a result

of a different bias between the wind speed as measured by the AWSs and the wind speed near the glacier surfaces on each glacier.

Our model performs less robustly on the south arm of Kaskawulsh than along the main trunk. The south arm is a northerly flowing tributary confined in a much narrower valley than the generally easterly/northeasterly flowing main trunk (Figure 2.1). We found the surface of the south arm to be heavily shaded by neighbouring terrain, reducing seasonal melt totals by up to $\sim 10\%$ (Figure 2.6). Combined with the northerly aspect, the south arm experiences significantly less incident shortwave radiation than the main trunk. Reduced shortwave radiation inhibits the growth of a weathering crust and consequently reduces the aerodynamic roughness length [136], leading to reduced turbulent heat fluxes. Since we have used a spatially uniform roughness length, we may be overestimating turbulent heat fluxes at the south arm station on Kaskawulsh Glacier.

Two distributed energy balance studies have been carried out recently in the St. Elias Mountains, both in the Donjek Range located just north of Kaskawulsh Glacier. Wheler and Flowers [147] modelled 1.80 m w.e. of melt at 2280 m asl. from 1 May–13 September 2008 on a small south-facing glacier located 2 km north of Kaskawulsh Glacier, while we modelled ~ 1 m w.e. of melt at ~ 2000 m asl. (Figure 2.8) on a glacier with an easterly aspect, where we would expect lower melt rates. MacDougall and Flowers [92] modelled ~ 1.2 m w.e. of melt at ~ 2300 m asl. on the north-facing North Glacier. Considering the variations in elevation, aspect, and temporal extent, our modelled melt rates are comparable to these previous studies. Wheler and Flowers [147] report relative model errors ranging from 6–29%, while MacDougall and Flowers [92] report errors ranging from 10–18% on two glaciers in the Donjek Range. Compared to these studies, our errors ranging from 5–10% represent a significant improvement in model performance.

We found that the subsurface model (Eq. 2.25) is important for accurately modelling melt volumes. At the upper Kaskawulsh station in 2012, melt was reduced by 0.25 m w.e. (8.6%). Near the ELA, melt was reduced by up to 0.37 m w.e. (13%). These differences in melt agree well with the results of Wheler and Flowers [147] and Pellicciotti et al. [113] who found melt rates were reduced by $\sim 10\%$ in the upper ablation zone, and so we conclude that our implementation of the subsurface model as a system of coupled differential equations is functionally similar to the iterative approach used in these previous studies, but is a more consistent formulation as we allow surface temperature and energy balance to evolve simultaneously. Moreover, we found that the subsurface model significantly reduced melt volumes even for a subsurface temperature of 0°C , indicating the reduction in melt is due to the cooling of near-surface layers overnight more than the deep thermal gradient. The subsurface model will be even more important for yearly mass balance models where the persistence of a winter cold wave into the spring may drastically slow the onset of extensive

melt, and for cold polar glaciers where subsurface heat flux due to the deep thermal gradient will be non-negligible even during the peak of summer.

We found that shading of the glacier surface reduced glacier-wide melt rates by $<2\%$, but locally by more than 20%. This is likely a strong enough impact to locally alter the spatial distribution of surface meltwater, and therefore has implications for ice dynamics in terms of volumes and locations of meltwater accessing the subglacial system. Surface shading may also help to explain spatial variations in surface elevation, as we found high elevations in our DEM along the western margin of the Kaskawulsh south arm, coincident with where our model predicts lower ablation rates due to shading. Moreover, we may be underestimating the impact of cast shadows on melt volumes due to the resolution of our DEM (32 m). Olson et al. [111] showed that using a 32 m resolution DEM leads to an average SW radiation that is 7–20% greater when compared to an 8 m resolution DEM, since coarser resolutions act to smooth out sharp elevation changes. Thus, shading becomes especially important in high resolution melt modelling [e.g. 14].

Insulation by debris also has a small global impact on melt rates on our study glaciers ($\sim 7\%$) but in localized regions the difference may be enough to impact the distribution of meltwater across the surface. Moreover, the global difference is likely to be much larger on more heavily debris covered glaciers, for example in High Mountain Asia where $\sim 11\%$ of total glacier area is debris covered, and nearly 100% in some lower ablation areas [84], or following rock avalanches [e.g. 129].

The final major modification we made in our energy balance model is deriving high resolution albedo (30 m resolution) from Landsat 8 surface reflectance data [100]. The resulting albedo maps have a similar range and standard deviation to nearly coincident in-situ measurements. Moreover, our model has similar performance across a range of elevation on both Kaskawulsh and Nàhùdäy Glaciers, suggesting we have captured the spatial variation in albedo. Therefore, we believe the Landsat 8 surface reflectance appears to be a highly portable and sufficiently accurate proxy for surface albedo that can be used in SEB models.

2.5.2 Model limitations and uncertainties

We have reported large uncertainties in modelled melt and ablation from 2010–14 (up to 20%) as a consequence of uncertainty in the surface albedo and incoming longwave radiation, highlighting the importance of measuring these quantities accurately. The uncertainty in surface albedo could be reduced by directly measuring surface albedo on each of the glaciers in the study area and calibrating the albedo maps to these measurements.

The in-situ measurements of Williamson et al. [149] provide evidence that our albedo maps are reliable enough to be used without calibration, but more thorough comparison and calibration using in-situ data could reduce the uncertainty in melt from SW radiation when a tighter uncertainty bound is required. The uncertainty in incoming longwave radiation can be eliminated by installing weather stations that measure longwave radiation (e.g. AWSK2 and AWSN1).

The UDS data in Figure 2.4 illustrate some of the limitations of the depth sounder data. Throughout 2010, 2011, and most of 2014, the data are high quality with low noise levels. However, throughout 2012 and 2013, and particularly at the upper station, the data has significant noise levels; consecutive measurements at 30 minute intervals vary by as much as 30 cm. We believe this behaviour is due to instrument error, perhaps due to reflections from off-nadir locations as the station melts out unevenly, which makes it difficult to quantify model performance. While model error is large in 2013 (-0.68 m or -14% at the upper station), it is not clear how to partition the bias between suspected instrument error and model error.

2.5.3 Implications for understanding surge mechanisms

Total modelled melt is similar at Kaskawulsh and Nàhùdäy in 2018. We modelled higher melt rates at coincident elevations on Kaskawulsh compared to Nàhùdäy, particularly in the lowest 10 km of the glaciers, but these higher melt rates were largely offset by the higher elevation range of Kaskawulsh (Figure 2.8). The higher melt rates we found on Kaskawulsh at coincident elevations are in part a result of a lower surface albedo on Kaskawulsh compared to Nàhùdäy leading to increased absorption of shortwave radiation. Lower surface albedo on Kaskawulsh may be a result of the glacier geometry; Kaskawulsh Glacier has several major confluences (Figure 2.1), each providing an opportunity for debris to access the middle of the glacier. Furthermore, since Nàhùdäy is a surge-type glacier, its surface is upheaved and fractured following each surge, exposing regions of subsurface clean ice and leaving the surface relatively clean. In contrast, debris on Kaskawulsh slowly melts out and accumulates on the surface, leading to lower albedo even away from medial moraines and confluences.

We can examine whether volumes of surface water input could impact surge dynamics by considering the enthalpy balance suggested by Benn et al. [17]. We have shown similar melt volumes on Kaskawulsh and Nàhùdäy, suggesting that differences in enthalpy between these two glaciers must be in the subsurface environment rather than driven by volumes of surface water input. The surface slope is very similar between the two glaciers (Figure 2.8),

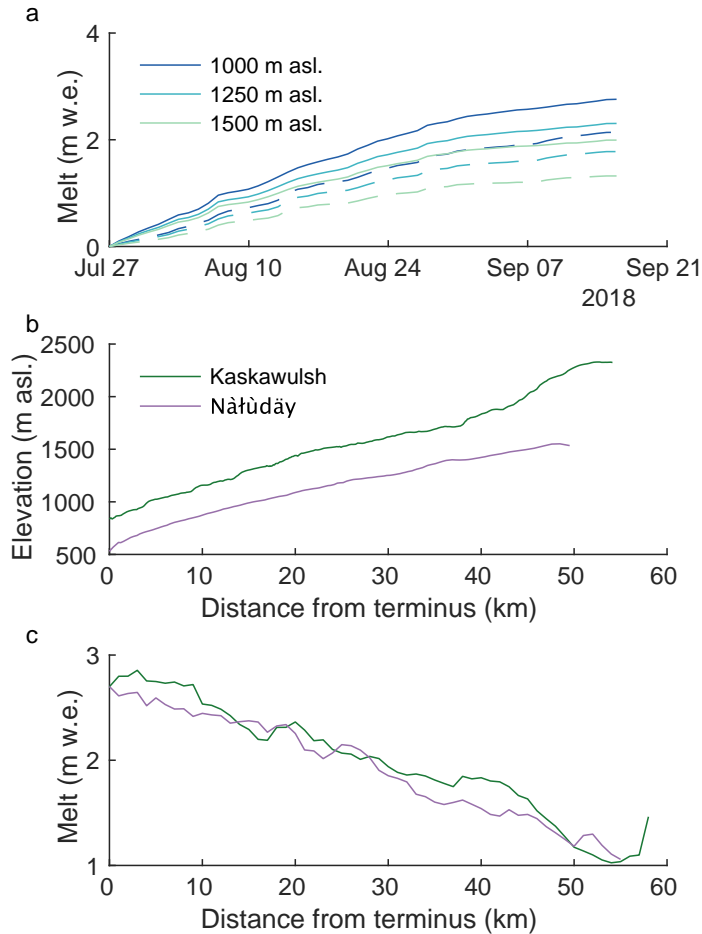


Figure 2.8: Modelled melt rates and elevation profiles on Kaskawulsh and Nàhùdäy Glaciers for the period 27 July–15 September 2018. (a) Average melt (m w.e.) at 1000 m, 1250 m, and 1500 m on Kaskawulsh (solid) and Nàhùdäy (dashed) Glaciers. (b) Centerline elevation (m asl.) on Kaskawulsh and Nàhùdäy. (c) Average melt (m w.e.) on Kaskawulsh and Nàhùdäy.

and combined with similar melt rates, we expect a similar rate of surface steepening due to surface melt, and a similar resulting change in driving stress. The surface slope should increase in the upper regions of Nàhùdäy Glacier leading up to a surge, but at present this does not seem to be impacting the lower portions of this glacier. To fully determine the

control of meltwater on dynamics, a supraglacial routing model and subglacial hydrology model [e.g. 145] will be necessary, and with our SEB model we have excellent inputs to drive such models.

2.6 Conclusions

We have presented a SEB model that captures the melt measured at Nàhùdäy and Kaskawulsh Glaciers, both spatially and temporally, to within 9% (range: -8.4% to 7.1%), a significant improvement in performance compared to other SEB models that have been applied in this region. In addition to improved performance, we have demonstrated the importance of spatially varying albedo, shading by adjacent topography (reducing melt by more than 20% in localized regions), insulation by thick debris (reducing total melt volumes by $\sim 7\%$ averaged across our study area), and subsurface heat flux (improving agreement between modelled and measured melt by up to 8.6% at the upper Kaskawulsh station) in both the volume and distribution of melt on both glaciers. Together, the improvements we have made to existing SEB models significantly advance the spatial representation of surface melt. The improved model is an important tool in understanding meltwater inputs to glacier systems, and how meltwater influences ice dynamics in the St. Elias Mountains.

Seasonal melt volumes are similar between the two glaciers, with higher melt towards the terminus of Kaskawulsh Glacier due to lower albedo and slightly higher turbulent heat fluxes offset by a higher elevation range compared to Nàhùdäy Glacier. The relatively higher albedo on Nàhùdäy may be due to its surge-driven dynamics that cause extreme fracturing and upheaval every 12–15 years, exposing cleaner subsurface ice. Similarly, we find that regions of debris insulated ice are more elevated on Kaskawulsh Glacier compared to Nàhùdäy, again likely due to the surface topography reorganization when Nàhùdäy surges.

The model we have presented requires extensive input data. Combined with the relative complexity of the model, it is best-suited to catchment-scale applications where high quality in-situ data is already available to better understand the volume and spatial and temporal distribution of meltwater production throughout the melt season. Since we derive distributed surface albedo from Landsat 8 data, the model also has wide applicability to further investigate the impacts of the darkening of mountain glaciers [101; 41] and ice sheets [20; 19; 42; 148; 139].

We found some of the model components to have less of an impact on total melt volumes than others. In particular, surface shading made little difference to seasonal melt volumes on both Kaskawulsh and Nàhùdäy. However, this finding is primarily a result of

the geometry of these particular glaciers. They generally flow to the east and fill relatively wide valleys. We showed that shading was relatively more important along the South Arm of Kaskawulsh, indicating this is an important mechanism for narrower, northerly aspect glaciers. Therefore, it is important to quantify the impact of each of the model components (shading, subsurface model, and insulation by debris) before deciding whether to include or exclude them.

Future work to combine our SEB model with a surface routing algorithm and subglacial hydrology model would further constrain the controls on surging in the region and provide evidence to explain the contrasting dynamics of Kaskawulsh and Nàlùdäy.

Chapter 3

Finite volume methods on unstructured triangular mesh elements and edges

3.1 Introduction

Finite volume methods are a broad class of methods to solve partial differential equations. These methods are based on applying a conservation law to a specified region to calculate the rate of change in the average of a conserved quantity as the difference between the flux out of and into the region [89]. They are useful for physical problems because these methods are exactly conservative and readily parallelizable [89; 1]. Since they are formulated in terms of fluxes across boundaries, they are adaptable to unstructured meshes, including meshes with mixed types of elements. For these reasons, finite volume methods are a common choice for computational fluid dynamics (CFD) solvers, including the MIT general circulation model [93], and for a variety of applications including modelling cardiovascular systems [86]. The main drawback of these methods is that computing gradients on an unstructured mesh is not as straightforward as on a structured grid. It can also be difficult to generate high quality meshes for complex geometries, especially in three dimensions [72].

This chapter describes the finite volume numerical methods used in the Subaerial Drainage System model (Chapter 4) by considering a semi-discrete finite volume form of a scalar conservation law applied to two-dimensional unstructured triangular meshes with an unspecified flux function. We then compare several methods for calculating gradients on the elements of the unstructured mesh. This process, called gradient reconstruction, is necessary when the flux function explicitly depends on the gradient of the conserved quantity. This is the case for diffusion equations, for instance the heat equation. Finally,

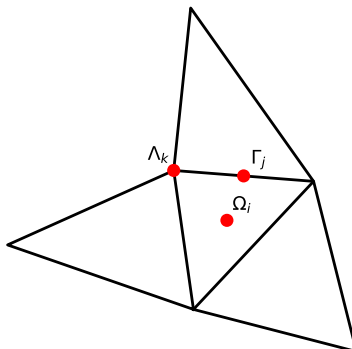


Figure 3.1: Mesh topology and nomenclature for a small subset of an unstructured triangular mesh. Ω_i refers to element i , located at the element centroid. Γ_j refers to edge j , located at the edge midpoint. Λ_k is the k -th node. Edge Γ_j connects exactly two elements and two nodes, while element Γ_j is connected to exactly three edges.

we explore how to apply one-dimensional finite volume methods on the edges of the triangular elements. This approach is well-suited to modelling the flow of water along edges, imagining the edges as representing possible rivers, for example. Here, we compare several methods for calculating the along-edge directional derivatives of the conserved quantity.

3.2 Unstructured mesh topology

We follow the nomenclature of Werder et al. [145] to describe our unstructured triangular mesh. Elements are denoted by Ω , edges by Γ , and nodes by Λ . We index elements by i , edges by j , and nodes by k (Figure 3.1). When variables are evaluated on an element Ω_i , we consider this value to be defined at the element centroid. Similarly, values on edges are assumed to be located at the edge midpoint, as shown in Figure 3.1.

We use the absolute value symbol to denote the measure of a mesh object. That means $|\Omega_i|$ is the area of element Ω_i and $|\Gamma_j|$ is the length of edge Γ_j . The outward unit vector to edge Γ_j (with respect to element Ω_i) is denoted \mathbf{n}_j . In the following development it is implicitly assumed that each element is connected to exactly 3 edges (Figure 3.1), while each node connects at least 3 edges, but typically many more.

3.3 General form

First, we derive a general semi-discrete form of the conservation law for a triangular mesh. This derivation is standard [e.g. 89], but is repeated here to emphasize how it applies to triangular meshes.

Consider the general two-dimensional scalar conservation law

$$\frac{\partial u}{\partial t} + \nabla \cdot \mathbf{q}(u, \nabla u) = f(t, u), \quad (3.1)$$

where $\mathbf{q}(u, \nabla u)$ is the flux, which is a function of the conserved quantity u and its gradient ∇u , and $f(t, u)$ is a source term. Note that this form differs from the standard form used by LeVeque [89] since we explicitly assume the flux depends on the gradient of the conserved quantity. Integrating over an arbitrary element Ω_i with infinitesimal area element dA , we have

$$\iint_{\Omega_i} \frac{\partial u}{\partial t} dA + \iint_{\Omega_i} \nabla \cdot \mathbf{q}(u, \nabla u) dA = \iint_{\Omega_i} f(t, u) dA.$$

We can move the time derivative outside the first integral, and apply the divergence theorem to the second term. Then, the conservation law becomes

$$\frac{d}{dt} \iint_{\Omega_i} u dA + \int_{\partial\Omega_i} \mathbf{q}(u, \nabla u) dS = \iint_{\Omega_i} f(t, u) dA.$$

To construct the finite volume method, we let \bar{u} be the average of u on Ω_i , let $F(t, u)$ be the average of f on Ω_i , and divide through by the area $|\Omega_i|$. We recognize that the contour integral becomes a discrete sum over the three triangle edges, so that we have

$$\frac{d\bar{u}}{dt} + \frac{1}{|\Omega_i|} \sum_{j=1}^3 \mathbf{q}(u, \nabla u)|_{\Gamma_j} |\Gamma_j| = F(t, u). \quad (3.2)$$

This is the most general finite volume formulation of conservation law (equation (3.1)). It is general in that the method of computing the edge fluxes $\mathbf{q}|_{\Gamma_j}$ is unspecified.

The edge fluxes are computed using an upwind method. If Ω_1 and Ω_2 are the two neighbouring elements with outward unit normals \mathbf{n}_1 and \mathbf{n}_2 , then the upwind element is the element where $\mathbf{q}|_{\Omega_i} \cdot \mathbf{n}_i > 0$, for $i = 1, 2$. We can write the edge flux as

$$\mathbf{q}_j = \begin{cases} \mathbf{q}_1 & \text{if } \mathbf{q}|_{\Omega_1} \cdot \mathbf{n}_1 \geq 0 \text{ and } \mathbf{q}|_{\Omega_2} \cdot \mathbf{n}_2 \leq 0, \\ \mathbf{q}_2 & \text{if } \mathbf{q}|_{\Omega_1} \cdot \mathbf{n}_1 \leq 0 \text{ and } \mathbf{q}|_{\Omega_2} \cdot \mathbf{n}_2 \geq 0, \\ 0 & \text{otherwise .} \end{cases} \quad (3.3)$$

The complete first-order semi-discrete finite volume form of equation (3.1) is given by equations (3.2) and (3.3).

3.4 Gradient reconstruction on unstructured elements

The general form (equation (3.2)) is incomplete, as we have not specified how to compute the gradient ∇u . The problem of computing gradients in finite volume methods is called gradient reconstruction. Several methods exist, which may be classified into two categories. Methods may be based on applying the divergence (also called Green-Gauss) theorem, analogous to the derivation of the semi-discrete form. These are called Green-Gauss methods. Methods may also be based on developing a linear system of equations using all neighbouring values, called least squares methods [133]. These methods are described in detail in the following sections.

3.4.1 Green-Gauss methods

Green-Gauss methods are based on applying the divergence (Green-Gauss) theorem [133]. In the same way as we derived the semi-discrete form (equation (3.2)), we integrate ∇u over a control area Ω_i , and apply a modified form of the divergence for scalar quantities,

$$\iint_{\Omega_i} \nabla u dA = \int_{\partial\Omega_i} u \mathbf{n} dS,$$

where \mathbf{n} is the outward unit normal. Recognizing again that the contour integral becomes a sum over the triangle edges, we have

$$\iint_{\Omega_i} \nabla u dA = \sum_{j=1}^3 u|_{\Gamma_j} \mathbf{n}_j |\Gamma_j|.$$

Finally, we let $u_j = u|_{\Gamma_j}$ and let $\overline{\nabla u}$ represent the average of ∇u on the element, leaving

$$\overline{\nabla u} = \frac{1}{|\Omega_i|} \sum_{j=1}^3 u_j \mathbf{n}_j |\Gamma_j|. \quad (3.4)$$

This expression is the basis of the Green-Gauss methods, which differ in their calculation of the edge values u_j .

Arithmetic averaging

The simplest approach to compute edge values in equation (3.4) is to simply average the neighbouring element values. Explicitly,

$$u_j = \frac{u|_{\Omega_1} + u|_{\Omega_2}}{2},$$

where Ω_1 and Ω_2 are the neighbouring elements. This method is assigned the label “GG Simple”.

Area-weighted averaging

The next approach modifies the arithmetic averaging method by computing the area-weighted average,

$$u_j = \frac{u|_{\Omega_1}|\Omega_1| + u|_{\Omega_2}|\Omega_2|}{|\Omega_1| + |\Omega_2|}.$$

This method is assigned the label “GG Area”.

Green-Gauss least squares

This method is again based on equation (3.4), but we construct a least squares problem to solve for the edge values u_j . Consider an arbitrary edge Γ_j , and let $i = \{1, \dots, N\}$ be the indices of the elements that share a node with the edge (the stencil; Figure 3.2), and let u_i be the value of u on element Ω_i . Expanding about element Ω_i ,

$$u_j = u_i + \frac{\partial u}{\partial x}\bigg|_{\Omega_i} \Delta x_i + \frac{\partial u}{\partial y}\bigg|_{\Omega_i} \Delta y_i + \mathcal{O}(\Delta x_i^2, \Delta y_i^2).$$

By writing this equation for each element in the stencil we arrive at the overdetermined linear system

$$\begin{bmatrix} 1 & \Delta x_1 & \Delta y_1 \\ 1 & \Delta x_2 & \Delta y_2 \\ \vdots & \vdots & \vdots \\ 1 & \Delta x_N & \Delta y_N \end{bmatrix} \begin{bmatrix} u_i \\ u_{i,x} \\ u_{i,y} \end{bmatrix} = \begin{bmatrix} u_1 \\ u_2 \\ \vdots \\ u_N \end{bmatrix}.$$

To construct the least squares solution, we rewrite this equation as the matrix system $\mathbf{Ax} = \mathbf{b}$. One approach to solve this overdetermined system is using standard least squares,

$$\mathbf{x} = (\mathbf{A}^T \mathbf{A})^{-1} \mathbf{A}^T \mathbf{b}.$$

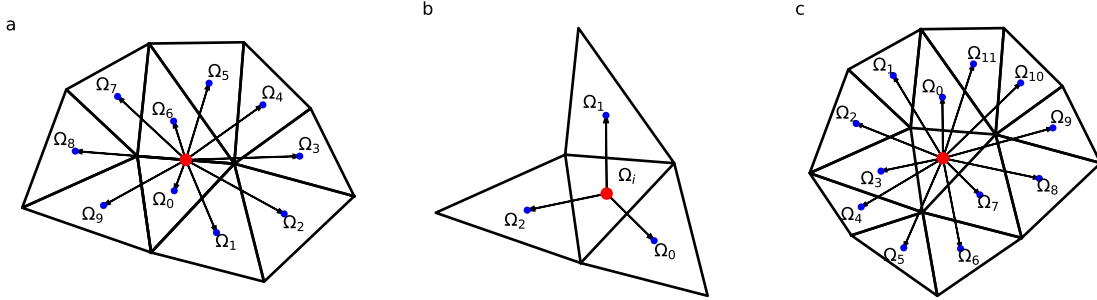


Figure 3.2: Examples of gradient reconstruction stencils for (a) Green-Gauss least squares method, (b) compact least squares method, and (c) extended least squares method.

However, the elements are not uniformly distributed around the edge Γ_j . We expect the centroids of two elements that share the edge to be much closer than the centroids of the remaining elements that only share a node. To account for this distribution we assign weights w_k to each equation, which we encode using a diagonal weight matrix W . We use inverse-distance weighting, $w_i = |\mathbf{r}_i - \mathbf{r}_j|^{-1}$. With this weight matrix, the weighted least squares solution is

$$\mathbf{x} = (A^T W^T W A)^{-1} A^T W^T W \mathbf{b}. \quad (3.5)$$

This method is assigned the label “GG-LS”.

3.4.2 Least squares methods

Least squares methods construct a least squares problem for the gradient on each element. We consider three least squares methods of varying degrees of complexity. The methods take the same approach, but differ in the stencils they use and the order of their Taylor expansion.

First order least squares methods

We consider two first order least squares methods. For both methods, consider an arbitrary element Ω_i . We wish to compute the gradient on this element.

For each element Ω_k in the stencil, we expand about Ω_i to write

$$u_k = u_i + u_{x,i} \Delta x_k + u_{y,i} \Delta y_k + \mathcal{O}(\Delta x_k^2, \Delta y_k^2).$$

By combining the equations for each element in the stencil and neglecting the higher order terms, we arrive at the approximate system of equations

$$\begin{bmatrix} \Delta x_1 & \Delta y_1 \\ \Delta x_2 & \Delta y_2 \\ \vdots & \\ \Delta x_N & \Delta y_N \end{bmatrix} \begin{bmatrix} u_{x,i} \\ u_{y,i} \end{bmatrix} = \begin{bmatrix} u_1 - u_i \\ u_2 - u_i \\ \vdots \\ u_N - u_i \end{bmatrix}.$$

Making the obvious definitions, we write the system as $A\mathbf{x} = \mathbf{b}$. As with the Green-Gauss least squares method we use inverse-distance weighting to construct a weight matrix W . We compute the gradient by solving the system

$$W A \mathbf{x} = W \mathbf{b}.$$

The compact least squares method includes only elements that share an edge with Ω_i in the stencil, while the extended method includes all elements that share a node with Ω_i (Figure 3.2). Inverse-distance weighting is especially important for the extended least squares method, as the three elements that share edges with Ω_i are typically much closer to the element in question, and so we want to assign higher weights to the values in these elements.

We consider four combinations of weighting and stencils and assign labels as follows: (1) inverse-distance weighted least squares with the extended stencil (WLS), (2) unweighted least squares with the extended stencil (LLS), (3) inverse-distance weighted least squares with the compact stencil (WLS-compact), and (4) unweighted least squares with the compact stencil (LLS-compact).

Higher order least squares method

Following the same steps as in the previous section, we can formulate a higher order method. Expanding to include the next highest order terms,

$$u_k = u_i + u_{x,i} \Delta x_k + u_{y,i} \Delta y_k + \frac{1}{2} u_{xx,i} \Delta x_k^2 + u_{xy,i} \Delta x_k \Delta y_k + \frac{1}{2} u_{yy,i} \Delta y_k^2 + \mathcal{O}(\Delta x_k^3, \Delta y_k^3).$$

After neglecting the cubic terms, this expansion yields the matrix system

$$\begin{bmatrix} \Delta x_1 & \Delta y_1 & \frac{1}{2}\Delta x_1^2 & \Delta x_1\Delta y_1 & \frac{1}{2}\Delta y_1^2 \\ \Delta x_2 & \Delta y_2 & \frac{1}{2}\Delta x_2^2 & \Delta x_2\Delta y_2 & \frac{1}{2}\Delta y_2^2 \\ & & \vdots & & \\ \Delta x_N & \Delta y_N & \frac{1}{2}\Delta x_N^2 & \Delta x_N\Delta y_N & \frac{1}{2}\Delta y_N^2 \end{bmatrix} \begin{bmatrix} u_{x,i} \\ u_{y,i} \\ u_{xx,i} \\ u_{xy,i} \\ u_{yy,i} \end{bmatrix} = \begin{bmatrix} u_1 - u_i \\ u_2 - u_i \\ \vdots \\ u_N - u_i \end{bmatrix}, \quad (3.6)$$

where we include all elements in the extended stencil.

This matrix system is solved in the least squares sense with inverse-distance weighting and the extended stencil. The stencil is supplemented with the stencils of neighbouring elements if the stencil has less than five elements (this is sometimes the case near boundaries). This method is assigned the label ‘‘WLS2’’.

3.4.3 Method comparison

To compare the gradient reconstruction methods, we compute their errors on several meshes with decreasing minimum area thresholds. We consider the test function

$$f(x, y) = xy \exp(-4(x^2 + y^2)),$$

which has analytical derivatives

$$\begin{aligned} f_x(x, y) &= (y - 8x^2y) \exp(-4(x^2 + y^2)) \\ f_y(x, y) &= (x - 8xy^2) \exp(-4(x^2 + y^2)). \end{aligned}$$

We quantify the error by computing the root mean square error in the residuals between the analytical and numerically approximated x -component of the gradient. We compare each of the methods described, and additionally include both weighted and unweighted least squares methods. The residuals are shown in Figure 3.3. The computational cost is also compared by measuring the total time required to compute the gradient for all elements in the mesh.

Figure 3.3 clearly shows that the two simple Green-Gauss methods (with arithmetic and area-weighted averaging) are a poor choice. These methods converge as the number of mesh elements increase, but they converge to the incorrect gradient value. In other words, these methods are inconsistent.

Three of the least squares methods cluster together with nearly identical performance and wall time (LLS, WLS-compact, and LLS-compact). The WLS method, using inverse-distance weighting and the extended stencil, is consistently more accurate with similar

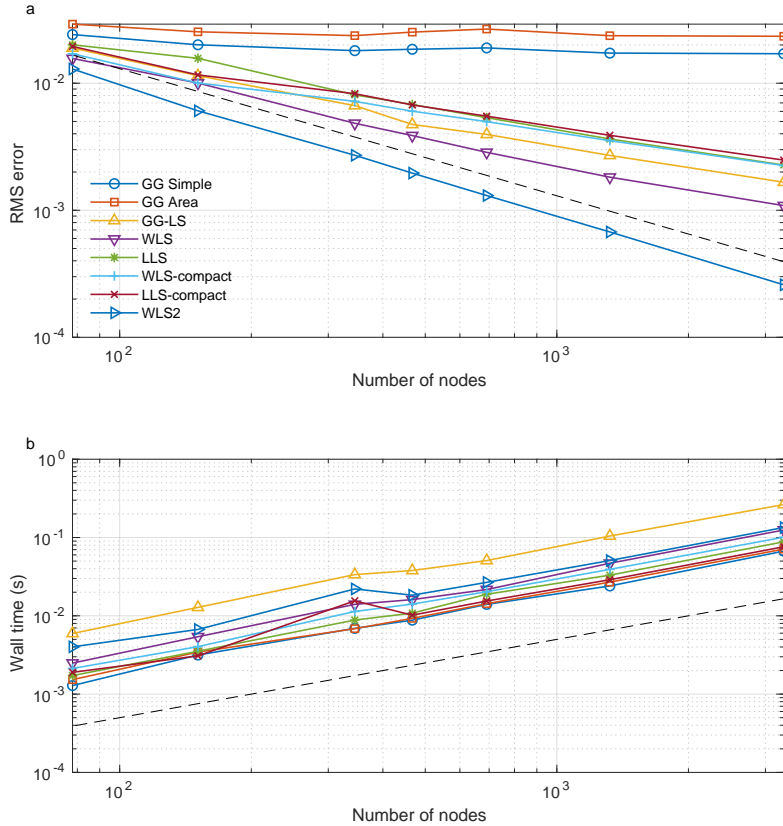


Figure 3.3: Comparison of gradient reconstruction methods on unstructured triangular meshes. (a) RMS error between exact and numerically approximated $f_x(x, y)$. Dashed line shows a linear reference. (b) Total time in seconds to compute the gradient for all mesh elements. Dashed line shows a linear reference.

wall time. The hybrid Green-Gauss least squares method has intermediate performance between the least squares methods, but is the most computationally expensive method. Since these methods all have the same order of convergence and computational cost, any of these methods would be a good choice to implement.

The single higher order method, WLS2, clearly outperforms the other methods. It is more accurate for all meshes, and it converges faster as the mesh is refined. It is also less computationally expensive than the GG-LS method. Therefore, this is the preferred

method.

The methods have benefits and drawbacks beyond their accuracy and cost. The least-squares based methods can avoid an explicit treatment of boundary conditions when the boundary conditions are simple because the stencil only considers interior points.

3.5 Finite volume methods on edge network

It is also possible to imagine a scenario when finite volume methods need to be applied on the edges of the mesh instead of (or in addition to) the elements. For example, this would be the case when the edges represent a network of streams, and we want to compute the flow in each stream. In this case, the relevant conservation law for mass is

$$\frac{\partial u}{\partial t} + \frac{\partial}{\partial s} q \left(u, \frac{\partial u}{\partial s} \right) = g(t, u), \quad (3.7)$$

where $\frac{\partial}{\partial s}$ represents the directional derivative along the edge. The derivation of the semi-discrete finite volume form follows the same steps as in the two-dimensional case, and we arrive at

$$\frac{\partial \bar{u}}{\partial t} + \frac{1}{|\Gamma_j|} (q^+ - q^-) = G(t, u), \quad (3.8)$$

where \bar{u} is the average of u on edge Γ_j , q^+ and q^- are the flux into and out of the element, respectively, and $G(t, u)$ is the average of $g(t, u)$.

3.6 Gradient calculation on edge network

As in the two-dimensional case, the most difficult aspect is computing the streamwise derivative $\frac{\partial u}{\partial s}$ in the flux parameterization. For the one-dimensional equation, we compute the derivative as

$$\frac{\partial u}{\partial s} = \frac{u_2 - u_1}{|\Gamma_j|},$$

where u_1 and u_2 are the values of u on the nodes that Γ_j connects. The methods vary in their calculation of the nodal values.

3.6.1 Arithmetic averaging

For each method, the nodal values u_1 and u_2 are computed from the values of u on all elements connected to the nodes. The simplest possible method takes the arithmetic average of the values of u on the midpoints of the connecting elements,

$$u_k = \frac{1}{N} \sum_{j=1}^N u|_{\Gamma_j},$$

for an arbitrary node Λ_k .

3.6.2 Least squares method

The least squares method takes a similar approach to the Green-Gauss least squares method. Consider an arbitrary node Λ_k , with N connecting edges $\{\Gamma_1, \dots, \Gamma_N\}$. Now, consider an arbitrary connecting element Γ_j , and let $u_j = u|_{\Gamma_j}$. Then by expanding about the midpoint of Γ_j ,

$$u_j = u_k + u_x \Delta x_j + u_y \Delta y_j,$$

where $(\Delta x, \Delta y)$ is the vector from the midpoint of Γ_j to the node Λ_k . By expanding in this way for each of the N connecting edges, we can write the system

$$\begin{bmatrix} 1 & \Delta x_1 & \Delta y_1 \\ 1 & \Delta x_2 & \Delta y_2 \\ \vdots & \vdots & \vdots \\ 1 & \Delta x_N & \Delta y_N \end{bmatrix} \begin{bmatrix} u_k \\ u_x \\ u_y \end{bmatrix} = \begin{bmatrix} u_1 \\ u_2 \\ \vdots \\ u_N \end{bmatrix}.$$

This is essentially the same system as we had for the Green-Gauss least squares method, and so we make the same definitions for A , \mathbf{x} , and \mathbf{b} , and solve the system with inverse-distance weighting.

3.6.3 Interpolation with Matlab

Instead of writing our own least squares interpolation method, we can leverage the existing interpolation functions in Matlab. Specifically, we interpolate between the edge midpoint values to find the nodal values using the `scatteredInterpolant` function. We define two methods, using the “Natural” and “Linear” interpolation methods. These methods are called the “Matlab natural” and “Matlab linear” methods.

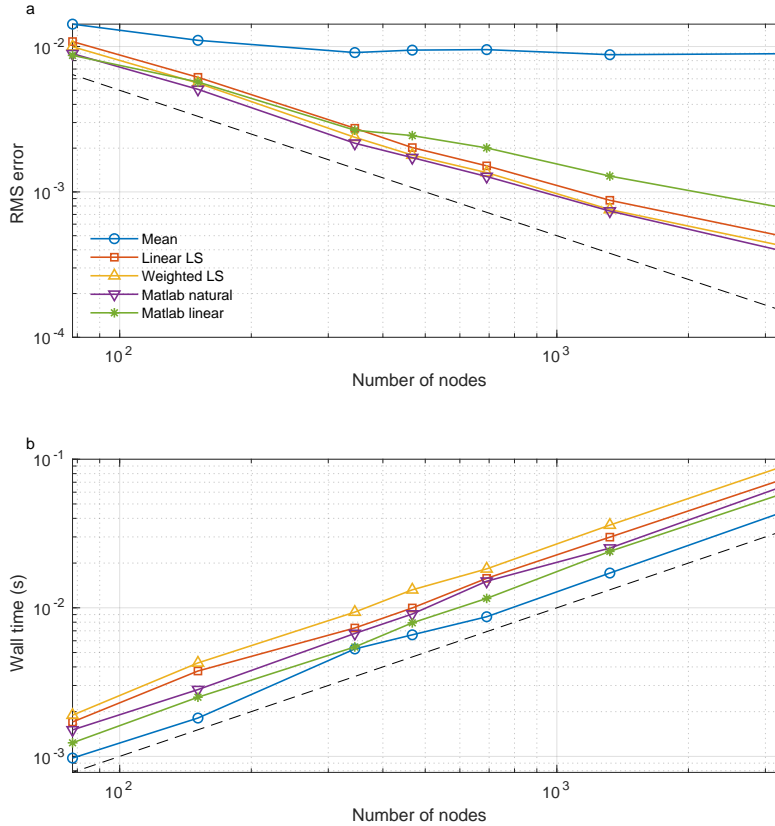


Figure 3.4: Comparison of gradient reconstruction methods on the edge network. (a) Evaluation of the methods by the root mean square (RMS) error in their reconstruction of the along-channel slope $\frac{df}{ds}$. (b) Total computational time in seconds to compute derivatives for the entire mesh.

3.6.4 Method comparison

The same type of comparison of the methods can be done for the gradient reconstruction methods on the edge network, both with and without weights in the least squares solutions. In this case, we compare the RMS error in their approximation of the along-channel derivatives of our function $f(x, y)$. Figure 3.4 shows the RMS error and the total computation time.

Compared to Figure 3.3, we notice in Figure 3.4 that including weights in the least

squares problem does not noticeably improve performance. This is because the variance in edge length in the mesh is small, hence the weights are nearly equal. This will not be the case for meshes than have been nonuniformly refined around regions of particular interest, and so we continue to include weights in the least squares solutions.

We see the same pattern in Figure 3.4 as in Figure 3.3. The simple averaging method converges to the incorrect slope values (this means it is inconsistent). The weighted and unweighted least squares, and the Matlab interpolation routines, have similar performance and wall times, so we recommend the weighted least squares since it is directly applicable to nonuniformly refined meshes.

3.7 Mass conservation on edge network

Recall that in equation (3.8) we simply described q^+ and q^- as the flux into and out of the edge, respectively. To complete the description of the method, we need to specify how we compute these fluxes.

The fluxes are computed based on mass conservation at each node. Since nodes can not store mass, we require

$$\sum_{j=1}^N q_j = 0, \tag{3.9}$$

where $q|_{\Gamma_j}$, and we take the sign convention that $q > 0$ represents flux into the node at $q < 0$ represents flux out of the node.

We enforce mass conservation by summing the flux directed towards the node, and routing all the flux out through a single edge. The criteria to choose the outlet edge is usually based on a potential ϕ (for example, gravitational potential), where mass is routed through the edge with the steepest downhill potential gradient. This process is schematized in Figure 3.5 for an arbitrary geometry. This method ensures mass is conserved at nodes, but also concentrates flow through the path with the lowest potential, analogous to terrestrial streams.

3.8 Conclusions

We have compared several numerical methods for computing gradients on unstructured triangular mesh elements and edges. For elements, the two simplest methods (Green-Gauss with arithmetic (GG simple) or area-weighted (GG Area) averaging) are shown

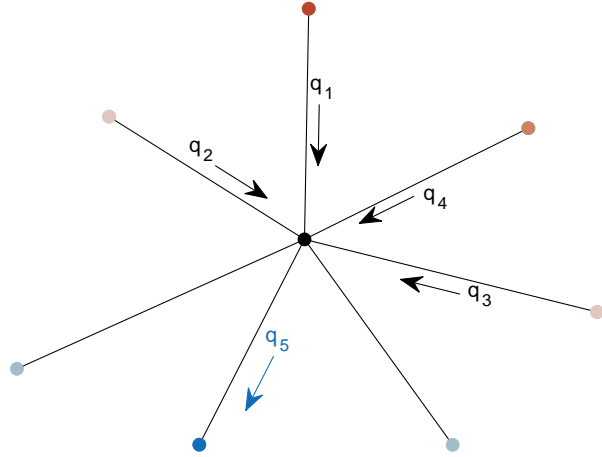


Figure 3.5: Schematic diagram of the mass conservation method at nodes. For this node, four edges have mass flow directed towards the node. The total flow is directed out through the edge with the steepest downhill potential (q_5).

to be inconsistent. As the number of nodes in the mesh increases, the methods do not converge to the correct gradient value. The second order method (WLS2) significantly outperforms all other methods, and is recommended to be used where possible.

For the edge network we found the simple averaging method was also inconsistent. The remaining methods had similar performance, and any of these methods should be a suitable choice. We also described a mass conservation scheme in order to assemble the individual edges into a connected network.

The tests carried out here are useful to inform the development of finite volume methods on unstructured meshes. While these methods have been tested on triangular meshes, they could be easily applied to arbitrary geometries, including with mixed elements. The next chapter explores supraglacial hydrology modelling using the second order element-centred least squares gradient reconstruction method and the first-order inverse-distance weighted node reconstruction method.

Chapter 4

Modeling the dynamics of supraglacial rivers and distributed meltwater flow with the Subaerial Drainage System (SaDS) model

4.1 Introduction

Large volumes of meltwater are generated each summer at the surface of melting glaciers and ice sheets [27; 126]. This meltwater flows across the glacier surface and can access the subglacial environment through moulins. Subglacial water determines basal effective pressure and therefore sliding rates of the overlying ice. As a result, surface meltwater volumes can exert an important control on ice dynamics [e.g. 155; 12; 74].

However, the exact relationship between surface melt rates and glacier flow velocities is complex [138; 131]. While it is clear that the seasonal pattern of glacier velocity is driven by surface meltwater [27], the specific impact that increasing melt rates have on ice velocity is not easily generalized across glacier types and regions [76]. Even for apparently similar glaciers, their response to changes in surface melt rates can be different [27; 98; 76]. In order to determine the impacts of surface melt on the dynamics of different glacial systems, we first need an accurate assessment of the routing of meltwater across the surface and the discharge rate into moulins.

In the ablation zone, meltwater flow consists of slow flow across the bare ice surface along with fast flow through discrete supraglacial channels [52; 115]. Meltwater can often

be stored in supraglacial lakes, features that are particularly common on the Greenland Ice Sheet [27]. Supraglacial flow is more complicated in the accumulation zone, where meltwater can be stored seasonally or perennially in firn aquifers, and percolation and refreezing within firn and snow is important [51; 80; 26; 97].

The supraglacial drainage network is not static throughout the melt season. Supraglacial streams in the ablation zone grow and shrink according to the balance between melt due to frictional heat dissipation along the wetted perimeter, melt due to solar radiation on the banks, and ablation of the adjacent ice surface reducing the channel cross section [134]. This balance means that small streams with low flow rates will melt out throughout the melt season, while larger streams with high flow rates will persist throughout the melt season and often perennially reform in the same location [153; 134]. Under certain conditions, streams can incise deeply enough for the channel opening to pinch closed due to ice deformation, forming an englacial conduit [73]. These seasonal changes in the channel network lead to a temporal pattern in river discharge and moulin inputs that changes throughout the melt season, and therefore have the potential to impact subglacial effective pressure and basal sliding.

A variety of models exist to represent the supraglacial drainage system. The most common approach is to precompute flow paths from a digital elevation model using a flow routing algorithm and travel times using velocity parameterizations [e.g. 4; 8; 33; 34; 130; 153]. However, these models often assume the ice surface and drainage basins are static so that the flow paths do not change throughout the melt season, and usually represent distributed sheet flow only.

Alternatively, “transient” or “dynamic” models can apply conservation laws to mathematically compute supraglacial runoff, usually driven by the conservation of mass of liquid water, combined with flow parameterizations. These models can be formulated for flow in a distributed sheet [49] or for flow in supraglacial channels (also called spillway models) [118; 77]. Since transient/dynamic models are usually formulated as partial differential equations, they are usually more complex and computationally expensive than flow routing. However, their transient formulation allows them to more accurately represent the dynamics of supraglacial flow. These models focus on a single mode of flow, with the exception of Koziol et al. [82], who combined distributed flow routing with supraglacial lake drainage through spillways.

Recent models have started to include both sheet and channel flow. Smith et al. [130] empirically determined synthetic unit hydrographs (SUH) that account for both modes of flow, although the hydrograph is derived using synthetic, non-physically based basis functions. Yang et al. [153] accounted for both types of flow in the Rescaled Width Function

(RWF) model, which also includes a parameterization that increases the interfluvial distance to account for seasonal dynamics. Gleason et al. [58] used the terrestrial Hillslope River Routing model [HRR; 15] that represents distributed hillslope and channelized flow to calculate flow in the Rio Behar catchment. However, this model does not account for seasonal changes in the supraglacial river network. All of these models rely on either in-situ calibration data [130; 58] or a high resolution topological map of the supraglacial river network [153; 58], limiting their transferability to other catchments or glaciers.

Here, we introduce a new supraglacial flow model. The SubAerial Drainage System (SaDS) model is a physically-based, dynamic model that represents coupled flow in both a distributed sheet and through supraglacial channels in order to calculate moulin inputs. SaDS improves on existing models by naturally developing a network of connected lakes and rivers with no prior knowledge of the location of drainage features. The model’s dynamic formulation lets the drainage system evolve throughout the melt season, resulting in moulin inputs with strong seasonal dynamics.

We begin by describing the theoretical basis of the model in section 2. Section 3 describes the setup and results from a synthetic experiment designed to emulate the conditions in the SHMIP experiment [40]. We then examine application of the model to internally drained catchments on the Greenland Ice Sheet in section 4 prior to discussing the outputs from both synthetic and applied experiments in section 5.

4.2 Model description

SaDS largely follows the framework of the subglacial hydrology Glacier Drainage System model (GlaDS) [145]. We combine slow, distributed flow across the glacier surface with discrete flow in supraglacial channels. Both systems are modelled by applying mass conservation with turbulent flow parameterizations, and with mass exchange allowed between the systems. Importantly, we model the dynamic evolution of the supraglacial channel system. Channels grow as concentrated flow melts the underlying ice, and shrink as the ice surface adjacent to the channels melts and lowers. This configuration provides the flexibility required to represent seasonal changes in the partitioning between distributed and channelized runoff. Smaller streams can melt out, with the distributed sheet taking up the excess meltwater and transporting it downstream to larger supraglacial rivers.

We apply the model equations on a two-dimensional, unstructured triangular mesh (Figures 4.2 and B.1), where sheet flow occurs across the elements, and channel flow occurs along the edges of the triangular elements. We first describe the sheet and channel

Table 4.1: Model variables symbols, descriptions, and units

Variable	Description	Units
h_s	Distributed sheet water depth	m
h_c	Channel water depth	m
H_c	Channel incision depth	m
σ	Water-filled channel cross section	m^2
A_c	Incised cross section	m^2
z_s	Distributed sheet surface elevation	m
ϕ_s	Distributed sheet hydraulic potential	Pa
ϕ_c	Channel hydraulic potential	Pa
q_s	Distributed sheet width-averaged flow	$\text{m}^2 \text{s}^{-1}$
q_c	Channel flow	$\text{m}^3 \text{s}^{-1}$
Ξ_s	Potential energy dissipation in distributed sheet	W m^{-2}
Ξ_c	Potential energy dissipation in channels	W m^{-1}
w_c	Channel width	m
f_e	Exchange fraction	-

model equations as applied to each individual element and edge in the domain, and then explain how the equations are combined to represent the complete domain. Additional details of the numerical implementation are provided in Appendix B. Model variables and their symbols are described in Table 4.1, and model parameters with their symbols are described in Table 4.2.

4.2.1 Sheet model

Slow, distributed flow along the glacier surface is represented as a two-dimensional continuous water sheet. We define h_s to be the water sheet thickness, and z_s to be the ice surface elevation. We assume the water pressure to be equal to the hydrostatic potential [49], and so the hydraulic potential is

$$\phi_s = \rho_w g z_s + \rho_w g h_s. \quad (4.1)$$

Here, ρ_w is the density of water and g is gravitational acceleration. Following Flowers and Clarke [49] and Werder et al. [145], the sheet model is based on conservation of mass. The evolution equation for the water depth is

$$\frac{\partial h_s}{\partial t} + \nabla \cdot \mathbf{q}_s = m_s + \frac{\Xi_s}{\rho_w L}, \quad (4.2)$$

where L is the latent heat of fusion, \mathbf{q}_s is the width-averaged mass flux, m_s is the surface melt source term, and Ξ_s represents melt by frictional potential energy dissipation.

The width averaged volume flux is calculated using a turbulent flow parameterization,

$$\mathbf{q}_s = -k_s h_s^{\alpha_s} \left| \frac{\nabla \phi_s}{\rho_w g} \right|^{\beta_s - 2} \frac{\nabla \phi_s}{\rho_w g}. \quad (4.3)$$

The flow exponents $\alpha_s > 1$ and $\beta_s > 1$ control the turbulence parameterization. For instance, $\alpha_s = 1$ and $\beta_s = 2$ would represent laminar flow. We take $\alpha_s = 5/4$ and $\beta_s = 3/2$ to represent fully turbulent flow [145]. While this is a coarse parameterization, it improves on flow routing models since the flow rate depends nonlinearly on the flow depth. This means that the flow velocity itself decreases as h_s tends to zero.

The potential energy dissipation term Ξ_s represents the energy dissipated by friction between the water and the underlying ice, so that

$$\Xi_s = |\mathbf{q}_s \cdot \nabla \phi_s|. \quad (4.4)$$

The direct inclusion of Ξ_s in equation (4.2) assumes that the ice is at the melting point and so all of the energy dissipated by friction is used immediately to melt the underlying ice. For applications where this is not true, this energy should first be used to warm the surface ice layer, and any remaining energy should be used as a melt source term in equation (4.2). For example, this could be achieved by adding Ξ_s to the net surface energy balance in a coupled surface energy balance and subsurface heat conduction model [e.g. 65].

The ice surface elevation is evolved to account for surface lowering due to surface melt and melt by potential energy dissipation. The time evolution of the ice surface is therefore calculated as

$$\frac{\partial z_s}{\partial t} = -\frac{\Xi_s}{\rho_i L} - m_s \frac{\rho_w}{\rho_i}, \quad (4.5)$$

where m_s is the surface melt rate and ρ_i is the density of the surface layer of ice. We assume a low ice density of 850 kg m^{-3} since this represents the density of the weathered surface layer, consistent with densities commonly used to convert geodetic volume changes to mass changes [154; 69].

4.2.2 Channel model

The supraglacial channel model is based on the same principles as the sheet model, namely mass conservation with a turbulent flow parameterization. As in the sheet model, flow in

Table 4.2: Parameters (top group) and physical constants (bottom group)

Parameter	Description	Units	Default value
α_s	Distributed sheet flow exponent	-	5/4
β_s	Distributed sheet flow exponent	-	3/2
α_c	Channel flow exponent	-	5/3
β_c	Channel flow exponent	-	3/2
k_s	Distributed sheet hydraulic conductivity	$\text{m}^{(2-\alpha_s)} \text{s}^{-1}$	0.5
k_c	Channel hydraulic conductivity	$\text{m}^{(2-\alpha_c)} \text{s}^{-1}$	10
r	Channel width-to-depth ratio	-	3
ζ	Exchange ratio	-	0.2
m_s	Distributed sheet melt rate	m w.e. s^{-1}	-
m_c	Channel melt rate	m w.e. s^{-1}	0
dt	Timestep	s	240
ρ_w	Density of water	kg m^{-3}	1000
ρ_i	Density of ice	kg m^{-3}	850
L	Latent heat of fusion	J kg^{-1}	3.34×10^5
g	Gravitational acceleration	m s^{-2}	9.81

channels melts the underlying ice. Additionally, channels are allowed to grow and shrink in both width and depth due to the balance between melt-out due to surface melt and down-cutting due to frictional melt.

As with the sheet model, the channel model begins with the hydraulic potential. Assuming hydrostatic potential we have

$$\phi_c = \rho_w g z_c + \rho_w g (h_c - H_c), \quad (4.6)$$

where z_c is the elevation of the lip of the channel, h_c is the depth of water in the channel, and H_c is the incision depth (the distance from the base of the channel to the lip; Figure 4.1).

We apply conservation of mass along the channel length to describe the time evolution of the water-filled cross-sectional area in the channel. We include a mass source term from melt by potential energy dissipation, Ξ_c and a prescribed melt term at the base of channels m_c . This prescribed source term could represent additional thermal erosion from the draining of lakes that have been warmed by solar radiation, for example. We set this additional melt to zero in the current work, consistent with most spillway models [e.g. 77], but we have included it in the model description as it may be important for future

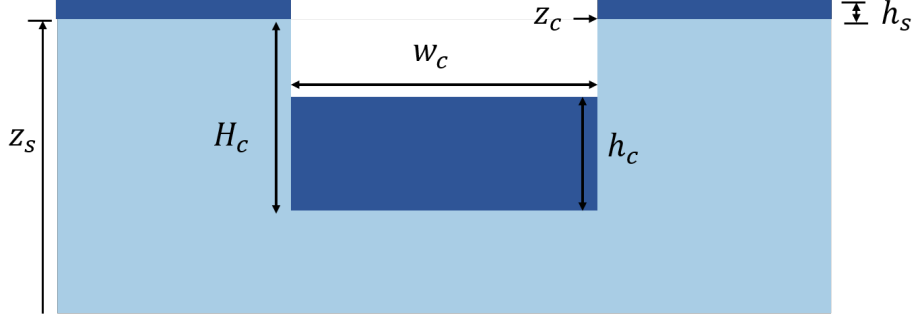


Figure 4.1: Cross-sectional geometry of supraglacial channels.

applications. Therefore, the time evolution equation for the channel water-filled area σ is

$$\frac{\partial \sigma}{\partial t} + \frac{\partial q_c}{\partial s} = w_c m_c + \frac{\Xi_c}{\rho_w L}, \quad (4.7)$$

where q_c is the volume flux in the channel, and w_c is the width of the channel at the level of the water surface.

The channel melt source term Ξ_c is calculated as

$$\Xi_c = \left| q_c \frac{\partial \phi_c}{\partial s} \right|. \quad (4.8)$$

This term represents frictional melt at the base of channels. All potential energy lost by flow across the element is applied as thermal energy to melt the ice along the entire channel perimeter. This term is analogous to the dissipation term in the sheet model (equation (4.4)). Here we have simplified the model by applying heat dissipation along the entire channel perimeter, rather than the wetted perimeter only. To apply heat dissipation along the wetted perimeter would cause the channel cross-sections to change over time and we would need to model this evolution by discretizing the channel perimeter.

Next, we model the evolution of the total incised channel cross-section, A_c , as the balance between the net melt rate and melt due to energy dissipation,

$$\frac{\partial A_c}{\partial t} = \frac{\Xi_c}{\rho_i L} + w_c \frac{\rho_w}{\rho_i} (m_c - m_s). \quad (4.9)$$

The elevation of the channel lip is evolved according to the rate of surface lowering in the adjacent ice sheet surface due to surface melt,

$$\frac{dz_c}{dt} = -m_s \frac{\rho_w}{\rho_i}. \quad (4.10)$$

We calculate volume flux in the channels using a turbulent flow parameterization,

$$q_c = -k_c w_c h_c^{\alpha_c} \left| \frac{1}{\rho_w g} \frac{\partial \phi_c}{\partial s} \right|^{\beta_c - 2} \frac{1}{\rho_w g} \frac{\partial \phi_c}{\partial s}. \quad (4.11)$$

In this equation, $\alpha_c > 1$ and $\beta_c > 1$ have the same role as α_s and β_s in equation (4.3). We take $\alpha_c = 5/3$ and $\beta_c = 3/2$, representing fully turbulent Darcy flow [118; 87; 145] (also called Forchheimer’s law).

To derive the equations for the evolution of the channel water thickness and incision depth from equations (4.7) and (4.9), we assume that channels have a rectangular cross section with a constant aspect ratio. This means that $w_c = rH_c$, where r is the constant width-to-depth ratio. Under this assumption, we derive the final equations for the evolution of the water depth and incision depth:

$$w_c \frac{\partial h_c}{\partial t} + \frac{\partial q_c}{\partial s} = w_c m_c + \frac{\Xi_c}{\rho_w L} - h_c \frac{\partial w_c}{\partial t}, \quad (4.12)$$

and,

$$\frac{dH_c}{dt} = \frac{1}{2} \frac{\rho_w}{\rho_i} (m_c - m_s) + \frac{1}{2w_c} \frac{\Xi_c}{\rho_i L}. \quad (4.13)$$

From these two equations, combined with equation (4.10), we calculate the evolution of the hydraulic potential:

$$\frac{d\phi_c}{dt} = \rho_w g \left(\frac{dz_c}{dt} + \frac{\partial h_c}{\partial t} - \frac{dH_c}{dt} \right). \quad (4.14)$$

4.2.3 Mass exchange

We wish to represent the fact that flow begins at high elevations as a distributed sheet and becomes channelized at lower elevations once sufficient flow accumulates, without assuming prior knowledge of the channel network. We model this process by allowing mass to be transferred from the distributed sheet into the channel system. We treat every interior edge in the triangular mesh equally as a possible location for a supraglacial stream and let the channel network evolve naturally according to the balance between heat dissipation and surface melt.

Mass exchange is regulated by the hydraulic potential difference between the sheet and the channels. At each edge, the model calculates the projection of the sheet flow vector on the outward unit normal vector,

$$q_n = \mathbf{q}_s \cdot \mathbf{n}.$$

If $q_n < 0$, the flow in the sheet is directed inwards along the edge, and so mass is not transferred to the edge. If $q_n > 0$ flow is directed outwards along the edge, and we calculate the sheet potential on the element edge. We let a fraction f_e ($0 \leq f_e \leq 1$) of the mass crossing the edge be taken up by the channel so that we add a mass source term

$$m_e = f_e l q_n \quad (4.15)$$

to equation (4.12), and remove this amount of mass from the element, where l is the length of the edge.

Any physical parameterization of the exchange fraction should satisfy two conditions. First, the channel should be hydrologically disconnected from the sheet when the water in the channel is below the sheet surface. That is, the flow from the adjacent sheet elements should freely flow into the channel. Second, the channel should overflow towards the downhill neighboring element when the water in the channel is above the water level on the neighboring sheet.

We parameterize the exchange fraction, f_e , as a function of the channel incision depth (H_c), water depth in the channel (h_c), and the sheet water depth interpolated to the channel edge h_{sc} . Ideally, we would transfer all the mass crossing an edge into the channel until it is exactly full, at which point zero mass would be transferred. However, such a sharp transition is too numerically unstable. Instead, the exchange fraction is equal to 1 until the water depth in the channel reaches a threshold ratio, ζ , from the top of the channel. For instance, if $\zeta = 0.1$, the exchange fraction is 1 until the water depth reaches the top 10% of the channel wall. We also enforce that the exchange fraction reaches 0 when the water surface height in the channel is greater than or equal to the interpolated sheet water height. This means that the systems are decoupled, so the channel system is free to evacuate the excess water and the sheet system continues routing water from high to low potential. The exchange fraction is linearly interpolated when the channel water thickness is between these extremes. Mathematically, this parameterization is:

$$f_e = \begin{cases} 1, & h_c \leq (1 - \zeta)H_c \\ 1 - \frac{h_c - (1 - \zeta)H_c}{\zeta H_c + h_{sc}}, & (1 - \zeta)H_c < h_c < H_c + h_{sc} \\ 0, & h_c \geq H_c + h_{sc}. \end{cases} \quad (4.16)$$

4.2.4 Summary of model equations

The five fundamental model equations are the evolution equations for h_s (4.2), z_s (4.5), h_c (4.12), H_c (4.13), and ϕ_c (4.14):

$$\frac{\partial h_s}{\partial t} + \nabla \cdot \mathbf{q}_s = m_s + \frac{\Xi_s}{\rho_w L} \quad (4.17)$$

$$\frac{\partial z_s}{\partial t} = -\frac{\Xi_s}{\rho_i L w_c} - m_s \frac{\rho_w}{\rho_i} \quad (4.18)$$

$$w_c \frac{\partial h_c}{\partial t} + \frac{\partial q_c}{\partial s} = w_c m_c + \frac{\Xi_c}{\rho_w L} - h_c \frac{\partial w_c}{\partial t} \quad (4.19)$$

$$\frac{dH_c}{dt} = \frac{1}{2} \frac{\rho_w}{\rho_i} (m_c - m_s) + \frac{1}{2w_c} \frac{\Xi_c}{\rho_i L} \quad (4.20)$$

$$\frac{d\phi_c}{dt} = \rho_w g \left(-m_s \frac{\rho_w}{\rho_i} + \frac{\partial h_c}{\partial t} - \frac{dH_c}{dt} \right) \quad (4.21)$$

The flux parameterizations for \mathbf{q}_s (4.3) and q_c (4.11), and the heat dissipation parameterizations for Ξ_s (4.4) and Ξ_c (4.8) complete the system.

4.2.5 Numerical methods

We solve the model equations using finite volume methods on the unstructured triangular mesh domain. The sheet model is a relatively standard finite volume problem, which we solve using the finite volume methods described in Chapter 3 with second-order ‘‘WLS2’’ gradient reconstruction. We incorporate the sheet-channel coupling term directly into the calculation of the sheet flux at element boundaries to ensure mass conservation.

For the channel model, we use the methods developed in Chapter 3 with the ‘‘Weighted LS’’ method to calculate the hydraulic potential at nodes and therefore along-channel potential gradients. The edge network is assembled from the individual edges by enforcing mass conservation at nodes as described in Chapter 3. Since here we have moulin, if the node is a moulin or a free-flux boundary node, the mass flowing into the node is removed from the domain, and no flux is routed to any of the downhill edges. This scheme conserves mass exactly and naturally forms a dendritic network. It is similar to the scheme used in GlaDs [145].

The model is stepped forward in time using a standard explicit fourth-order Runge-Kutta method. The timestep is chosen at run-time, and is strongly dependent on the maximum melt rate and the minimum edge length. The timestep is typically between 30 and 240 seconds. The convergence is evaluated by considering the maximum absolute change in the state variables (h_c , H_c , ϕ_c , h_s , ϕ_s) over each timestep.

4.2.6 Boundary conditions

Boundary conditions for the sheet model are imposed on equation (4.2). We impose a hybrid boundary condition that combines Neumann and free-flux boundary conditions on the domain boundary. For each boundary element, we calculate the outward normal component of flow, q_n .

Where the flow is directed into the domain from the boundary ($q_n < 0$), we use a Neumann boundary condition to specify the flow entering the domain. In practice, this flux is usually set to zero. Where the flow is directed towards the boundary ($q_n > 0$) we impose that the flux does not change across the boundary, which allows mass to freely leave the domain. This condition is imposed numerically by directly transferring the flux value from boundary element centroids to boundary edges. We do not need to impose boundary conditions on equation (4.3) because our numerical method is able to calculate the potential gradient for boundary elements without specifying the value at the boundary.

For the channel model, we impose boundary conditions on the mass conservation equation (4.12). For this, we partition the nodes in the domain into Neumann and free-flux groups. For Neumann nodes we impose a zero-flux condition. For free-flux nodes we impose that the total flux flowing towards the node leaves the domain. Together, these conditions allow the channel system to naturally form in the upper reaches and evacuate water through the domain outlet. Our numerical method does not require boundary conditions on equation (4.11).

4.3 Synthetic ice sheet margin experiments

We test the model using the synthetic ice sheet margin geometry of the Subglacial Hydrology Model Intercomparison Experiment [SHMIP; 40]. The ice sheet margin geometry represents a land-terminating segment of the margin, and is similar to that used in Werder et al. [145]. We present modelled moulin hydrographs using standard parameters as well as a suite of sensitivity tests to characterize the model’s spectrum of behaviours.

4.3.1 Ice sheet margin domain

The SHMIP ice sheet margin geometry represents an idealized 100 km long, 20 km wide ice sheet margin (Figure 4.2). The surface elevation from de Fleurian et al. [40] is given by

$$z = 6 \left(\sqrt{x + 5000} - \sqrt{5000} \right) + 1. \quad (4.22)$$

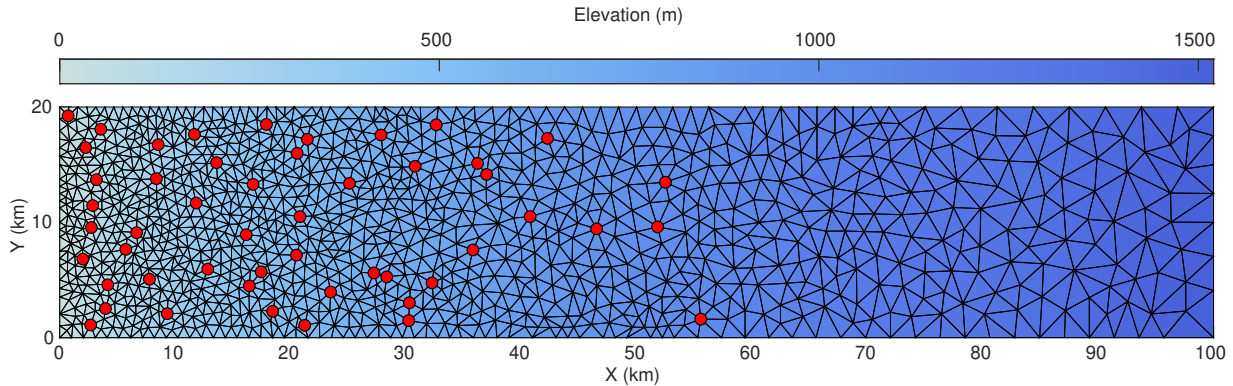


Figure 4.2: Synthetic ice sheet margin domain and triangular mesh. The domain is 100 km long and 20 km wide, and ranges from 1 m to 1521 m elevation following equation (4.22). Moulin locations are indicated by red circular markers.

We solve the model equations on a triangular mesh with 1205 nodes, 3443 edges, and 2239 elements. The mesh is refined by a factor of 10 at lower elevations, where the channel density is expected to be higher due to the greater melt rate. The maximum element area is $6.0 \times 10^6 \text{ m}^2$ at the upper boundary, and $6.0 \times 10^5 \text{ m}^2$ at the lower boundary. The minimum edge length is 625 m near the terminus.

Since our synthetic domain has no topography to naturally concentrate flow in valleys, it is difficult to predict which nodes will be on flow paths. Therefore, we randomly place a large number of moulins throughout the domain, with a higher density of moulins at lower elevation. In this initial stage, we place moulins at up to 60% of nodes. To decide which moulins to keep, we apply the flow-routing stage of the channel model to predict the flow paths. Since removing a moulin impacts downstream moulins, we remove moulins one at a time. At each step, we remove the moulin with the lowest input, and then recalculate the flow paths. We continue this process until we are left with a prescribed number of moulins. For the baseline scenario, we keep 50 moulins. This corresponds to the number of moulins in SHMIP case B4.

4.3.2 Surface melt parameterization

We force the supraglacial model with the simple degree-day melt model used in the SHMIP experiment [40], which we summarize here. We follow the SHMIP model exactly, except for the diurnal amplitude function.

The daily mean sea-level temperature T_0 ($^{\circ}\text{C}$) is parameterized as

$$T_0(t) = -16 \cos\left(\frac{2\pi t}{t_{\text{year}}}\right) - 5 + \Delta T,$$

where t_{year} is the number of seconds in one year and t is the current time in seconds. We take the offset $\Delta T = 0$, corresponding to the standard SHMIP case ‘‘D3’’ [40]. The air temperature is distributed across the domain assuming a constant and uniform lapse rate $\Gamma = -0.0075 \text{ }^{\circ}\text{C m}^{-1}$,

$$T(z) = \Gamma z + T_0.$$

Melt m (m w.e. day^{-1}) is calculated using the degree-day model

$$m(t) = \max\{0, [\Gamma z + T_0(t)] D(t) \text{DDF}\},$$

where $\text{DDF} = 0.01 \text{ m }^{\circ}\text{C}^{-1} \text{ day}^{-1}$ is the degree day factor. $D(t)$ is a diurnally varying melt factor, calculated as

$$D(t) = 1 - A \cos\left(\frac{2\pi t}{t_{\text{day}}}\right),$$

where A is the relative amplitude and t_{day} is the length of one day in seconds (86 400 s). We have changed this diurnal factor from the sine function in the SHMIP model [40] to a cosine function so that the melt rate reaches its minimum at midnight and its maximum at noon. Figure B.2 shows the melt for the synthetic ice sheet margin geometry over the duration of the melt season. This degree day model is used as the source term for the distributed sheet (m_s).

4.3.3 Baseline scenario

The baseline scenario uses default values as listed in Table 4.2, forced by the SHMIP melt model. To allow the supraglacial channel dimensions to adjust to balance the surface melt rate, we first run the model for one melt season as a spinup period. At the end of this period the channel dimensions are nearly in equilibrium with the rate of mass transfer from the elements, and so we use these dimensions as initial conditions for the second melt season. Since there is no topography to influence channel locations, we increase small channels to a minimum channel incision depth of 25 cm to give channels the potential to grow everywhere. This means that even if a channel melted out during the spinup period it is initialized with a 25 cm incision depth. This process represents the perennial nature of large supraglacial rivers [134; 115], while the minimum depth of 25 cm represents the

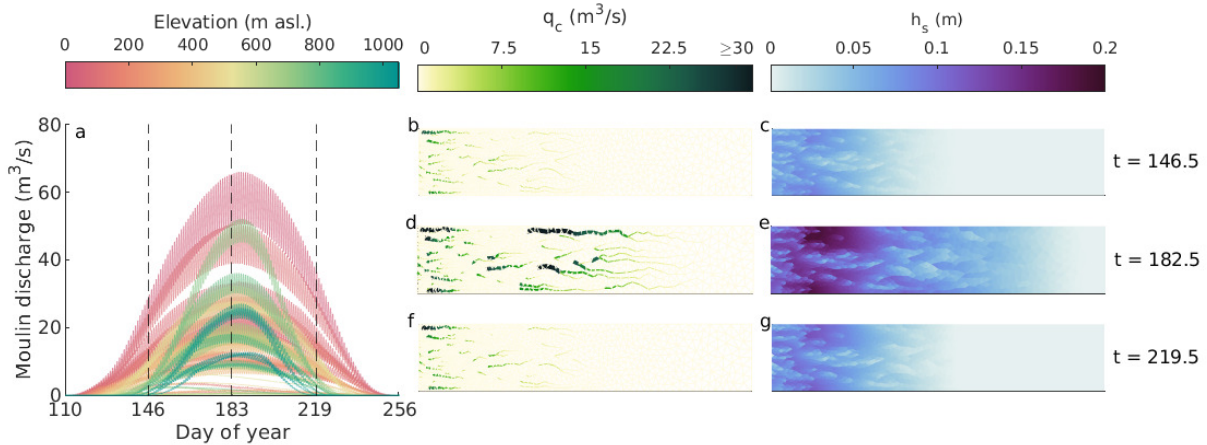


Figure 4.3: Overview of model outputs for the baseline scenario. (a) Moulin flux for the 50 moulins, colored by the elevation of the moulins. The vertical dashed lines indicate the times used for panels (b-g). (b, d, f) Volume flux in the channels at noon on days 146, 182, and 219. (c, e, g) Sheet water thickness at noon on days 146, 182, and 219.

rapid channelization of supraglacial runoff when snow melts at the beginning of the melt season [153; 115].

The modelled water sheet thickness, channel flow, and moulin discharge are shown in Figure 4.3. The sheet thickness is highly variable due to its interaction with the channel system. Large channels draw water out of the sheet, leaving localized regions with very little water in the distributed system. Regions with low channel density, in particular downstream of large moulins, have the most water in the distributed system.

The channel flow maps show evidence of seasonal dynamics. Early in the melt season (Figure 4.3 b) there are numerous small channels with flow $< 5 \text{ m}^3 \text{ s}^{-1}$. By peak melt (Figure 4.3 d) there is significant flow ($> 50 \text{ m}^3 \text{ s}^{-1}$) in the largest channels due to the higher melt rate. Late in the melt season (Figure 4.3 f) the smaller channels have melted out, concentrating more flow into the large channels that remain compared to the early season map, even though the melt rate is the same.

The discharge in the largest moulins peaks at almost $70 \text{ m}^3 \text{ s}^{-1}$. This discharge is high, but not unprecedented, as Echelmeyer and Harrison [45] reported river flow ranging from 50 to $80 \text{ m}^3 \text{ s}^{-1}$ in a large river on Jakobshavn Isbræ. The bulk of the moulins have inputs that peak between 10 to $30 \text{ m}^3 \text{ s}^{-1}$, which is more in line with other measurements of large supraglacial rivers [115].

The moulin hydrographs show additional evidence of seasonal dynamics. Figure 4.4

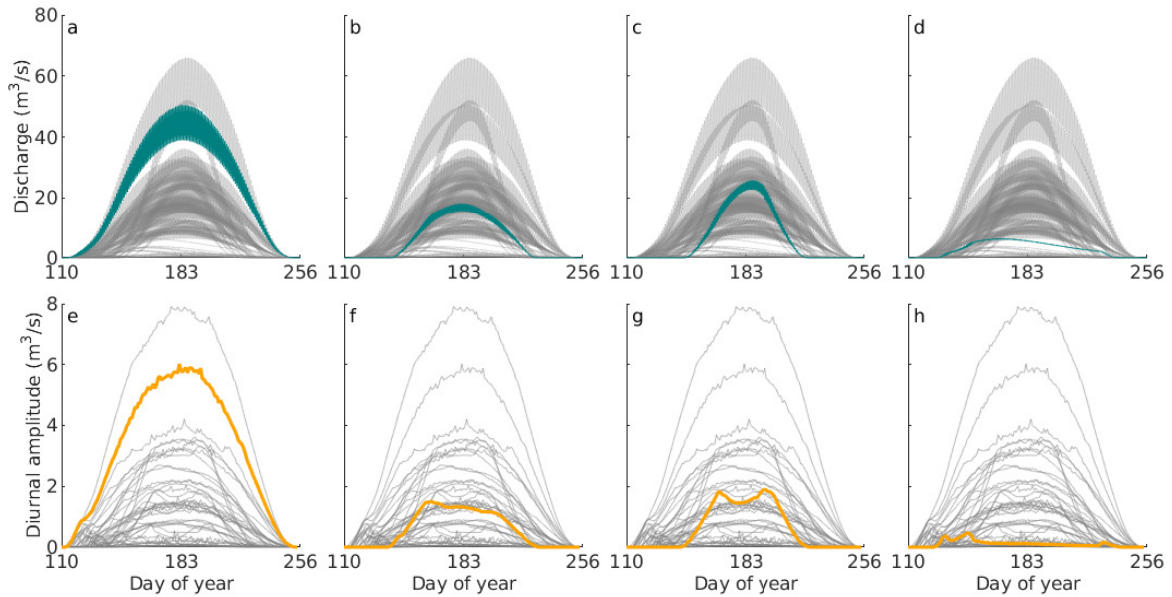


Figure 4.4: Moulin discharge (a-d) and diurnal amplitude (e-h) from the baseline case highlighted for four select moulins, with the discharge and diurnal amplitude for all other moulins shown in gray.

highlights the discharge (teal) and diurnal amplitude (yellow) for moulins representing four typical responses: (1) In Figure 4.4 a, e the discharge and diurnal amplitude are both roughly symmetric and peak shortly after peak melt. This behaviour is similar to what would be predicted by a supraglacial flow-routing model. (2) In Figure 4.4 b, f the diurnal amplitude and discharge in the highlighted case both peak before peak melt and taper off after. However, other moulins with the same pattern of diurnal amplitude may peak before or after peak melt. (3) In Figure 4.4 c, g there are two separate peaks in the diurnal amplitude. Discharge picks up rapidly in the early season and peaks well after peak melt, with a rapid drop off towards the end of the melt season. (4) Several moulins shut off throughout the melt season as the channels that feed them melt out (Figure 4.4 d, h).

4.3.4 Sensitivity tests

We ran a large suite of sensitivity tests to investigate the full range of the model's behaviour and to constrain the set of parameter values where the model produces physically realistic outputs. Since many of the model parameters are poorly constrained, these tests are

Table 4.3: Deviations from the default parameters (Table 4.2) for the sensitivity tests

Case name	Case code	Varied parameter	Value
Conductivity	C1	k_s	$0.5 \text{ m}^{3/4} \text{ s}^{-1}$
Conductivity	C2	k_c	$5 \text{ m}^{1/3} \text{ s}^{-1}$
Exchange fraction	E1	ζ	0.1
Width-to-depth ratio	W1	r	2.0
Width-to-depth ratio	W2	r	5.0
Diurnal melt	D1 ^a	$D(t)$	$D(t) = \max\left(0, -\pi \cos\left(\frac{2\pi t}{t_{\text{Day}}}\right)\right)$
Seasonal melt rate	S1	ΔT	-2°C
Seasonal melt rate	S2	ΔT	2°C
Seasonal melt rate	S3 ^b	ΔT	-2°C
Seasonal melt rate	S4 ^b	ΔT	2°C
Resolution	R1	Number of nodes	582
Resolution	R2	Number of nodes	2451
Timestep	T1	dt	90 s

^aThis $D(t)$ function maintains the same average melt rate and has no melt for 12 hours overnight.

^bCases S3 and S4 are initialized using the channel dimensions after the spinup year of the baseline case.

important to inform applications of the model to real domains. The sensitivity tests are summarized in Table 4.3. Each test varies a single parameter to test its effect on moulin discharges. Here, we present hydrographs for the sensitivity tests (Figure 4.5) and describe the results from a selection of tests in detail.

Parameter sensitivity

As shown in Figure 4.5, the hydraulic conductivity values and the width-to-depth ratio strongly control the moulin inputs. From cases C1 and C2, we see that the sheet conductivity controls the moulin diurnal amplitude, while the channel conductivity controls the moulin discharge rates. With a lower conductivity (case C2) the larger moulins have captured more flow, while the smaller moulins are more likely to shut off.

The width-to-depth ratio regulates the minimum flow required to prevent channels from melting out. Narrower channels sustain channels with lower flow, which means that no moulins shut off in case W1. This leads to a lower peak input into the largest moulins.

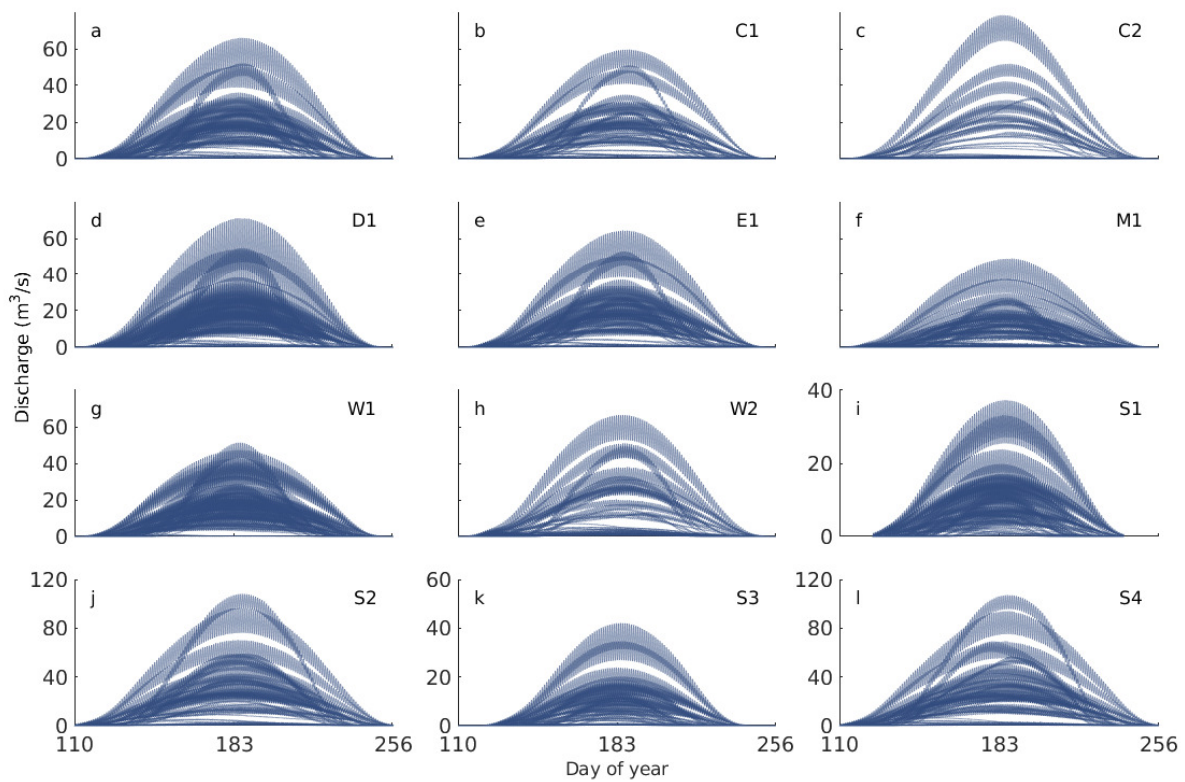


Figure 4.5: Hydrographs for the sensitivity tests described in Table 4.3. (a) Hydrograph for the baseline case for comparison. This is the same data presented in Figure 4.3. (b-l) Hydrographs for the sensitivity tests indicated in the top right corner of each panel. Note the different y-axis scales for (i), (j), (k), and (l).

In the case of wider channels (W2), more moulins shut off and more flow is concentrated in the largest channels. There is also more exaggerated asymmetry in moulin discharges in case W2.

In case T1, reducing the timestep from 180 seconds to 90 seconds changes moulin inputs by only $\sim 1\%$ (Figure B.3). Therefore, we are confident that our default timestep sufficiently resolves the system's dynamics.

For case E1, we decreased the channel exchange ratio ζ to 10%, which more faithfully represents the true physics but is less numerically stable. This only changes moulin inputs by $\sim 4\%$, so we believe the default value of 20% is a good choice for this scenario.

Forcing sensitivity

We included five tests that vary the surface melt rates used to force the model. For case D1 we changed the diurnal melt forcing so that there is no melt overnight for 12 hours while maintaining the daily-averaged melt rate. The main difference in this case is that the moulin inputs have a larger diurnal amplitude, although the seasonal dynamics are similar.

Cases S1 and S2 modified the melt parameterization by using temperature offsets of $\Delta T = -2^\circ\text{C}$ and $\Delta T = 2^\circ\text{C}$, respectively. The results from these cases show similar seasonal patterns of moulin inputs as the baseline, with flow rates scaled according to changes in the melt forcing.

The final sensitivity tests, S3 and S4, have the most interesting dynamics. Cases S3 and S4 are designed to mimic years with abnormally low and high melt, respectively. We change the sea level temperature in the melt model by setting $\Delta T = -2^\circ\text{C}$ for case S3 and $\Delta T = 2^\circ\text{C}$ for case S4, but initialize the model with channel dimensions from the baseline case. This means that the channels are initially out of balance with the melt intensity.

Case S3 is interesting in that it yields moulin inputs that are nearly symmetric. For the most part, moulin inputs peak soon (a few days to a week) after peak melt, and do not show dramatic differences between the early and late melt season. These moulin inputs are therefore similar to what would be predicted by flow routing models that do not represent the seasonal evolution of supraglacial channels.

In contrast, case S4 provides very dynamic moulin discharge curves (Figure 4.6). As in Figure 4.4, the moulins in Figure 4.6 were chosen to show four representative responses. In panels (a) and (e), the discharge is nearly symmetric, whereas the diurnal amplitude is nearly constant through the middle of the melt season. In panels (b) and (f) the discharge

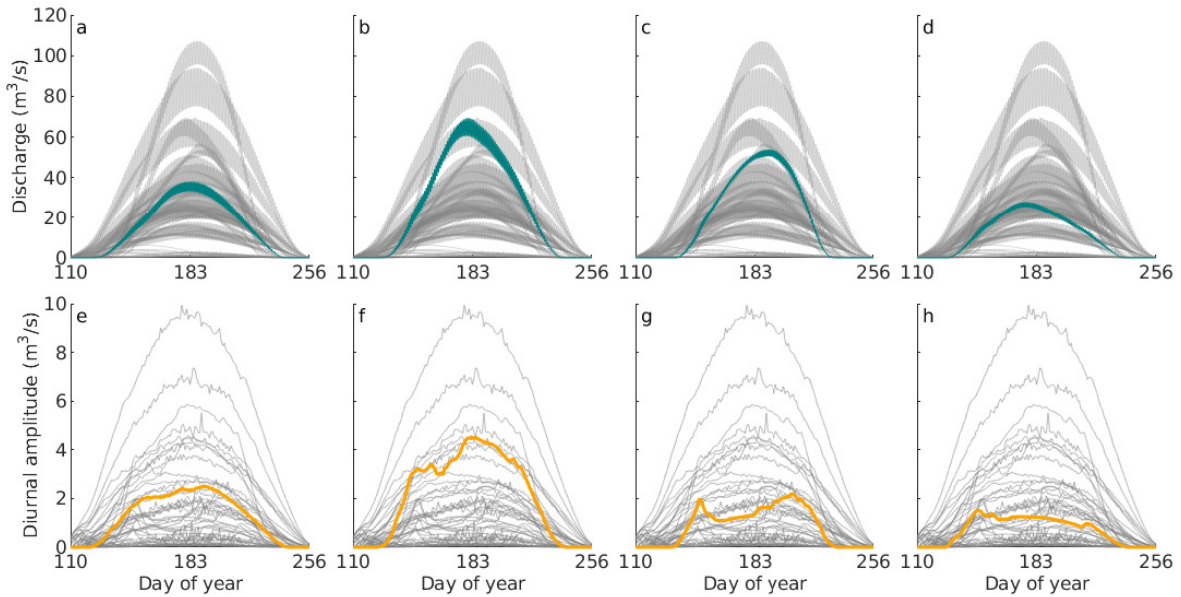


Figure 4.6: Moulin discharge (a-d) and diurnal amplitude (e-h) from case S4 for four select moulins.

peaks early, and the diurnal amplitude has two distinct peaks. In panels (c) and (g) the discharge peaks late, and the diurnal amplitude has an even more prominent double peak. Panels (d) and (h) show a moulin with early peaks in both diurnal amplitude and discharge.

Domain sensitivity

The final tests investigate the sensitivity of modelled moulin inputs to changes in the physical domain, including the number of moulins and the mesh resolution.

To investigate the effect of moulin placement and density we run the model with 100 moulins in case M1 (Figure B.4). In this scenario the distributed water sheet thickness is on average $\sim 20\%$ higher than in the baseline case because of the additional moulins. The water thickness tends to be highest directly downstream of moulins since there is insufficient flow to maintain channels, so increasing the number of moulins increases the total water volume in the distributed system. In the channel flow maps, we see that the peak flow in the channels is significantly lower than in the baseline, as should be expected with more moulins. The seasonal dynamics evident in these maps and in the moulin inputs are similar to the baseline case.

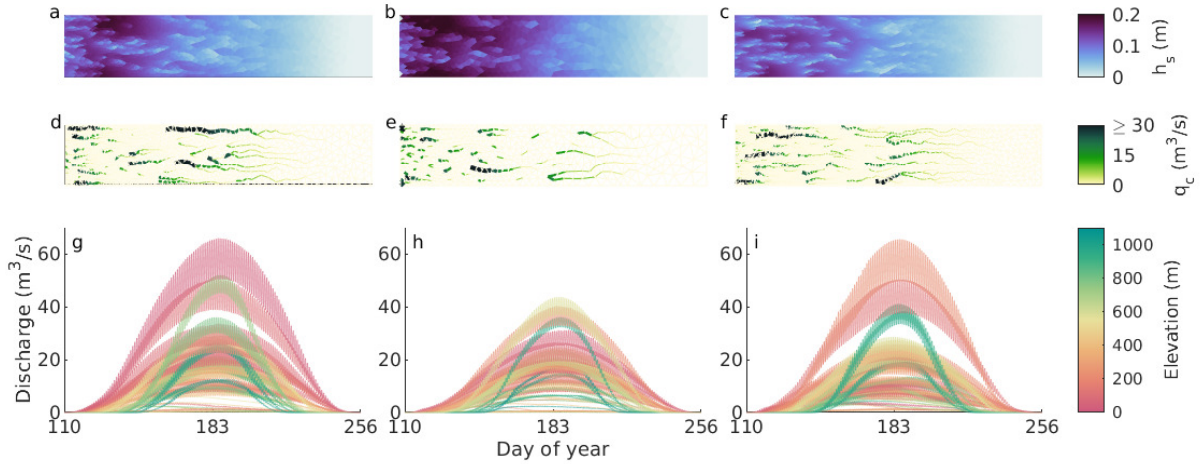


Figure 4.7: modelled drainage system for the baseline case (a, d, g), case R1 with a coarse mesh (b, e, h), and case R2 with a fine mesh (c, f, i). The panels show water sheet thickness (a-c) and channel flow (d-e) at time $t = 182.5$ days, and moulin inputs (g-i).

To test the effect of mesh resolution on the modelled drainage system, the model is applied to a coarser mesh with 582 nodes (case R1) and a finer mesh with 2451 nodes (case R2), compared to the default mesh with 1205 nodes (Figure 4.7, Table S1). The meshes for cases R1 and R2 are refined by the same elevation-dependent factor as the default mesh.

As expected, we needed to use a shorter timestep (90 seconds) for case R2 than for the baseline case (180 seconds) to ensure similar numerical convergence. Interestingly, case R1 required the same timestep as the baseline case. The model runtime for these cases were 11.4 hours for the baseline case, 4.9 hours for case R1, and 46.5 hours for case R2 on a single CPU on Compute Canada’s Graham cluster (Intel E5-2683 v4 Broadwell @ 2.1GHz) with 8 GB of RAM and one CPU.

The sheet thickness maps suggest that the maximum water sheet thickness decreases with the number of nodes in the mesh (Figure 4.7 a,b,c). This can be explained by the fact that the finer meshes have a higher density of possible channel locations, and so finer meshes allow a channel network to form that more evenly takes up mass from the distributed sheet (Figure 4.7 d,e,f).

Due to the nature of the unstructured triangular meshes, each mesh contains unique node locations and moulins are placed at different nodes. This means it is difficult to directly compare moulin hydrographs, and instead we compare the results from a more qualitative perspective. The moulin hydrographs show that the difference between the

baseline case and case R2 is small in terms of moulin inputs, while case R1 has significantly lower flow rates (Figure 4.7 g,h,i). The baseline and R2 have similar maximum input rates (approximately $70 \text{ m}^3\text{s}^{-1}$) and show qualitatively similar seasonal patterns. On the other hand, case R1 has significantly lower maximum input rates (approximately $45 \text{ m}^3\text{s}^{-1}$), but shows similar seasonal patterns.

When applied to a real setting, moulin locations would be known (e.g. from satellite imagery), but other parameters such as the conductivities, the width-to-depth ratio, and the exchange ratio would have to be tested or calibrated, and the number of the nodes in the mesh would need to be adjusted to properly resolve flow across rough topography.

4.4 Internally drained catchments on the Greenland Ice Sheet

To test our model’s ability to calculate moulin inputs in a real setting, we apply the model to a $\sim 27 \times 20 \text{ km}^2$ region of the southwestern Greenland Ice Sheet (Figure 4.8). We have chosen this domain so that we can compare our modelled network development with the existing map of supraglacial rivers, lakes, moulins, and catchments by created by Yang and Smith [151] from a 19 August 2013 Landsat 8 panchromatic image. Our domain includes a subset of eight internally drained catchments, corresponding to the region shown in Figure 4.3 of Yang and Smith [151], and we run the model for the 2013 melt season to coincide with their map.

4.4.1 Input data

We run SaDS using a mesh with 1984 nodes, 5751 edges, 3768 elements, and a maximum element area threshold of $1.5 \times 10^5 \text{ m}^2$. The mesh is refined by a factor of 4 within a 2 km radius of nine supraglacial lake locations. Edge lengths range from 180.9 m to 768.1 m with a median of 419.5 m. The model is run with default parameters as in Table 4.2, with the exception of a 30 second timestep. The short timestep is necessary to ensure numerical stability with the small edge lengths compared to the synthetic experiments and to resolve supraglacial lake dynamics.

We derive a digital elevation model (DEM) for this triangular mesh from 32 m resolution ArcticDEM mosaic tiles [116]. To do this, we smooth the ArcticDEM data using a square two-dimensional moving average filter with an edge length of 45 pixels (1.44 km).

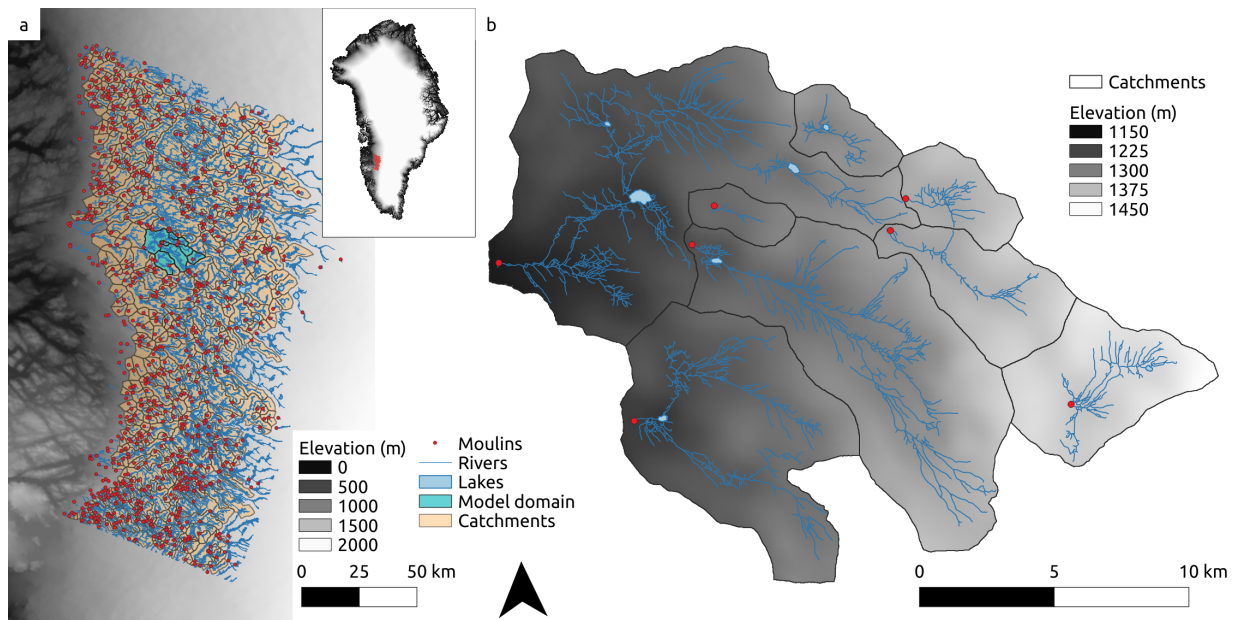


Figure 4.8: Overview of the Greenland model domain. (a) Hydrology features mapped by Yang and Smith [151], with 32 m resolution ArcticDEM [116] shown as the background. The inset shows the location of the study area within Greenland in red. (b) Detailed view of the model domain and mapped rivers shown in (a).

The elevation of each element centroid is calculated as the average value of the smoothed ArcticDEM pixels that lie within the triangular element.

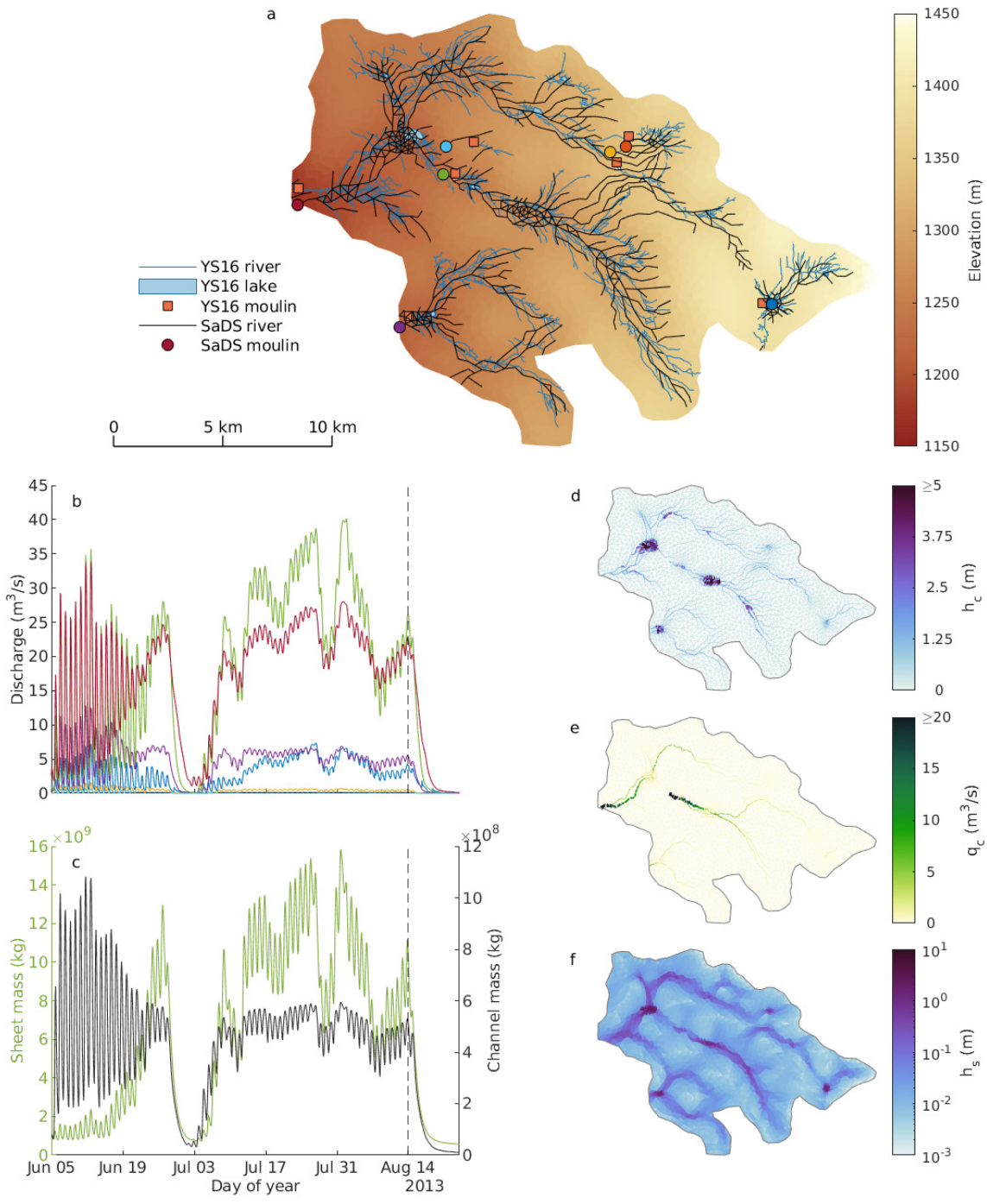
We use the seven moulin locations mapped within the subdomain by Yang and Smith [151] to place moulins in our triangular mesh domain. We shift moulins by up to 1290 m (median 556.3 m) to coincide with local depressions in the DEM and our modelled flow paths. This shift is not surprising since it is only slightly larger than the median edge length, and we are using a different elevation model that is derived from DigitalGlobe WorldView-1, WorldView-2, and WorldView-3 satellite imagery from 2011–2017, whereas the Spirit DEM [81] used by Yang and Smith [151] uses imagery from 2007–2009.

The model is forced with RACMO2.3p2 surface melt data at 5.5 km horizontal resolution and 3 hour temporal resolution [104]. We linearly interpolate this raw data spatially and temporally to calculate melt rates for each element in our triangular mesh. The RACMO data indicates the melt season for our domain spans 5 June to 15 August 2013 (Figure B.5). To ensure the model fully captures the onset of melt and has time to drain at the end of the season, we run the model from 5 June to 18 August 2013. As for the synthetic case, we run the model for one year as a spinup period and present results for the second year. This spinup year is critical to allow channels to adjust to their equilibrium dimensions. Since in this case (unlike with the synthetic setup) we have topography to guide the location of supraglacial channels, we use the channel dimensions from the end of the spinup year directly as initial conditions in the second year.

4.4.2 Results

The modelled outputs are shown in Figure 4.9, where we have used an arbitrary threshold water depth of 30 cm to plot supraglacial river locations. The modelled drainage system closely matches the drainage system mapped by Yang and Smith [151]. SaDS predicts an extensive system of supraglacial channels that is controlled by topography: rivers form in valleys, while distributed flow is dominant along topographic ridges (Figure 4.9 a, d). Several supraglacial lakes are formed by the model, shown by the deep (>1 m) water in the sheet and in the channels (Figure 4.9 d, f). These lakes form in topographic depressions and are fed by both modes of flow.

As with the synthetic case, SaDS predicts dynamic and variable moulin inputs (Figure 4.9 b). Moulin inputs (Figure 4.9 b) have slightly higher diurnal amplitude in the first few weeks of the melt season than in the late season. We also see that moulins have distinct behaviours from one another, in particular in their relaxation time after the cessation of melt.



The total mass in both systems has similar dynamics to the moulin inputs (Figure 4.9 c). The channel mass has slightly lower diurnal amplitude in the late melt season than at the beginning. We also see that the channels very quickly take up mass at the beginning of the melt season compared to the distributed system. However, when melt resumes after the mid-season pause, the systems both take a similar amount of time to reach their saturation values. The nonzero equilibrium value in both systems is due to water storage in lakes.

As a test of the impact of initial conditions following spinup, we also ran the model with all channel locations incised by at least 25 cm at the beginning of the second melt season, as we did for the non-topographically driven synthetic tests. The outputs (Figure B.6) show extremely high diurnal amplitude in the first few weeks of the melt season with moulin inputs nearly halting overnight.

4.5 Discussion

4.5.1 Synthetic ice sheet margin

The modelled supraglacial drainage systems behaves largely as expected. In the SHMIP-inspired synthetic ice sheet margin tests, most of the mass is transported through the channel network, while the distributed sheet acts to control the diurnal amplitude and lag time of moulin inputs.

In the baseline case, moulin discharge lags behind melt forcing by about 5.5–7.5 hours. On a seasonal timescale, moulin discharge generally peaks a few days to a week after peak melt. However, several moulins show more complex dynamics and so are exceptions to this behaviour (Figure 4.4, 5). This behaviour is a direct result of our model’s physics-based treatment of supraglacial channel incision and melt out. For moulins that have high inputs, which are primarily at low elevations, we predict moulin inputs similar to what would be predicted by a routing model [e.g. 8]. This pattern occurs when the moulin is fed by

Figure 4.9 (*preceding page*): (a) Comparison between the modelled drainage system (black lines) and the drainage system mapped by Yang and Smith [151, legend elements indicated by YS16]. The background is colored by the surface elevation. (b) Discharge for the moulins shown in (a). (c) Total mass in the distributed water sheet (left axis, green) and the channel system (right axis, black). The vertical dashed lines in (b) and (c) indicated the time of the maps shown in (d), (e), and (f). (d) Water thickness in supraglacial channels. (e) Channel volume flux. (f) Water sheet thickness (note the logarithmic color scale).

large, perennial channels that consistently take up water from the distributed sheet. When a moulin is fed by smaller channels that may become overwhelmed by the mass inputs from the sheet, or by channels that melt out, the moulin inputs resemble those of Yang et al. [153]. The inputs to these moulins have their maximum diurnal amplitude early in the season, and their discharge may peak before or after peak melt. The "double peak" diurnal amplitude response in Figure 4.4(c, g) occurs for the same reasons, but in this case the channel network is either able to evacuate the excess mass, or grows sufficiently by heat dissipation to take up mass from the sheet again, causing the diurnal amplitude to increase towards the second peak (Figure B.7). Finally, moulin inputs may decrease throughout the melt season as the channels feeding the moulin melt out. This only occurs for moulins with low input rates in regions with low surface slopes.

Beyond these seasonal dynamics, the model predicts long-term evolution of the drainage system. Large channels incise by $\sim 2 \text{ m a}^{-1}$, and flow in the distributed sheet melts the ice sheet surface by up to 15 cm due to heat dissipation (Figure B.8). These channel incision rates compare well to direct observations of 2.5 m a^{-1} in the Canadian High Arctic [134] and 3.3 cm day^{-1} on the Greenland ice sheet (this is equivalent to 2 m a^{-1} assuming a 60 day melt season) [95]. Surface melt by sheet water flow is not usually considered in the energy balance or water budget of glacier surfaces. However, Bash and Moorman [14] suggested that thin sheet flow could be an additional source of surface melt on Fountain Glacier, in the Canadian High Arctic, as they found that errors in their high resolution melt models were correlated with the density of water features.

4.5.2 Sensitivity tests

We carried out a large suite of sensitivity tests (Figure 4.5, Table 4.3). From these tests, we can characterize how sensitive the model is to each parameter, as well as begin to constrain the range of values that parameters may take.

From the sensitivity test hydrographs (Figure 4.5), it is clear that the model is most sensitive to the channel conductivity and the width-to-depth ratio. The channel conductivity controls how much energy is available to melt the underlying ice, so reducing the conductivity causes more small channels to melt out. This acts to concentrate the flow into a few larger channels, which is why there is such inequity in moulin inputs in case C2. The width-to-depth ratio acts in a similar way. Wider channels will melt out more quickly since surface melt reduces the channel cross section much more than for narrower channels. On the other hand, in case W1, the channels are narrow enough that no moulins shut off, and the distribution of flow between moulins is more uniform. These parameters

could be tuned for regions of interest by mapping changes in river networks over a melt season, allowing more accurate model projections.

The resolution sensitivity tests (R1 and R2) demonstrate that the modelled moulin inputs and drainage system behaviour are similar between the default mesh and the fine resolution mesh (Figure 4.7 g,h). The coarse mesh predicts lower moulin inputs (Figure 4.7 g,i) and an erratic channel network, where large rivers (with flux $>10 \text{ m}^3 \text{ s}^{-1}$) are represented by only two or three edges (Figure 4.7 e). These findings suggest that the coarse resolution mesh used in case R1 is insufficient to resolve the supraglacial drainage system. The increase in resolution for case R2 does not appear to be worth the trade-off in model runtime, since the behaviour is qualitatively similar to the baseline case, yet the runtime was four times higher. For these reasons, we believe the baseline mesh with a median edge length of 1232 m is the best choice for this simple synthetic domain.

The lower peak discharge in case M1 compared to the high peak discharge in the baseline run (nearly $70 \text{ m}^3 \text{ s}^{-1}$) suggests that the moulin density in case M1 may be more appropriate than the density in the baseline case. This problem is unique to this synthetic domain since we cannot use satellite imagery or direct observations to place moulins. This finding is interesting as 100 moulins was the highest number considered by the SHMIP experiment, but here we have found this is the most appropriate number for the supraglacial drainage system.

We also see that changes in the total melt volume do not significantly change the drainage system's behaviour as long as the system is in balance with the melt rate. Cases S1 and S2, where the model is run for two years to reach equilibrium, show very similar responses, only scaled in proportion to the mean melt rates. On the other hand, cases S3 and S4, where the channel network is initially not in equilibrium, show complex responses. This likely has important implications for extreme melt years on the Greenland Ice Sheet. While it is beyond the scope of this study, it is an interesting question how these complex moulin inputs would impact the development of the subglacial drainage system in extreme melt years.

The set of default parameters in Table 4.2 is informed by previous modelling studies and direct measurements [145; 115; 57], and in the case of the exchange ratio ζ , to preserve numerical stability. While the conductivities have been measured and reported, it is less clear how to apply the width-to-depth ratio. Measured width-to-depth ratios have been reported as 3.4 to 12 [78], 4.4 to 9.5 [152], and 6.8 to 17.3 [57], however, these ratios are usually taken to be the ratio of the water depth to the wetted width. We have purposely used the ratio of total incision depth of the channel to the total width in our model because we believe adjusting the channel width at the fast timescale of changes in the water depth

is nonphysical and would result in numerical instabilities. Measurements of this width-to-incision depth ratio are less common. For example, St Germain and Moorman [134] reported that deeply incised rivers on Fountain Glacier may have an equal ratio of total incised depth to width. Therefore, we use a ratio of 3 as a midpoint between these cases, although this parameter remains poorly constrained.

4.5.3 Application to the Greenland Ice Sheet

We applied the model to a small domain on the Greenland Ice Sheet composed of several connected internally drained catchments. The modelled drainage system agrees well with maps created from satellite imagery [151], and the system shows similar dynamics to the synthetic ice sheet margin tests. This Greenland drainage test demonstrates that the model is able to predict realistic drainage systems when forced with regional climate model data and DEM-derived surface topography. These results are promising for future application of the model to different catchments and for utilizing its outputs to force subglacial hydrology models.

We note that the map we have used to validate the model [151] was created from a Landsat 8 image from 19 August 2013. This date is outside the melt season predicted by the RACMO melt data, and is five days later than the model outputs we have compared it to (14 August 2013). Since the satellite-derived map was created from the panchromatic image, it is possible that only the dry remnants of the supraglacial drainage system were mapped. It is also possible that the RACMO data incorrectly predicts the timing of the end of the melt season.

The most significant difference compared to the synthetic case is perhaps the presence of supraglacial lakes. SaDS implicitly calculates filling and draining of lakes without requiring DEM sinks to be filled and without pre-calculating lake basins. Since we do not fill sinks in the DEM, water in the sheet and channel systems naturally accumulates in depressions until the lake overflows. The water stored in the lake elements spills over into downhill elements, and the edges spill over into downstream channels. The channels along the lake drainage path take up flow from the elements, effectively creating a lake spillway. This has the same effect as an explicit treatment of supraglacial lakes [e.g. 8; 77], but happens automatically as a result of the model's structure.

4.5.4 Assumptions and simplifications in the model formulation

In developing our mathematical model of the drainage system, we have intentionally used relatively simple parameterizations and reduced the model to a few key equations rather than modelling every detail of the relevant physical mechanisms in order to keep the model transparent and numerically tractable. It is worthwhile to discuss some of the assumptions in more detail.

The model assumes that heat dissipation in the channels melts ice along the entire channel perimeter, rather than just the wetted perimeter (equation (4.9)). This assumption does not capture the details of the physics at play, but it does capture the end result, which is that channel cross section increases as flow in the channel melts the underlying ice. Any energy lost by melting the channel walls above the water surface could be at least partially compensated for by increasing the channel conductivity or reducing the width-to-depth ratio, both of which make it easier for channels to expand.

We acknowledge that our channel geometry parameterization is simplified. The assumption of rectangular channels with a uniform aspect ratio lets us formulate the channel model equations in a straightforward way with a single parameter (the width-to-depth ratio) controlling the geometry of the channel cross-section, instead of requiring additional equations to evolve the channel perimeter [e.g. 73]. Other geometries may work, for example a triangular cross section, but they would be at least as simplified as our choice. The important behaviour here is simply that channels should grow in both width and depth, which our parameterization captures. The impacts of a linear relationship between channel incision depth and width is an interesting question, and nonlinear relationships should be investigated in future work.

Finally, we have not directly addressed all the details of the onset of surface melt in our channel network. Supraglacial channels typically become filled with snow throughout the winter which must be melted before the bare-ice channel walls are exposed. This snow can sometimes plug the channel, forcing the water to be diverted around the snow-plug [134]. These processes are beyond the current resolution capability of the model, but would likely have interesting consequences for moulin inputs at the beginning of the melt season.

More generally, while the model does account for rivers, distributed flow, and lakes, we have excluded some aspects of the supraglacial drainage system. We leave it as future work to include the effect of crevasses interrupting and capturing flow [e.g. 33] and transport, refreezing and/or storage within snow and firn [e.g. 97], and rainfall. Until these mechanisms are incorporated, it is important to carefully choose domains where they are expected to be unimportant.

We used two different initialization procedures to represent the perennial nature of supraglacial channels: (1) applying the channel dimensions from the end of the spinup period, and (2) implementing a minimum incision depth of 25 cm across the domain. For the Greenland case (Figures 8, S6), the initialization has a significant impact on moulin inputs in the first few weeks with much stronger diurnal swings in the minimum incision depth case due to extremely fast flow through the over-developed channel network before small channels melt out. The model is capable of representing either behaviour, and since there are limited measurements of supraglacial river discharge over the entire melt season, and particularly when melt begins in the spring, we cannot be certain which of these is more realistic.

4.6 Conclusions

We have presented the Subaerial Drainage System Model, SaDS. The model combines surface runoff through both a distributed water sheet and within a network of supraglacial channels to calculate moulin input rates. Its unique formulation allows both systems to be modelled dynamically, with mass exchange terms coupling the systems. The model does not rely on pre-determined maps of the supraglacial drainage system. Instead, a network of lakes and rivers emerges naturally depending on the balance between channel erosion and surface melt.

The model was tested using the Subglacial Hydrology Model Intercomparison Project (SHMIP) [40] synthetic ice sheet margin geometry. Modelled moulin inputs show a wide range of realistic, dynamic behaviour. Supraglacial channels with low flow rates melt out, leading to reduced diurnal amplitude in moulin inputs, while large rivers are found to be perennial features, and are responsible for the majority of the runoff transport.

We ran a large suite of sensitivity tests to characterize the range of behaviours the model is capable of reproducing and to constrain possible parameter values. The sensitivity tests suggest that the interannual variability in surface melt is more important for the seasonal patterns of moulin inputs than the absolute melt rate. This finding likely has interesting implications for the development of the subglacial drainage system, and therefore basal sliding, in extreme melt years.

The model was successfully applied to a $\sim 20 \times 27 \text{ km}^2$ region of southwest Greenland. The modelled drainage system includes several supraglacial lakes and an extensive network of supraglacial rivers that agrees well with a satellite-derived map of the drainage system [151]. These results suggest the model should be transferable to other catchments and in different years.

We have made several simplifying assumptions in formulating the model to ensure it is transparent and numerically feasible. Perhaps most important is our assumption that channels have rectangular cross-sections with uniform ratios of total incision depth to channel width. When this ratio is measured in the field, it is usually reported as the ratio of the water depth, not the total incision depth, to the wetted channel width. Therefore, to constrain our model further, we require more field measurements of the total incision depth, width, and cross-sectional shape of incised supraglacial channels across a wide range of discharges.

Compared to existing models, we predict more dynamic and variable moulin inputs. Our model encompasses the behaviour of existing models [e.g. 8; 153], as well as behaviours not predicted by existing models. We do this without relying on prior knowledge of supraglacial river locations or lake basins. The trade-off, however, is complexity. Our model both is mathematically complex and numerically expensive compared to most other models. This makes it best suited for applications where the specific dynamics of moulin inputs are important since it requires skill and an investment in computation time to run. For this type of application, SaDS is a significant step forward.

Chapter 5

Conclusions and future work

5.1 General conclusions

This thesis aimed to advance the state of numerical modelling of meltwater production and drainage on the melting surface of glaciers and ice sheets. Two numerical models were developed to do this: a surface energy balance (SEB) model and the Subaerial Drainage System (SaDS) model.

The SEB model improves on existing models by leveraging high resolution (30 m horizontal resolution) satellite data. However, the improved model requires large amounts of input data, including shortwave and longwave radiation, air temperature, humidity, wind speed, and Landsat 8 imagery (ideally more than one scene) to derive surface albedo.

The model was applied to Kaskawulsh and Nàhùdäy (Lowell Glacier) in the St. Elias Mountains, Yukon. The difference between modelled and measured ablation is within 9% at a range of elevations on both glaciers, improving on the 6–29% errors found in previous studies in the region [147; 92]. Surface shading has a strong local impact (up to 20% along the South Arm of Kaskawulsh), but only reduces glacier-wide total melt by <2%. Debris insulation reduces glacier-wide melt by 7%, while subsurface heat conduction reduces melt at the Kaskawulsh upper station by 8.6%. Similar melt volumes between Kaskawulsh and Nàhùdäy suggest that the surging behaviour of Nàhùdäy is not likely due to differences in surface water input. Instead, following the theory of Benn et al. [17], any differences in enthalpy must come from the subglacial environment. The improved spatial representation of surface melt in the SEB model makes it a valuable tool for future modelling studies.

The SaDS model represents the next step in the path that meltwater takes through the glacier system – flow across the glacier surface. SaDS calculates flow through the

supraglacial drainage system as a distributed sheet and through a discrete river network. This model is the first to combine both modes of flow in a physical model while dynamically evolving the drainage system throughout the melt season. SaDS is tested on a synthetic ice sheet margin domain and on a small portion of the Greenland Ice Sheet.

Results from the synthetic ice sheet margin experiment sensitivity tests constrain suitable parameter values and demonstrate the range of possible behaviours the model can display. The results further suggest that interannual variability in melt intensity is more important than the average melt volume in driving complex seasonal patterns in moulin hydrographs.

When applied to the Greenland Ice Sheet, the modelled drainage system, including both rivers and lakes, coincides well with the satellite-derived map published by Yang and Smith [151]. Due to its conservation-law formulation, SaDS implicitly allows supraglacial lakes to fill and drain within topographic depressions. These results demonstrate the advantages of SaDS, namely that a connected network of supraglacial rivers and lakes forms naturally, without using satellite-derived drainage maps, and that the drainage system evolves throughout the melt season in response to changes in melt intensity.

Together, these tools improve our understanding of supraglacial meltwater processes. The SEB model calculates surface melt, and SaDS routes this meltwater through the drainage system and into moulins. By combining these models, we can predict moulin inputs from meteorological data or climate model predictions. Moreover, the advantages of each of these models work together to further improve calculated moulin inputs. The SEB model focuses on improving the spatial distribution of melt, and with a more accurate assessment of where melt happens, SaDS is more likely to be able to route meltwater through the correct supraglacial catchments and moulins. This will provide more precise information about the location and timing of the delivery of supraglacial meltwater to the subglacial system, therefore allowing existing subglacial models to more accurately compute subglacial pressure and basal sliding.

5.2 Limitations

These models were not directly combined in this thesis as a result of data availability. The SEB model was applied to Kaskawulsh and Nāhūdäy in the St. Elias Mountains because of the availability of several years of weather station, on-ice HOBO sensor, and surface ablation data to apply and validate the model, in addition to the interesting glacier dynamics in the region. Similarly, SaDS was applied to southwest Greenland to compare the

modelled drainage to a satellite-derived map of the supraglacial drainage system created by Yang and Smith [151]. A map of supraglacial drainage systems in the St. Elias Mountains region is currently being developed and will allow future application of both models to the region.

Despite their individual successes, the tools presented here have important limitations. The SEB model requires significant input data and has several poorly constrained parameters even after calibration with in-situ data. The energy balance formulation allows for a wide range of distinct parameter combinations that result in similar melt rates. For instance, lower surface roughness could be compensated for by assuming higher down-glacier wind speeds. This makes it difficult to fully constrain parameters with limited measurements. This type of uncertainty may lead to errors in predictions of future melt rates as the relative importance between each energy balance term shifts under changing climate forcing. This limitation could be overcome by reducing the model to have fewer free parameters or by using an ETI model instead.

SaDS is a relatively simple model for the physical mechanisms it represents, yet it remains a numerically expensive model. Part of this is due to the timescales involved. SaDS represents moulin inputs with roughly hourly temporal resolution, since melt changes rapidly throughout the day, yet it is usually desirable to run for one or more melt seasons that can be up to ~ 100 days long. While this expense is inherent to any supraglacial hydrology model (and the SEB model), SaDS is especially expensive due to its short timestep (30 seconds for the Greenland test) necessary to resolve the fast dynamics of flow through large supraglacial channels with volume flow rates $> 10 \text{ m}^3\text{s}^{-1}$.

The computational expense could be reduced by creating a hybrid model partway between the fully dynamic formulation of SaDS and a static flow routing model. Simple flow routing across elements and through the channel network could be realized with a relatively long timestep (e.g. 1 hour) to calculate moulin inputs and channel flow rates. At the same time, channel incision and melt out rates could be calculated from the surface melt rate and flow accumulation, in the same way that they are in SaDS. Since channel cross sections evolve relatively slowly, this could also be done with a long timestep. This would let the channel network evolve throughout the season while avoiding the expensive parts of the model. This approach is similar to that of Yang et al. [153], but the sheet-channel partitioning would be explicitly modelled rather than parameterized.

5.3 Future work

This thesis describes two models that will be valuable tools in future modelling studies. A clear direction for the next steps would be to use the SEB model outputs to drive SaDS, for example for glaciers in the St. Elias region. This coupling would provide important information about how moulin input rates are controlled by climatic variables.

Moreover, the results of this thesis have suggested a few interesting specific questions. In the synthetic ice sheet margin sensitivity tests, we found that interannual variability in surface melt drove complex seasonal dynamics in moulin inputs. This finding suggests that extreme melt years may have a strong impact on subglacial effective pressure. We could address this question by using the moulin inputs predicted by SaDS as inputs to a subglacial hydrology model, for example GlaDS [145]. SaDS would be important for this coupling since it is the first supraglacial hydrology model to explicitly model seasonal changes in the drainage system. It would be interesting to use this setup to compare subglacial effective pressure throughout the melt season in extreme melt years on the Greenland Ice Sheet (e.g. 2012, 2019) to average and low melt years (e.g. 2016).

More generally, coupling the SEB model presented here, SaDS, and GlaDS would allow predictions of subglacial effective pressure to be made from meteorological observations or climate model predictions. This would provide clear information about how atmospheric conditions control basal sliding and therefore ice velocity. These models could be further coupled to an ice flow model to explicitly predict ice velocities, although this would require a large investment of computation time.

The work contained in this thesis provides a solid basis for future supraglacial hydrology and mass balance modelling studies. More generally, these tools will be valuable components of future studies that aim to answer questions about sea level rise, natural hazard risks, water resource availability, and ecosystem impacts as a result of changing ice melt and dynamics.

References

- [1] Afzal, A., Ansari, Z., Faizabadi, A. R., and Ramis, M. (2017). Parallelization strategies for computational fluid dynamics software: state of the art review. *Archives of Computational Methods in Engineering*, 24(2):337–363. [51](#)
- [2] Altena, B. and Kääb, A. (2017). Weekly glacier flow estimation from dense satellite time series using adapted optical flow technology. *Frontiers in Earth Science*, 5:53. [19](#)
- [3] Andrews, L. C., Poinar, K., and Trunz, C. (2021). Controls on Greenland moulin geometry and evolution from the Moulin Shape model. *The Cryosphere Discussions*, 2021:1–47. [6](#), [13](#)
- [4] Arnold, N., Richards, K., Willis, I., and Sharp, M. (1998). Initial results from a distributed, physically based model of glacier hydrology. *Hydrological Processes*, 12(2):191–219. [9](#), [10](#), [32](#), [66](#)
- [5] Arnold, N., Willis, I., Sharp, M., Richards, K., and Lawson, W. (1996). A distributed surface energy-balance model for a small valley glacier. I. Development and testing for Haut Glacier d’Arolla, Valais, Switzerland. *Journal of Glaciology*, 42(140):77–89. [8](#), [16](#)
- [6] Arnold, N. S., Rees, W. G., Hodson, A. J., and Kohler, J. (2006). Topographic controls on the surface energy balance of a high Arctic valley glacier. *Journal of Geophysical Research: Earth Surface*, 111(F2). [16](#)
- [7] Aubry-Wake, C., Zéphir, D., Baraer, M., McKenzie, J. M., and Marek, B. G. (2018). Importance of longwave emissions from adjacent terrain on patterns of tropical glacier melt and recession. *Journal of Glaciology*, 64(243):49–60. [16](#)
- [8] Banwell, A. F., Arnold, N. S., Willis, I. C., Tedesco, M., and Ahlstrøm, A. P. (2012a). Modeling supraglacial water routing and lake filling on the greenland ice sheet. *Journal of Geophysical Research: Earth Surface*, 117(F4):1–11. [11](#), [12](#), [66](#), [89](#), [92](#), [95](#)

- [9] Banwell, A. F., Willis, I. C., Arnold, N. S., Messerli, A., Rye, C. J., Tedesco, M., and Ahlstrøm, A. P. (2012b). Calibration and evaluation of a high-resolution surface mass-balance model for paakitsoq, west greenland. *Journal of Glaciology*, 58(212):1047–1062. [8](#)
- [10] Barrand, N. E. and Sharp, M. J. (2010). Sustained rapid shrinkage of Yukon glaciers since the 1957–1958 international geophysical year. *Geophysical Research Letters*, 37(7). [15](#)
- [11] Bartholomew, I., Nienow, P., Sole, A., Mair, D., Cowton, T., and King, M. A. (2012). Short-term variability in greenland ice sheet motion forced by time-varying meltwater drainage: Implications for the relationship between subglacial drainage system behavior and ice velocity. *Journal of Geophysical Research: Earth Surface*, 117(F3). [9](#), [10](#)
- [12] Bartholomew, I., Nienow, P., Sole, A., Mair, D., Cowton, T., Palmer, S., and Wadham, J. (2011). Supraglacial forcing of subglacial drainage in the ablation zone of the Greenland ice sheet. *Geophysical Research Letters*, 38(8). [65](#)
- [13] Bash, E. A. and Marshall, S. J. (2014). Estimation of glacial melt contributions to the bow river, alberta, canada, using a radiation-temperature melt model. *Annals of Glaciology*, 55(66):138–152. [2](#)
- [14] Bash, E. A. and Moorman, B. J. (2020). Surface melt and the importance of water flow – an analysis based on high-resolution unmanned aerial vehicle (UAV) data for an Arctic glacier. *The Cryosphere*, 14(2):549–563. [8](#), [16](#), [20](#), [30](#), [31](#), [32](#), [44](#), [46](#), [90](#)
- [15] Beighley, R. E., Eggert, K. G., Dunne, T., He, Y., Gummadi, V., and Verdin, K. L. (2009). Simulating hydrologic and hydraulic processes throughout the Amazon River Basin. *Hydrological Processes*, 23(8):1221–1235. [67](#)
- [16] Benn, D. I. and Evans, D. J. A. (2010). *Glaciers & Glaciation*. Routledge, New York, NY, USA, 2 edition. [2](#), [6](#), [7](#)
- [17] Benn, D. I., Fowler, A. C., Hewitt, I., and Sevestre, H. (2019). A general theory of glacier surges. *Journal of Glaciology*, 65(253):701–716. [18](#), [19](#), [47](#), [96](#)
- [18] Bevington, A. and Copland, L. (2014). Characteristics of the last five surges of Lowell Glacier, Yukon, Canada, since 1948. *Journal of Glaciology*, 60(219):113–123. [18](#), [19](#), [20](#)
- [19] Bond, T. C., Doherty, S. J., Fahey, D. W., Forster, P. M., Berntsen, T., DeAngelo, B. J., Flanner, M. G., Ghan, S., Kärcher, B., Koch, D., Kinne, S., Kondo, Y., Quinn,

- P. K., Sarofim, M. C., Schultz, M. G., Schulz, M., Venkataraman, C., Zhang, H., Zhang, S., Bellouin, N., Guttikunda, S. K., Hopke, P. K., Jacobson, M. Z., Kaiser, J. W., Klimont, Z., Lohmann, U., Schwarz, J. P., Shindell, D., Storelvmo, T., Warren, S. G., and Zender, C. S. (2013). Bounding the role of black carbon in the climate system: A scientific assessment. *Journal of Geophysical Research: Atmospheres*, 118(11):5380–5552. [49](#)
- [20] Box, J. E., Fettweis, X., Stroeve, J. C., Tedesco, M., Hall, D. K., and Steffen, K. (2012). Greenland ice sheet albedo feedback: thermodynamics and atmospheric drivers. *The Cryosphere*, 6(4):821–839. [49](#)
- [21] Braithwaite, R. J. (1995). Positive degree-day factors for ablation on the Greenland ice sheet studied by energy-balance modelling. *Journal of Glaciology*, 41(137):153–160. [8](#)
- [22] Brock, B. W., Willis, I. C., and Sharp, M. J. (2000). Measurement and parameterization of albedo variations at Haut Glacier d’Arolla, Switzerland. *Journal of Glaciology*, 46(155):675–688. [16](#), [20](#)
- [23] Brun, F., Dumont, M., Wagnon, P., Berthier, E., Azam, M. F., Shea, J. M., Sirguey, P., Rabatel, A., and Ramanathan, A. (2015). Seasonal changes in surface albedo of himalayan glaciers from MODIS data and links with the annual mass balance. *The Cryosphere*, 9(1):341–355. [22](#)
- [24] Buzzard, S. C., Feltham, D. L., and Flocco, D. (2018). A mathematical model of melt lake development on an ice shelf. *Journal of Advances in Modeling Earth Systems*, 10(2):262–283. [17](#), [28](#), [32](#), [33](#)
- [25] Chesnokova, A., Baraër, M., Laperrière-Robillard, T., and Huh, K. (2020). Linking mountain glacier retreat and hydrological changes in southwestern Yukon. *Water Resources Research*, 56(1):e2019WR025706. [15](#)
- [26] Christianson, K., Kohler, J., Alley, R. B., Nuth, C., and van Pelt, W. J. J. (2015). Dynamic perennial firn aquifer on an arctic glacier. *Geophysical Research Letters*, 42(5):1418–1426. [66](#)
- [27] Chu, V. W. (2014). Greenland ice sheet hydrology: A review. *Progress in Physical Geography: Earth and Environment*, 38(1):19–54. [4](#), [5](#), [65](#), [66](#)

- [28] Cirací, E., Velicogna, I., and Swenson, S. (2020). Continuity of the mass loss of the world’s glaciers and ice caps from the GRACE and GRACE Follow-On missions. *Geophysical Research Letters*, 47(9):e2019GL086926. e2019GL086926 10.1029/2019GL086926. [15](#)
- [29] Clague, J. J. and Rampton, V. N. (1982). Neoglacial Lake Alesk. *Canadian Journal of Earth Sciences*, 19(1):94–117. [19](#)
- [30] Clarke, G. K. and Blake, E. W. (1991). Geometric and thermal evolution of a surge-type glacier in its quiescent state: Trapridge Glacier, Yukon Territory, Canada, 1969–89. *Journal of Glaciology*, 37(125):158–169. [18](#)
- [31] Clarke, G. K. and Holdsworth, G. (2002). Glaciers of the St. Elias Mountains. *US Geological Survey professional paper*, 1386J. [15](#), [18](#), [19](#)
- [32] Clarke, G. K. C., Schmok, J. P., Ommanney, C. S. L., and Collins, S. G. (1986). Characteristics of surge-type glaciers. *Journal of Geophysical Research: Solid Earth*, 91(B7):7165–7180. [18](#)
- [33] Clason, C., Mair, D. W., Burgess, D. O., and Nienow, P. W. (2012). Modelling the delivery of supraglacial meltwater to the ice/bed interface: application to southwest Devon Ice Cap, Nunavut, Canada. *Journal of Glaciology*, 58(208):361–374. [9](#), [10](#), [66](#), [93](#)
- [34] Clason, C. C., Mair, D. W. F., Nienow, P. W., Bartholomew, I. D., Sole, A., Palmer, S., and Schwanghart, W. (2015). Modelling the transfer of supraglacial meltwater to the bed of leverett glacier, southwest greenland. *The Cryosphere*, 9(1):123–138. [9](#), [10](#), [66](#)
- [35] Collier, E., Maussion, F., Nicholson, L. I., Mölg, T., Immerzeel, W. W., and Bush, A. B. G. (2015). Impact of debris cover on glacier ablation and atmosphere–glacier feedbacks in the Karakoram. *The Cryosphere*, 9(4):1617–1632. [26](#)
- [36] Cook, S. J., Christoffersen, P., Todd, J., Slater, D., and Chauché, N. (2020). Coupled modelling of subglacial hydrology and calving-front melting at Store Glacier, West Greenland. *The Cryosphere*, 14(3):905–924. [9](#)
- [37] Corripio, J. G. (2003). Vectorial algebra algorithms for calculating terrain parameters from DEMs and solar radiation modelling in mountainous terrain. *International Journal of Geographical Information Science*, 17(1):1–23. [25](#), [30](#)
- [38] Crawford, T. and Duchon, C. (1999). An improved parameterization for estimating downwelling longwave radiation at the Earth’s surface. *J. Appl. Meteor*, 38:474–480. [23](#)

- [39] Cuffey, K. M. and Paterson, W. S. B. (2010). *The physics of glaciers*. Academic Press. [18](#)
- [40] de Fleurian, B., Werder, M. A., Beyer, S., Brinkerhoff, D. J., Delaney, I., Dow, C. F., Downs, J., Gagliardini, O., Hoffman, M. J., Hooke, R. L., Seguinot, J., and Sommers, A. N. (2018). SHMIP the subglacial hydrology model intercomparison project. *Journal of Glaciology*, 64(248):897–916. [13](#), [67](#), [75](#), [76](#), [77](#), [94](#), [125](#)
- [41] Di Mauro, B., Garzonio, R., Baccolo, G., Franzetti, A., Pittino, F., Leoni, B., Remias, D., Colombo, R., and Rossini, M. (2020). Glacier algae foster ice-albedo feedback in the European Alps. *Scientific reports*, 10(1):1–9. [49](#)
- [42] Dumont, M., Brun, E., Picard, G., Michou, M., Libois, Q., Petit, J., Geyer, M., Morin, S., and Josse, B. (2014). Contribution of light-absorbing impurities in snow to Greenland’s darkening since 2009. *Nature Geoscience*, 7(7):509–512. [49](#)
- [43] Ebrahimi, S. and Marshall, S. J. (2015). Parameterization of incoming longwave radiation at glacier sites in the Canadian Rocky Mountains. *Journal of Geophysical Research: Atmospheres*, 120(24):12536–12556. [24](#)
- [44] Ebrahimi, S. and Marshall, S. J. (2016). Surface energy balance sensitivity to meteorological variability on Haig Glacier, Canadian Rocky Mountains. *The Cryosphere*, 10(6):2799–2819. [8](#), [16](#), [20](#), [23](#), [30](#), [31](#), [32](#), [44](#)
- [45] Echelmeyer, K. and Harrison, W. D. (1990). Jakobshavns Isbræ, West Greenland: Seasonal variations in velocity - or lack thereof. *Journal of Glaciology*, 36(122):82–88. [78](#)
- [46] Engelhardt, M., Schuler, T. V., and Andreassen, L. M. (2015). Sensitivities of glacier mass balance and runoff to climate perturbations in Norway. *Annals of Glaciology*, 56(70):79–88. [16](#)
- [47] Fitzpatrick, N., Radić, V., and Menounos, B. (2017). Surface energy balance closure and turbulent flux parameterization on a mid-latitude mountain glacier, Purcell Mountains, Canada. *Frontiers in Earth Science*, 5:67. [8](#), [16](#), [32](#), [44](#)
- [48] Fitzpatrick, N., Radić, V., and Menounos, B. (2019). A multi-season investigation of glacier surface roughness lengths through in situ and remote observation. *The Cryosphere*, 13(3):1051–1071. [44](#)

- [49] Flowers, G. E. and Clarke, G. K. C. (2002). A multicomponent coupled model of glacier hydrology 1. theory and synthetic examples. *Journal of Geophysical Research: Solid Earth*, 107(B11):ECV 9–1–ECV 9–17. [10](#), [11](#), [66](#), [68](#)
- [50] Flowers, G. E., Copland, L., and Schoof, C. G. (2014). Contemporary glacier processes and global change: Recent observations from Kaskawulsh Glacier and the Donjek Range, St. Elias Mountains. *Arctic*, 67:22–34. [19](#)
- [51] Forster, R. R., Box, J. E., Van Den Broeke, M. R., Miège, C., Burgess, E. W., Van Angelen, J. H., Lenaerts, J. T., Koenig, L. S., Paden, J., Lewis, C., et al. (2014). Extensive liquid meltwater storage in firn within the greenland ice sheet. *Nature Geoscience*, 7(2):95–98. [66](#)
- [52] Fountain, A. G. and Walder, J. S. (1998). Water flow through temperate glaciers. *Reviews of Geophysics*, 36(3):299–328. [6](#), [65](#)
- [53] Foy, N., Copland, L., Zdanowicz, C., Demuth, M., and Hopkinson, C. (2011). Recent volume and area changes of Kaskawulsh Glacier, Yukon, Canada. *Journal of Glaciology*, 57(203):515–525. [15](#), [19](#), [20](#)
- [54] Fyffe, C. L., Reid, T. D., Brock, B. W., Kirkbride, M. P., Diolaiuti, G., Smiraglia, C., and Diotri, F. (2014). A distributed energy-balance melt model of an alpine debris-covered glacier. *Journal of Glaciology*, 60(221):587–602. [17](#), [26](#)
- [55] Gagliardini, O. and Werder, M. A. (2018). Influence of increasing surface melt over decadal timescales on land-terminating greenland-type outlet glaciers. *Journal of Glaciology*, 64(247):700–710. [13](#)
- [56] Ghosal, A. (2021). Himalayan glacier disaster highlights climate change risks. *Associated Press*. [1](#)
- [57] Gleason, C. J., Smith, L. C., Chu, V. W., Legleiter, C. J., Pitcher, L. H., Overstreet, B. T., Rennermalm, A. K., Forster, R. R., and Yang, K. (2016). Characterizing supraglacial meltwater channel hydraulics on the greenland ice sheet from in situ observations. *Earth Surface Processes and Landforms*, 41(14):2111–2122. [91](#)
- [58] Gleason, C. J., Yang, K., Feng, D., Smith, L. C., Liu, K., Pitcher, L. H., Chu, V. W., Cooper, M. G., Overstreet, B. T., Rennermalm, A. K., and Ryan, J. C. (2021). Hourly surface meltwater routing for a Greenlandic supraglacial catchment across hillslopes and through a dense topological channel network. *The Cryosphere*, 15(5):2315–2331. [10](#), [12](#), [67](#)

- [59] Goelzer, H., Nowicki, S., Payne, A., Larour, E., Seroussi, H., Lipscomb, W. H., Gregory, J., Abe-Ouchi, A., Shepherd, A., Simon, E., Agosta, C., Alexander, P., Aschwanden, A., Barthel, A., Calov, R., Chambers, C., Choi, Y., Cuzzone, J., Dumas, C., Edwards, T., Felikson, D., Fettweis, X., Gолledge, N. R., Greve, R., Humbert, A., Huybrechts, P., Le clec’h, S., Lee, V., Leguy, G., Little, C., Lowry, D. P., Morlighem, M., Nias, I., Quiquet, A., Rückamp, M., Schlegel, N.-J., Slater, D. A., Smith, R. S., Straneo, F., Tarasov, L., van de Wal, R., and van den Broeke, M. (2020). The future sea-level contribution of the Greenland ice sheet: a multi-model ensemble study of ISMIP6. *The Cryosphere*, 14(9):3071–3096. [4](#)
- [60] Greuell, W. and Konzelmann, T. (1994). Numerical modelling of the energy balance and the englacial temperature of the Greenland Ice Sheet. Calculations for the ETH-camp location (West Greenland, 1155 m a.s.l.). *Global and Planetary Change*, 9(1):91 – 114. Greenland ice margin experiment (GIMEx). [17](#), [28](#), [32](#), [33](#)
- [61] Harrison, S., Kargel, J. S., Huggel, C., Reynolds, J., Shugar, D. H., Betts, R. A., Emmer, A., Glasser, N., Haritashya, U. K., Klimeš, J., Reinhardt, L., Schaub, Y., Wiltshire, A., Regmi, D., and Vilimek, V. (2018). Climate change and the global pattern of moraine-dammed glacial lake outburst floods. *The Cryosphere*, 12(4):1195–1209. [2](#), [3](#)
- [62] Herdes, È. (2014). Evolution of seasonal variations in motion of the Kaskawulsh Glacier, Yukon Territory. Master’s thesis, Department of Geography, University of Ottawa. [16](#), [19](#), [23](#), [33](#)
- [63] Herzfeld, U. C., Stauber, M., and Stahl, N. (2000). Geostatistical characterization of ice surfaces from ERS-1 and ERS-2 SAR data, Jakobshavn Isbræ, Greenland. *Annals of Glaciology*, 30:224–234. [44](#)
- [64] Hill, T. and Dow, C. F. (submitted). Modeling the dynamics of supraglacial rivers and distributed meltwater flow with the Subaerial Drainage System (SaDS) model. *Journal of Geophysical Research: Earth Surface*, 2021JF006309. [5](#), [14](#)
- [65] Hill, T., Dow, C. F., Bash, E. A., and Copland, L. (2021). Application of an improved surface energy balance model to two large valley glaciers in the St. Elias Mountains, Yukon. *Journal of Glaciology*, 67(262):297–312. [13](#), [69](#)
- [66] Hock, R. (1999). A distributed temperature-index ice- and snowmelt model including potential direct solar radiation. *Journal of Glaciology*, 45(149):101–111. [8](#)
- [67] Hock, R. (2005). Glacier melt: a review of processes and their modelling. *Progress in Physical Geography: Earth and Environment*, 29(3):362–391. [8](#), [32](#)

- [68] Hock, R., Bliss, A., Marzeion, B., Giesen, R. H., Yukio, H., Huss, M., Radić, V., and Slangen, A. B. A. (2019). GlacierMIP – a model intercomparison of global-scale glacier mass-balance models and projections. *Journal of Glaciology*, 65(251):453–467. [15](#)
- [69] Huss, M. (2012). Extrapolating glacier mass balance to the mountain-range scale: the European Alps 1900–2100. *The Cryosphere*, 6(4):713–727. [69](#)
- [70] Huss, M. and Hock, R. (2018). Global-scale hydrological response to future glacier mass loss. *Nature Climate Change*, 8(2):135–140. [2](#), [15](#)
- [71] Iken, A. and Bindschadler, R. A. (1986). Combined measurements of subglacial water pressure and surface velocity of Findelengletscher, Switzerland: Conclusions about drainage system and sliding mechanism. *Journal of Glaciology*, 32(110):101–119. [16](#), [19](#)
- [72] Ito, Y. (2013). Challenges in unstructured mesh generation for practical and efficient computational fluid dynamics simulations. *Computers & Fluids*, 85:47–52. International Workshop on Future of CFD and Aerospace Sciences. [51](#)
- [73] Jarosch, A. H. and Gudmundsson, M. T. (2012). A numerical model for meltwater channel evolution in glaciers. *The Cryosphere*, 6(2):493–503. [6](#), [66](#), [93](#)
- [74] Joughin, I., Das, S. B., Flowers, G., Behn, M. D., Alley, R. B., King, M. A., Smith, B., Bamber, J., van den Broeke, M. R., and Van Angelen, J. (2013). Influence of ice-sheet geometry and supraglacial lakes on seasonal ice-flow variability. *The Cryosphere*, 7(4):1185–1192. [65](#)
- [75] Kargel, J. S., Leonard, G. J., Bishop, M. P., Käab, A., and Raup, B. H., editors (2014). *Global land ice measurements from space*. Springer. [1](#), [4](#)
- [76] King, M. D., Howat, I. M., Candela, S. G., Noh, M. J., Jeong, S., Noël, B. P., van den Broeke, M. R., Wouters, B., and Negrete, A. (2020). Dynamic ice loss from the Greenland Ice Sheet driven by sustained glacier retreat. *Communications Earth & Environment*, 1(1):1–7. [2](#), [65](#)
- [77] Kingslake, J., Ng, F., and Sole, A. (2015). Modelling channelized surface drainage of supraglacial lakes. *Journal of Glaciology*, 61(225):185–199. [10](#), [11](#), [66](#), [70](#), [92](#)
- [78] Knighton, A. D. (1985). Channel form adjustment in supraglacial streams, Austre Okstindbreen, Norway. *Arctic and Alpine Research*, 17(4):451–466. [91](#)

- [79] Kochtitzky, W., Jiskoot, H., Copland, L., Enderlin, E., McNabb, R., Kreutz, K., and Main, B. (2019). Terminus advance, kinematics and mass redistribution during eight surges of Donjek Glacier, St. Elias Range, Canada, 1935 to 2016. *Journal of Glaciology*, 65(252):565–579. [18](#), [19](#)
- [80] Koenig, L. S., Miège, C., Forster, R. R., and Brucker, L. (2014). Initial in situ measurements of perennial meltwater storage in the Greenland firn aquifer. *Geophysical Research Letters*, 41(1):81–85. [66](#)
- [81] Korona, J., Berthier, E., Bernard, M., Rémy, F., and Thouvenot, E. (2009). SPIRIT. Spot 5 stereoscopic survey of Polar Ice: Reference Images and Topographies during the fourth International Polar Year (2007–2009). *ISPRS Journal of Photogrammetry and Remote Sensing*, 64(2):204–212. [87](#)
- [82] Koziol, C., Arnold, N., Pope, A., and Colgan, W. (2017). Quantifying supraglacial meltwater pathways in the Paakitsoq region, West Greenland. *Journal of Glaciology*, 63(239):464–476. [66](#)
- [83] Koziol, C. P. and Arnold, N. (2018). Modelling seasonal meltwater forcing of the velocity of land-terminating margins of the greenland ice sheet. *The Cryosphere*, 12(3):971–991. [10](#), [12](#)
- [84] Kraaijenbrink, P., Bierkens, M., Lutz, A., and Immerzeel, W. (2017). Impact of a global temperature rise of 1.5 degrees Celsius on Asia’s glaciers. *Nature*, 549(7671):257–260. [46](#)
- [85] Kraaijenbrink, P. D. A., Shea, J. M., Litt, M., Steiner, J. F., Treichler, D., Koch, I., and Immerzeel, W. W. (2018). Mapping surface temperatures on a debris-covered glacier with an Unmanned Aerial Vehicle. *Frontiers in Earth Science*, 6:64. [16](#), [26](#)
- [86] Lee, B.-K. (2011). Computational fluid dynamics in cardiovascular disease. *Korean circulation journal*, 41(8):423–430. [51](#)
- [87] Leeson, A. A., Shepherd, A., Palmer, S., Sundal, A., and Fettweis, X. (2012). Simulating the growth of supraglacial lakes at the western margin of the greenland ice sheet. *The Cryosphere*, 6(5):1077–1086. [10](#), [11](#), [72](#)
- [88] Leuliette, E. W. and Nerem, R. S. (2016). Contributions of greenland and antarctica to global and regional sea level change. *Oceanography*, 29(4):154–159. [4](#)

- [89] LeVeque, R. J. (2002). *Finite Volume Methods for Hyperbolic Problems*. Cambridge Texts in Applied Mathematics. Cambridge University Press. [51](#), [53](#)
- [90] Liang, S., Shuey, C. J., Russ, A. L., Fang, H., Chen, M., Walthall, C. L., Daughtry, C. S., and Hunt Jr, R. (2003). Narrowband to broadband conversions of land surface albedo: II. Validation. *Remote Sensing of Environment*, 84(1):25–41. [21](#)
- [91] Lindbäck, K., Pettersson, R., Hubbard, A. L., Doyle, S. H., van As, D., Mikkelsen, A. B., and Fitzpatrick, A. A. (2015). Subglacial water drainage, storage, and piracy beneath the Greenland ice sheet. *Geophysical Research Letters*, 42(18):7606–7614. [6](#)
- [92] MacDougall, A. H. and Flowers, G. E. (2011). Spatial and temporal transferability of a distributed energy-balance glacier melt model. *Journal of Climate*, 24(5):1480–1498. [16](#), [17](#), [44](#), [45](#), [96](#)
- [93] Marshall, J., Adcroft, A., Hill, C., Perelman, L., and Heisey, C. (1997). A finite-volume, incompressible Navier Stokes model for studies of the ocean on parallel computers. *Journal of Geophysical Research: Oceans*, 102(C3):5753–5766. [51](#)
- [94] Marshall, S. J. and Clarke, G. K. (1999). Modeling north american freshwater runoff through the last glacial cycle. *Quaternary Research*, 52(3):300–315. [10](#)
- [95] McGrath, D., Colgan, W., Steffen, K., Lauffenburger, P., and Balog, J. (2011). Assessing the summer water budget of a moulin basin in the sermeq avannarleq ablation region, greenland ice sheet. *Journal of Glaciology*, 57(205):954–964. [9](#), [10](#), [90](#)
- [96] Meier, M. F. and Post, A. (1969). What are glacier surges? *Canadian Journal of Earth Sciences*, 6(4):807–817. [18](#), [19](#)
- [97] Meyer, C. R. and Hewitt, I. J. (2017). A continuum model for meltwater flow through compacting snow. *The Cryosphere*, 11(6):2799–2813. [4](#), [66](#), [93](#)
- [98] Moon, T., Joughin, I., Smith, B., van den Broeke, M. R., van de Berg, W. J., Noël, B., and Usher, M. (2014). Distinct patterns of seasonal Greenland glacier velocity. *Geophysical Research Letters*, 41(20):7209–7216. [65](#)
- [99] Mölg, N., Ferguson, J., Bolch, T., and Vieli, A. (2020). On the influence of debris cover on glacier morphology: How high-relief structures evolve from smooth surfaces. *Geomorphology*, 357:107092. [16](#), [27](#)

- [100] Naegeli, K., Damm, A., Huss, M., Wulf, H., Schaepman, M., and Hoelzle, M. (2017). Cross-comparison of albedo products for glacier surfaces derived from airborne and satellite (Sentinel-2 and Landsat 8) optical data. *Remote Sensing*, 9(2):110. [20](#), [21](#), [34](#), [46](#)
- [101] Naegeli, K. and Huss, M. (2017). Sensitivity of mountain glacier mass balance to changes in bare-ice albedo. *Annals of Glaciology*, 58(75pt2):119–129. [49](#)
- [102] Neal, E. G., Hood, E., and Smikrud, K. (2010). Contribution of glacier runoff to freshwater discharge into the gulf of alaska. *Geophysical Research Letters*, 37(6). [3](#)
- [103] Nicholson, L. and Stiperski, I. (2020). Comparison of turbulent structures and energy fluxes over exposed and debris-covered glacier ice. *Journal of Glaciology*, pages 1–13. [16](#), [26](#)
- [104] Noël, B., van de Berg, W. J., Lhermitte, S., and van den Broeke, M. R. (2019). Rapid ablation zone expansion amplifies north Greenland mass loss. *Science Advances*, 5(9). [87](#)
- [105] Noël, B., van de Berg, W. J., Lhermitte, S., Wouters, B., Schaffer, N., and van den Broeke, M. R. (2018). Six decades of glacial mass loss in the Canadian Arctic Archipelago. *Journal of Geophysical Research: Earth Surface*, 123(6):1430–1449. [16](#), [20](#)
- [106] Nye, J. F. and Perutz, M. F. (1957). The distribution of stress and velocity in glaciers and ice-sheets. *Proceedings of the Royal Society of London. Series A. Mathematical and Physical Sciences*, 239(1216):113–133. [7](#)
- [107] Oerlemans, J. (1991). A model for the surface balance of ice masses: Part i: alpine glaciers. *Zeitschrift für Gletscherkunde und Glazialgeologie*, 27:63–83. [20](#)
- [108] Oerlemans, J. and Fortuin, J. P. F. (1992). Sensitivity of glaciers and small ice caps to greenhouse warming. *Science*, 258(5079):115–117. [16](#)
- [109] Oerlemans, J. and Grisogono, B. (2002). Glacier winds and parameterisation of the related surface heat fluxes. *Tellus A: Dynamic Meteorology and Oceanography*, 54(5):440–452. [34](#)
- [110] Olson, M. and Rupper, S. (2019). Impacts of topographic shading on direct solar radiation for valley glaciers in complex topography. *The Cryosphere*, 13(1):29–40. [16](#), [25](#)

- [111] Olson, M., Rupper, S., and Shean, D. E. (2019). Terrain induced biases in clear-sky shortwave radiation due to digital elevation model resolution for glaciers in complex terrain. *Frontiers in Earth Science*, 7:216. [46](#)
- [112] O’Neel, S., Hood, E., Bidlack, A. L., Fleming, S. W., Arimitsu, M. L., Arendt, A., Burgess, E., Sergeant, C. J., Beaudreau, A. H., Timm, K., Hayward, G. D., Reynolds, J. H., and Pyare, S. (2015). Icefield-to-Ocean Linkages across the Northern Pacific Coastal Temperate Rainforest Ecosystem. *BioScience*, 65(5):499–512. [3](#)
- [113] Pellicciotti, F., Carenzo, M., Helbing, J., Rimkus, S., and Burlando, P. (2009). On the role of subsurface heat conduction in glacier energy-balance modelling. *Annals of Glaciology*, 50(50):16–24. [17](#), [28](#), [45](#)
- [114] Pfeffer, W. T., Arendt, A. A., Bliss, A., Bolch, T., Cogley, J. G., Gardner, A. S., Hagen, J.-O., Hock, R., Kaser, G., Kienholz, C., and et al. (2014). The Randolph Glacier Inventory: a globally complete inventory of glaciers. *Journal of Glaciology*, 60(221):537–552. [15](#)
- [115] Pitcher, L. H. and Smith, L. C. (2019). Supraglacial streams and rivers. *Annual Review of Earth and Planetary Sciences*, 47(1):421–452. [5](#), [65](#), [77](#), [78](#), [91](#)
- [116] Porter, C., Morin, P., Howat, I., Noh, M.-J., Bates, B., Peterman, K., Keeseey, S., Schlenk, M., Gardiner, J., Tomko, K., Willis, M., Kelleher, C., Cloutier, M., Husby, E., Foga, S., Nakamura, H., Platson, M., Wethington, Michael, J., Williamson, C., Bauer, G., Enos, J., Arnold, G., Kramer, W., Becker, P., Doshi, A., D’Souza, C., Cummins, P., Laurier, F., and Bojesen, M. (2018). ArcticDEM. [20](#), [85](#), [86](#)
- [117] Rango, A. and Martinec, J. (1995). Revisiting the degree-day method for snowmelt computations. *Journal of the American Water Resources Association*, 31(4):657–669. [8](#)
- [118] Raymond, C. F. and Nolan, M. (2000). Drainage of a glacial lake through an ice spillway. *IAHS publication*, pages 199–210. [10](#), [11](#), [66](#), [72](#)
- [119] Reid, T. D. and Brock, B. W. (2010). An energy-balance model for debris-covered glaciers including heat conduction through the debris layer. *Journal of Glaciology*, 56(199):903–916. [26](#)
- [120] Reznichenko, N., Davies, T., Shulmeister, J., and McSaveney, M. (2010). Effects of debris on ice-surface melting rates: an experimental study. *Journal of Glaciology*, 56(197):384–394. [16](#), [26](#)

- [121] RGI Consortium (2017). Randolph Glacier Inventory - A dataset of global glacier outlines: Version 6.0. Technical Report, Global Land Ice Measurements from Space, Colorado, USA. [20](#)
- [122] Rye, C. J., Arnold, N. S., Willis, I. C., and Kohler, J. (2010). Modeling the surface mass balance of a high Arctic glacier using the ERA-40 reanalysis. *Journal of Geophysical Research: Earth Surface*, 115(F2). [16](#), [20](#)
- [123] Schoof, C. (2010). Ice-sheet acceleration driven by melt supply variability. *Nature*, 468(7325):803–806. [7](#)
- [124] Sevestre, H. and Benn, D. I. (2015). Climatic and geometric controls on the global distribution of surge-type glaciers: implications for a unifying model of surging. *Journal of Glaciology*, 61(228):646–662. [18](#)
- [125] Shaw, T. E., Brock, B. W., Fyffe, C. L., Pellicciotti, F., Rutter, N., and Diotri, F. (2016). Air temperature distribution and energy-balance modelling of a debris-covered glacier. *Journal of Glaciology*, 62(231):185–198. [16](#), [26](#)
- [126] Shepherd, A., Ivins, E., Rignot, E., Smith, B., van Den Broeke, M., Velicogna, I., Whitehouse, P., Briggs, K., Joughin, I., Krinner, G., et al. (2020). Mass balance of the greenland ice sheet from 1992 to 2018. *Nature*, 579(7798):233–239. [65](#)
- [127] Shrestha, A. B., Steiner, J., Nepal, S., Maharjan, S. B., Jackson, M., Rasul, G., and Bajracharya, B. (2021). Understanding the Chamoli flood: Cause, process, impacts, and context of rapid infrastructure development. Technical report, ICIMOD. [1](#)
- [128] Shugar, D. H., Clague, J. J., Best, J. L., Schoof, C., Willis, M. J., Copland, L., and Roe, G. H. (2017). River piracy and drainage basin reorganization led by climate-driven glacier retreat. *Nature Geoscience*, 10(5):370–375. [19](#)
- [129] Shugar, D. H., Rabus, B. T., Clague, J. J., and Capps, D. M. (2012). The response of Black Rapids Glacier, Alaska, to the Denali earthquake rock avalanches. *Journal of Geophysical Research: Earth Surface*, 117(F1). [46](#)
- [130] Smith, L. C., Yang, K., Pitcher, L. H., Overstreet, B. T., Chu, V. W., Rennermalm, Å. K., Ryan, J. C., Cooper, M. G., Gleason, C. J., Tedesco, M., Jeyaratnam, J., van As, D., van den Broeke, M. R., van de Berg, W. J., Noël, B., Langen, P. L., Cullather, R. I., Zhao, B., Willis, M. J., Hubbard, A., Box, J. E., Jenner, B. A., and Behar, A. E. (2017). Direct measurements of meltwater runoff on the greenland ice sheet surface. *Proceedings of the National Academy of Sciences*, 114(50):E10622–E10631. [10](#), [11](#), [12](#), [66](#), [67](#)

- [131] Sole, A., Nienow, P., Bartholomew, I., Mair, D., Cowton, T., Tedstone, A., and King, M. A. (2013). Winter motion mediates dynamic response of the Greenland Ice Sheet to warmer summers. *Geophysical Research Letters*, 40(15):3940–3944. [65](#)
- [132] Sommers, A., Rajaram, H., and Morlighem, M. (2018). Shakti: Subglacial hydrology and kinetic, transient interactions v1.0. *Geoscientific Model Development*, 11(7):2955–2974. [13](#)
- [133] Sozer, E., Brehm, C., and Kiris, C. C. (2014). Gradient calculation methods on arbitrary polyhedral unstructured meshes for cell-centered cfd solvers. In *52nd Aerospace Sciences Meeting*, page 1440. [54](#)
- [134] St Germain, S. L. and Moorman, B. J. (2019). Long-term observations of supraglacial streams on an Arctic glacier. *Journal of Glaciology*, 65(254):900–911. [4](#), [66](#), [77](#), [90](#), [92](#), [93](#)
- [135] Steiner, J. F., Litt, M., Stigter, E. E., Shea, J., Bierkens, M. F. P., and Immerzeel, W. W. (2018). The importance of turbulent fluxes in the surface energy balance of a debris-covered glacier in the Himalayas. *Frontiers in Earth Science*, 6:144. [16](#), [17](#), [26](#)
- [136] Stevens, I. T., Irvine-Fynn, T. D., Porter, P. R., Cook, J. M., Edwards, A., Smart, M., Moorman, B. J., Hodson, A. J., and Mitchell, A. C. (2018). Near-surface hydraulic conductivity of northern hemisphere glaciers. *Hydrological Processes*, 32(7):850–865. [45](#)
- [137] Stevens, L. A., Nettles, M., Davis, J. L., Creyts, T. T., Kingslake, J., Ahlstrøm, A. P., and Larsen, T. B. (2021). Helheim glacier diurnal velocity fluctuations driven by surface melt forcing. *Journal of Glaciology*, page 1–13. [7](#)
- [138] Sundal, A. V., Shepherd, A., Nienow, P., Hanna, E., Palmer, S., and Huybrechts, P. (2011). Melt-induced speed-up of greenland ice sheet offset by efficient subglacial drainage. *Nature*, 469(7331):521–524. [65](#)
- [139] Tedstone, A. J., Cook, J. M., Williamson, C. J., Hofer, S., McCutcheon, J., Irvine-Fynn, T., Gribbin, T., and Tranter, M. (2020). Algal growth and weathering crust state drive variability in western Greenland Ice Sheet ice albedo. *The Cryosphere*, 14(2):521–538. [49](#)
- [140] Thomson, L. I. and Copland, L. (2017). Multi-decadal reduction in glacier velocities and mechanisms driving deceleration at polythermal White Glacier, Arctic Canada. *Journal of Glaciology*, 63(239):450–463. [16](#)

- [141] van den Broeke, M. R. (1997). Momentum, heat, and moisture budgets of the katabatic wind layer over a midlatitude glacier in summer. *Journal of Applied Meteorology*, 36(6):763–774. [34](#)
- [142] van der Veen, C. J., Ahn, Y., Csatho, B. M., Mosley-Thompson, E., and Krabill, W. B. (2009). Surface roughness over the northern half of the Greenland Ice Sheet from airborne laser altimetry. *Journal of Geophysical Research: Earth Surface*, 114(F1). [44](#)
- [143] Vaughan, D., Comiso, J., Allison, I., Carrasco, J., Kaser, G., Kwok, R., Mote, P., Murray, T., Paul, F., Ren, J., Rignot, E., Solomina, O., Steffen, K., and Zhang, T. (2013). Observations: Cryosphere. In Stocker, T., Qin, D., Plattner, G.-K., Tignor, M., Allen, S., Boschung, J., Nauels, A., Xia, Y., Bex, V., and Midgley, P., editors, *Climate Change 2013: The Physical Science Basis. Contribution of Working Group I to the Fifth Assessment Report of the Intergovernmental Panel on Climate Change*, book section 4, page 317–382. Cambridge University Press, Cambridge, United Kingdom and New York, NY, USA. [1](#), [4](#)
- [144] Wang, K., Davies, E. G., and Liu, J. (2019). Integrated water resources management and modeling: A case study of Bow river basin, Canada. *Journal of Cleaner Production*, 240:118242. [2](#)
- [145] Werder, M. A., Hewitt, I. J., Schoof, C. G., and Flowers, G. E. (2013). Modeling channelized and distributed subglacial drainage in two dimensions. *Journal of Geophysical Research: Earth Surface*, 118(4):2140–2158. [13](#), [49](#), [52](#), [67](#), [68](#), [69](#), [72](#), [74](#), [75](#), [91](#), [99](#)
- [146] Wheler, B. A. (2009). Glacier melt modelling in the Donjek Range, St. Elias Mountains, Yukon Territory. Master’s thesis, Dept. of Earth Sciences-Simon Fraser University. [17](#), [28](#), [32](#)
- [147] Wheler, B. A. and Flowers, G. E. (2011). Glacier subsurface heat-flux characterizations for energy-balance modelling in the Donjek Range, southwest Yukon, Canada. *Journal of Glaciology*, 57(201):121–133. [16](#), [28](#), [29](#), [32](#), [34](#), [44](#), [45](#), [96](#), [119](#)
- [148] Williamson, C. J., Cameron, K. A., Cook, J. M., Zarsky, J. D., Stibal, M., and Edwards, A. (2019). Glacier algae: A dark past and a darker future. *Frontiers in microbiology*, 10:524. [49](#)
- [149] Williamson, S. N., Copland, L., and Hik, D. S. (2016). The accuracy of satellite-derived albedo for northern alpine and glaciated land covers. *Polar Science*, 10(3):262 – 269. ISAR-4/ICARPIII, Science Symposium of ASSW2015. [18](#), [35](#), [36](#), [47](#)

- [150] Willis, I. C. (1995). Intra-annual variations in glacier motion: a review. *Progress in Physical Geography: Earth and Environment*, 19(1):61–106. [16](#), [19](#)
- [151] Yang, K. and Smith, L. C. (2016). Internally drained catchments dominate supraglacial hydrology of the southwest greenland ice sheet. *Journal of Geophysical Research: Earth Surface*, 121(10):1891–1910. [85](#), [86](#), [87](#), [89](#), [92](#), [94](#), [97](#), [98](#), [128](#)
- [152] Yang, K., Smith, L. C., Chu, V. W., Pitcher, L. H., Gleason, C. J., Rennermalm, A. K., and Li, M. (2016). Fluvial morphometry of supraglacial river networks on the southwest Greenland Ice Sheet. *GIScience & Remote Sensing*, 53(4):459–482. [91](#)
- [153] Yang, K., Smith, L. C., Karlstrom, L., Cooper, M. G., Tedesco, M., van As, D., Cheng, X., Chen, Z., and Li, M. (2018). A new surface meltwater routing model for use on the Greenland Ice Sheet surface. *The Cryosphere*, 12(12):3791–3811. [5](#), [10](#), [11](#), [12](#), [66](#), [67](#), [78](#), [90](#), [95](#), [98](#)
- [154] Zemp, M., Jansson, P., Holmlund, P., Gärtner-Roer, I., Koblet, T., Thee, P., and Haeberli, W. (2010). Reanalysis of multi-temporal aerial images of Storglaciären, Sweden (1959–99); – Part 2: Comparison of glaciological and volumetric mass balances. *The Cryosphere*, 4(3):345–357. [69](#)
- [155] Zwally, H. J., Abdalati, W., Herring, T., Larson, K., Saba, J., and Steffen, K. (2002). Surface melt-induced acceleration of greenland ice-sheet flow. *Science*, 297(5579):218–222. [65](#)

APPENDICES

Appendix A

Supplementary material for Application of an improved surface energy balance model to two large valley glaciers in the St. Elias Mountains, Yukon

Table A.1: Location of HOBOS and temporal coverage of HOBOS Temperature and Relative Humidity and surface ablation measurements on Nàhùdäy and Kaskawulsh Glaciers. Note that data gaps may exist within the indicated measurement periods

Glacier	Station	Latitude	Longitude	Elevation (m asl.)	Temporal coverage	
					HOBOS	Surface ablation
Nàhùdäy	Lower	60.2908°N	138.1808°W	760	2018-08-25–2019-05-12	2018-07-27–2019-07-06
	Middle	60.3076°N	138.3593°W	1002	2017-07-25–2018-07-25	2018-07-27–2018-08-08
	Upper	60.2840°N	138.5406°W	1218	2017-07-25–2019-07-09	–
Kaskawulsh	Lower	60.7675°N	138.7712°W	1163	2010-06-05–2015-04-09; 2018-07-23–2019-05-11	2013-08-28–2015-04-09 2017-08-22–2019-05-11
	Middle	60.7537°N	138.9713°W	1521	2010-06-05–2015-04-09; 2018-07-23–2019-03-20	2017-08-22–2019-03-18; 2017-08-22–2019-03-18
	Upper	60.7267°N	139.1330°W	1705	2010-06-05–2015-04-09; 2018-07-23–2019-05-11	2010-07-06–2015-04-09 2017-08-22–2018-08-26
	South Arm	60.6704°N	138.7992°W	1487	2010-06-05–2014-08-12	2010-05-06–2013-07-23

Table A.2: Summary of weather stations on Kaskawulsh and Nàhùdäy Glacier. The data gaps are discussed in Chapter 2

AWS	Start date	End data	Data gaps	Variables measured	Measurement frequency
AWSK1	2010-06-05	2018-07-26	2017-08-29–2018-07-26	T, SW_{in}, U, P	1 hour (T, SW_{in}, U), 3 hour (P)
AWSK2	2018-07-26	Continuing	2019-05-11–2019-09-11	$T, RH, SW_{in}, SW_{out}, LW_{in}, LW_{out}, U, P$	2 hour
AWSN1	2018-07-26	2019-06-05	None	$T, RH, SW_{in}, SW_{out}, LW_{in}, LW_{out}, U, P$	2 hour

Table A.3: Default parameters used in the SEB model

Parameter	Description	Default value
ε_s	Ice emissivity	1
ε_a	Atmospheric emissivity	Varies
z_0	Momentum roughness length	3×10^{-3} to 5×10^{-3} m
z_{0H}	Heat roughness length	$z_0/100$
z_{0E}	Moisture roughness length	$z_0/100$
z	Height of RH, T measurements above ice surface	1.35 to 2 m
ρ_{ice}	Ice density	850 kg m^{-3}
T_{12m}	Ice temperature at 12 metre depth	$-3 \text{ }^\circ\text{C}$ [147]
Δt_{SSM}	Subsurface and energy balance model timestep	900 s
Δt_{AWS}	Meteorological forcing timestep	3600 to 7200 s
N_{SSM}	Number of vertical layers in subsurface model	12

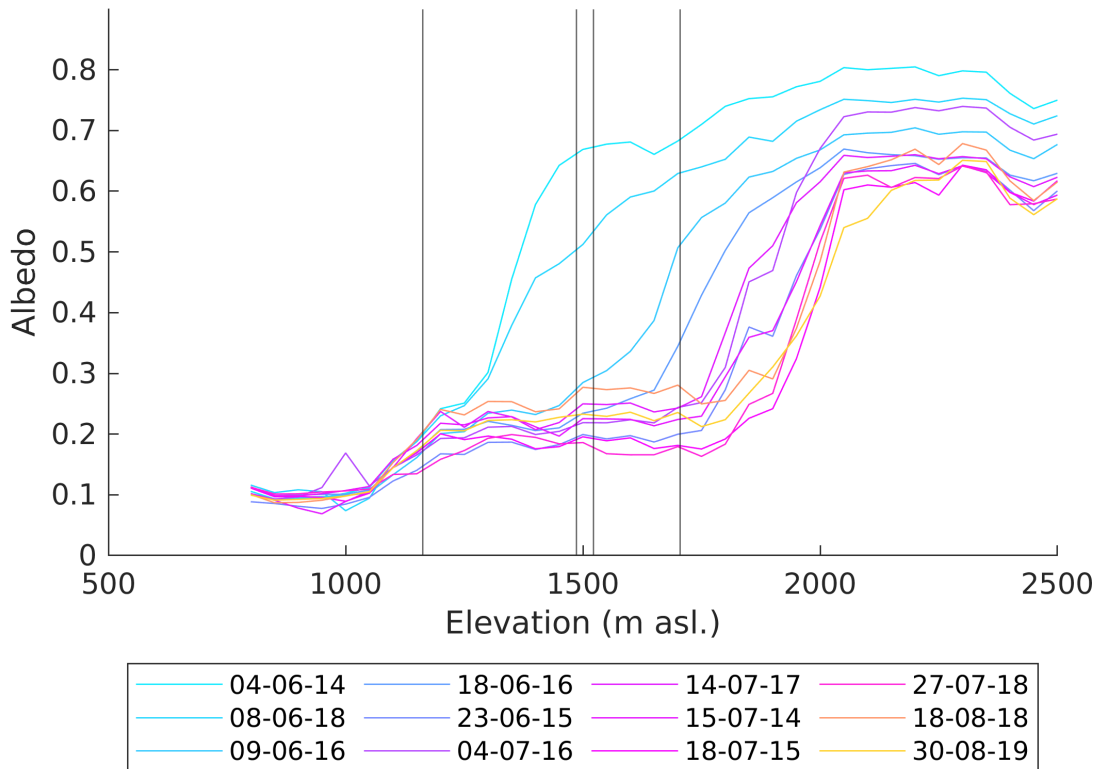


Figure A.1: Mean albedo as a function of elevation on Kaskawulsh Glacier, using 12 Landsat 8 scenes from 2014-2019. Vertical black lines indicate the elevation of the four HOBO stations.

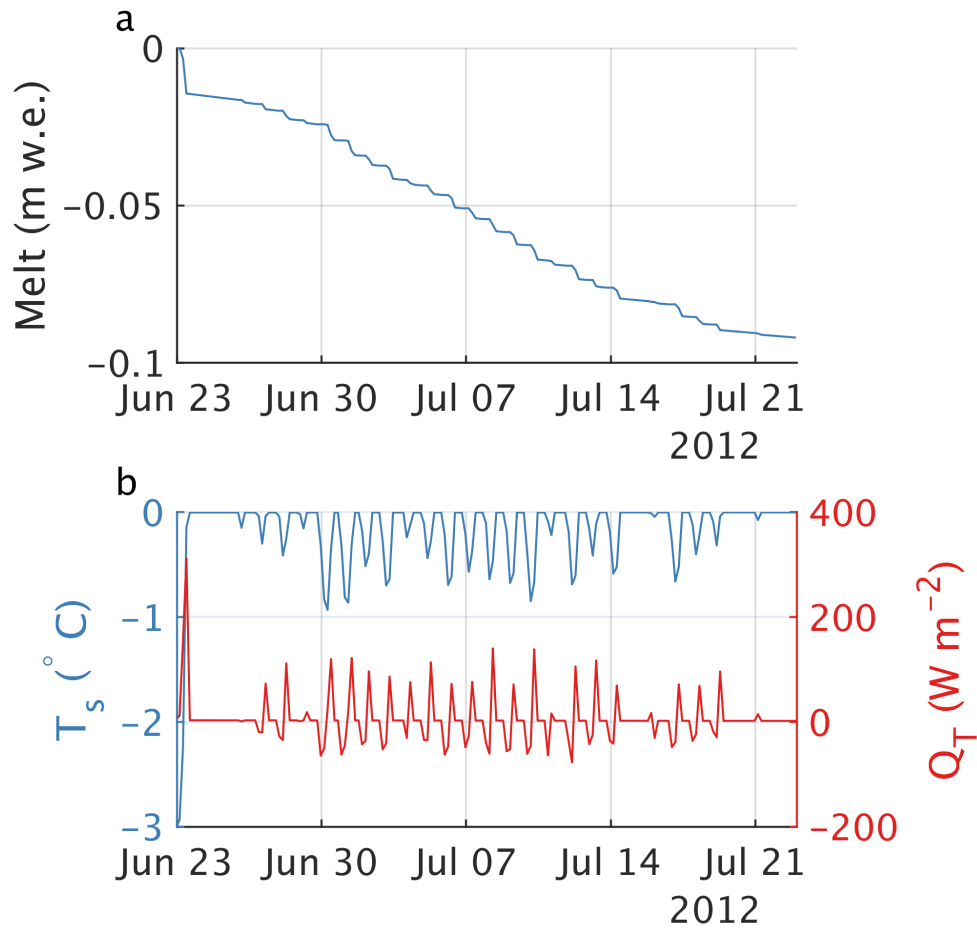


Figure A.2: (a) Difference in modelled melt (m w.e.) with and without subsurface model at the Kaskawulsh Upper station during the beginning of the 2012 melt season. (b) Modelled surface temperature (blue) and heat used to warm the ice (orange).

Table A.4: Total and relative model error (ME) and ablation rate error (ARE) compared to available validation data (UDS and time-lapse ablation stake measurements). Empty cells represent locations and years with no measurements to compare with. Error at the middle station of Nàlùdäy in 2018 is computed using the extended melt record derived from measurements at the lower station

Glacier	Melt year	Lower		Middle		Upper		South Arm	
		ME (m)	ARE (m day ⁻¹)						
Kaskawulsh	2010					-0.08	-0.0037	0.52	0.0094
						-3.0%	-6.8%	16.0%	17.5%
	2011					-0.07	-0.0053	0.10	0.0034
						-12.3%	-20.2%	22.3%	12.0%
	2012					0.27	0.0013		
						8.5%	0.3%		
	2013	0.03	0.0015			-0.68	-0.0093	-0.21	0.0011
		4.8%	3.2%			-14.4%	-17.3%	-2.3%	1.8%
	2014	0.29	0.0017			-0.13	-0.0056		
		7.1%	3.2%			-3.6%	-11.7%		
	2018	0.0025	0.0010	0.10	-0.0051	-0.14	0.0010		
		0.1%	1.8%	4.4%	-9.6%	-7.7%	1.8%		
Nàlùdäy	2018	-0.10	0.0021	-0.23	-0.0011				
		-3.3%	3.4%	-8.4%	-2.1%				

Appendix B

Supplementary information to “Modeling the dynamics of supraglacial rivers and distributed meltwater flow with the Subaerial Drainage System (SaDS) model”

B.1 Introduction

This supporting information provides additional figures in support of the analysis of the synthetic domain model outputs and Greenland Ice Sheet input data to support the conclusions made in the main text.

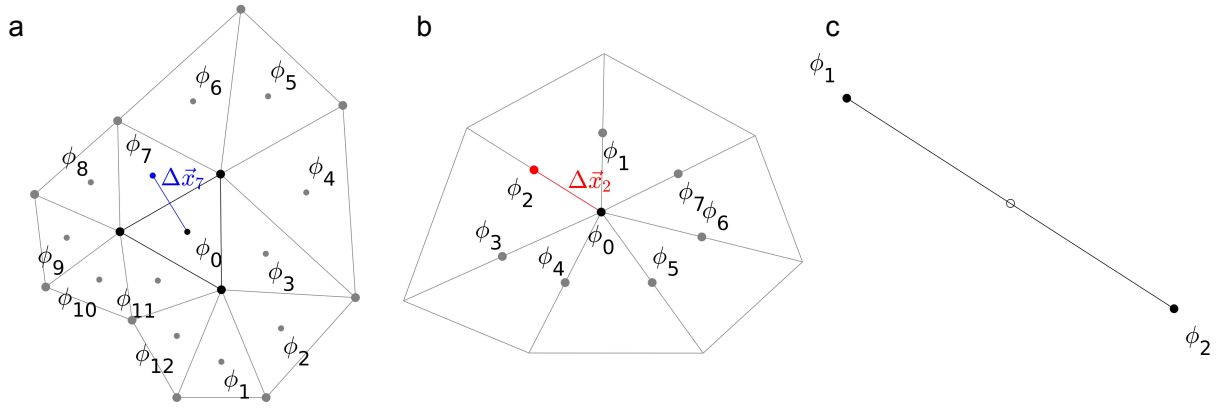


Figure B.1: (a) Gradient reconstruction stencil centered on element Ω_0 . The blue vector $\Delta \mathbf{x}_7$ illustrates the distances used in equation (3.6) to calculate the gradient on element Ω_0 . (b) Stencil used to calculate the channel potential on node Λ_0 . (c) The along-channel potential gradient is simply calculated from the potential difference on the connecting nodes and the length of the edge.

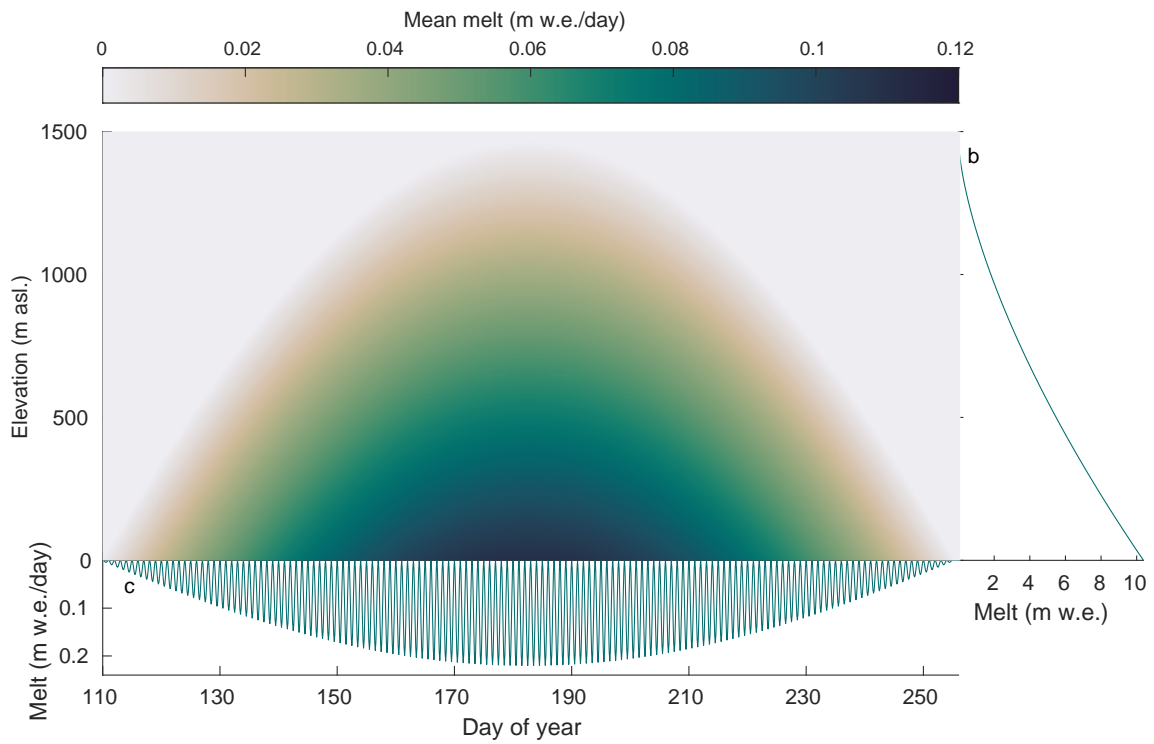


Figure B.2: Melt parameterization from de Fleurian et al. [40] for the ice sheet margin geometry. (a) Profiles of mean daily melt the synthetic ice sheet margin over the melt season. (b) Melt summed over the melt season as a function of elevation. (c) Instantaneous maximum melt in the domain, showing the diurnal cycle.

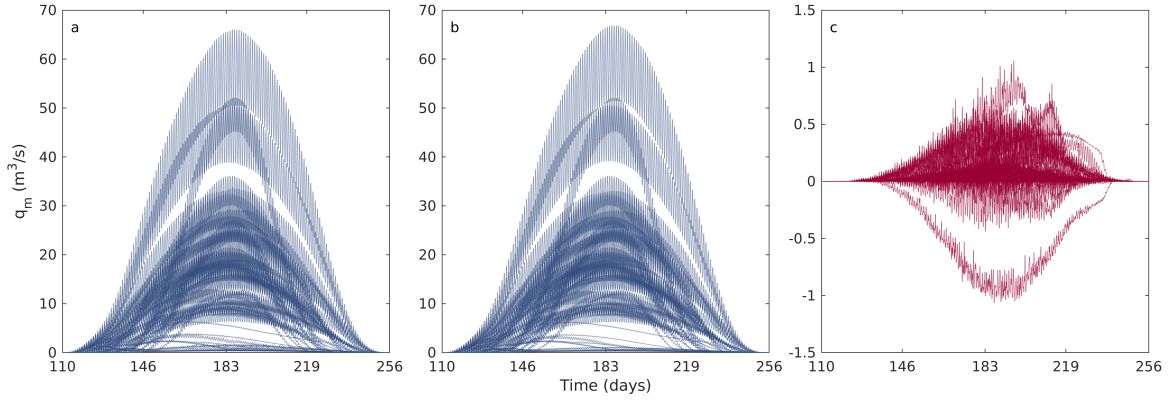


Figure B.3: Moulin inputs for the baseline case (a), case T1 with a timestep of 90 seconds (b), and the difference between the baseline and case T1 (c).

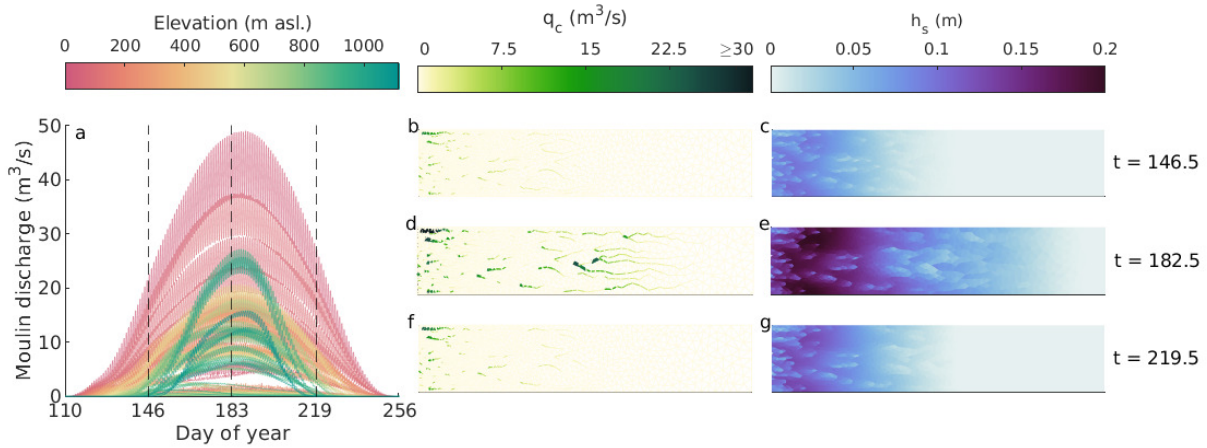


Figure B.4: Overview of model outputs for the case M1. (a) Moulin flux for the 100 moulins, colored by the elevation of the moulins. The vertical dashed lines indicate the times used for panels (b-g). (b, d, f) Volume flux in the channels at noon on days 146, 182, and 219. (c, e, g) Sheet water thickness at noon on days 146, 182, and 219.

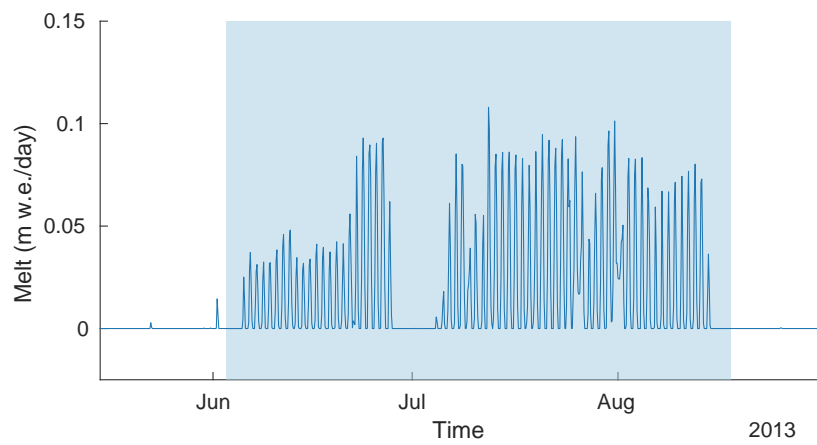


Figure B.5: Median surface melt rate calculated from RACMO2.3p2 data. The shaded box defines the extent of the melt season.

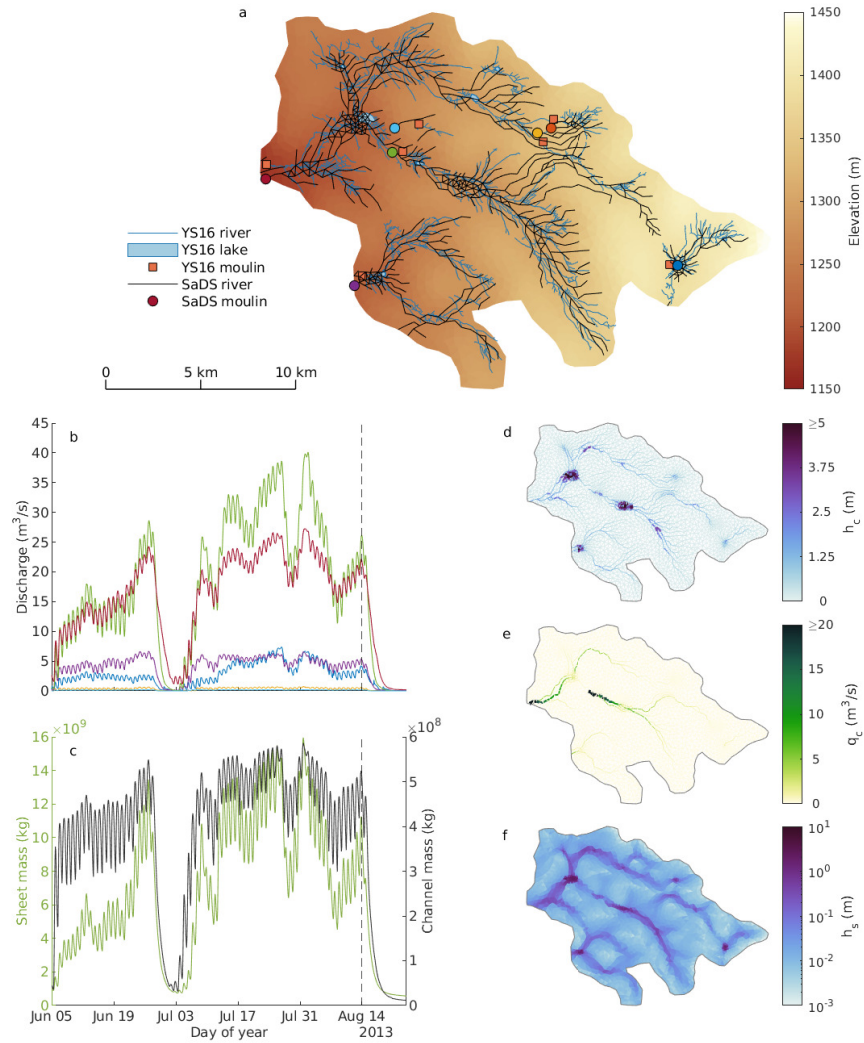


Figure B.6: (a) Comparison between the modeled drainage system (black lines) and the drainage system mapped by Yang and Smith [151, legend elements indicated by YS16] in the case of initializing channels with a minimum 25 cm incision depth. Yang and Smith [151]. The background is colored by the surface elevation. (b) Discharge for the moulins shown in (a). (c) Total mass in the distributed water sheet (left axis, green) and the channel system (right axis, black). The vertical dashed lines in (b) and (c) indicated the time of the maps shown in (d), (e), and (f). (d) Water thickness in supraglacial channels. (e) Channel volume flux. (f) Water sheet thickness (note the logarithmic color scale).

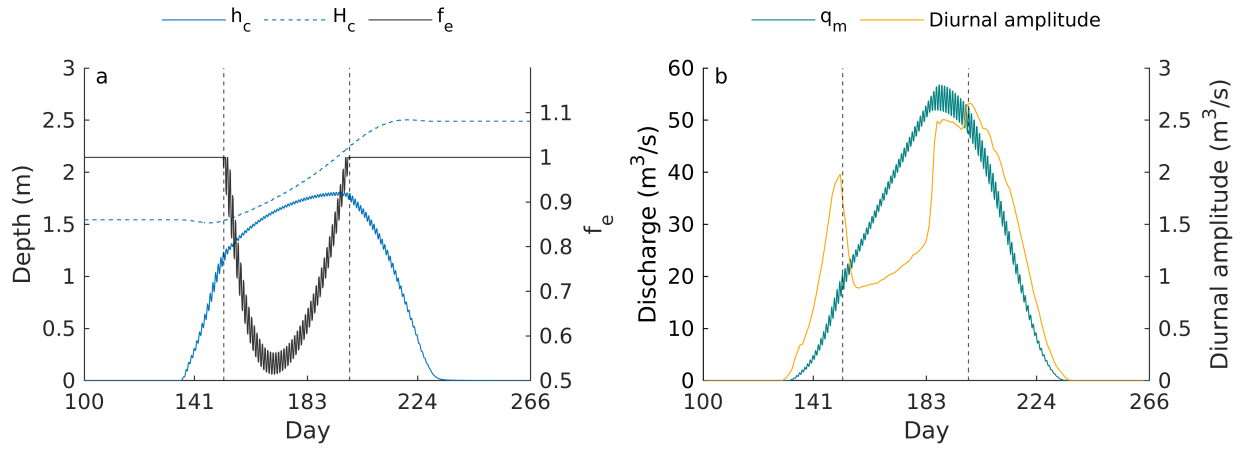


Figure B.7: Details of the channel configuration leading to the two distinct peaks in the diurnal amplitude. (a) Water depth h_c , incision depth H_c (left axis), and exchange fraction f_e (right axis) for one channel segment feeding the moulin with inputs shown in (b). (b) Moulin input q_m (left axis) and diurnal amplitude of the input (right axis) for one of the moulins showing two peaks in the diurnal amplitude.

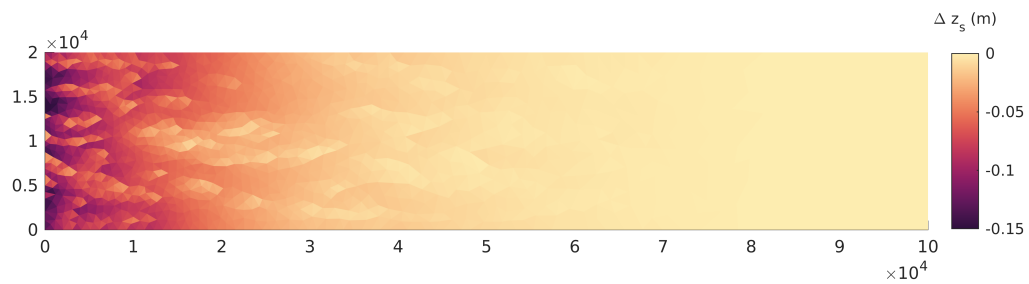


Figure B.8: Surface ablation due to melt by potential energy dissipation in the distributed sheet system for the baseline run.

Table B.1: Statistics for the baseline mesh and the meshes used in the resolution sensitivity tests. The maximum area refers to the maximum area threshold used for the highest elevations when creating the triangular mesh. The maximum refined area refers to the maximum area threshold used for the lowest elevations when creating the triangular mesh.

Mesh	Nodes	Edges	Elements	Maximum area (m ²)	Maximum refined area (m ²)	Maximum edge length (m)	Minimum edge length (m)
R1	582	1635	1054	1.25×10^7	1.25×10^6	5.98×10^3	1.02×10^3
Baseline	1205	3443	2239	6.00×10^6	6.00×10^5	4.46×10^3	625
R2	2451	7113	4663	2.86×10^6	2.86×10^5	3.12×10^3	369